AD-A037 441 PURDUE UNIV LAFAYETTE IND PROJECT SQUID HEADQUARTERS F/G 20/4
LAMINARISCENT TURBULENT BOUNDARY LAYERS: EXPERIMENTS ON NOZZLE --ETC(U)
JAN 77 R L SIMPSON, C R SHACKLETON N00014-75-C-1143

UNCLASSIFIED SQUID-SMU-2-PU NL

1 OF 2
AD
A037441

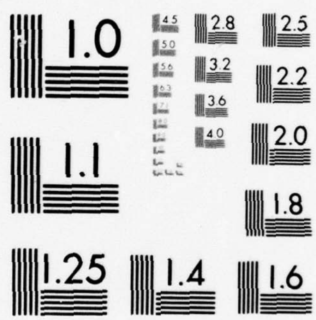

MICROCOPY RESOLUTION TEST CHART
NATIONAL BUREAU OF STANDARDS-1963-A

(12)

PROJECT SQUID

TECHNICAL REPORT SMU-2-PU

LAMINARISCENT TURBULENT BOUNDRY LAYERS: EXPERIMENTS ON NOZZLE FLOWS

by

ROGER L. SIMPSON AND C. R. SHACKLETON
SOUTHERN METHODIST UNIVERSITY
DALLAS, TEXAS

PROJECT SQUID HEADQUARTERS
CHAFFEE HALL
PURDUE UNIVERSITY
WEST LAFAYETTE, INDIANA 47907

Project SQUID is a cooperative program of basic research relating to Jet Propulsion. It is sponsored by the Office of Naval Research and is administered by Purdue University through Contract N00014-75-C-1143, NR-098-038.

(14) SQUID-SMU-2-PU

(9) Technical Report SMU-2-PU

PROJECT SQUID

A COOPERATIVE PROGRAM OF FUNDAMENTAL RESEARCH
AS RELATED TO JET PROPULSION
OFFICE OF NAVAL RESEARCH, DEPARTMENT OF THE NAVY

(15) CONTRACT N00014-75-C-1143 NR-098-038

(6) LAMINARISCENT TURBULENT BOUNDARY LAYERS: EXPERIMENTS ON NOZZLE FLOWS

by

(10) Roger L. Simpson and C. R. Shackleton
SOUTHERN METHODIST UNIVERSITY

(11) January 1977

(12) 107p.

PROJECT SQUID HEADQUARTERS
CHAFFEE HALL
PURDUE UNIVERSITY
WEST LAFAYETTE, INDIANA 47907

403 617

bpg

LAMINARISCENT TURBULENT BOUNDARY LAYERS: EXPERIMENTS ON NOZZLE FLOWS

by

Roger L. Simpson* and C. R. Shackleton**

ABSTRACT

Because a turbulent boundary layer in a nozzle undergoes strong acceleration, a laminariscent boundary layer with the benefit of a lower surface heat transfer rate can result for some short distance. Here and in a previous report (Simpson and Wallace, 1975) several phenomena which accompany laminariscence produced by strong acceleration are examined for nozzle-flow and sink-flow accelerational distributions, respectively. Several different type measurements of the structure of two nozzle-type flows are reported to determine how an initially normal turbulent boundary layer approaches the laminar-like state, including mean velocity and Reynolds stresses profiles, spectra, turbulent/non-turbulent interfacial structure, and wall bursting and sublayer spanwise spatial structure.

As a result of these experiments, it appears that the surface skin-friction is not reduced to laminar values in sink flows unless $K(=\nu U_\infty^{-2} dU_\infty/dx)$ is greater than about 3.6×10^{-6}. In nozzle-type flows, K must also be greater than this value over a short distance in order to produce a short relaminarized region downstream. The large-eddy structure of the outer region governs the bursting frequency, the intermittent bulge passage frequency, and influences the wall flow behavior downstream. After the cessation of entrainment of free-stream fluid, these frequencies approach constant values. The wall spanwise structure appears to lag behind local conditions and to reflect upstream flow behavior. After retransition to a low acceleration turbulent boundary layer downstream, much larger spanwise scale structures are observed.

The entrainment rate of non-turbulent fluid decreases to zero at about the streamwise location at which the shape factor reaches a minimum value. The cessation of entrainment by the eruption and

---

* Professor of Mechanical Engineering, Southern Methodist University.
** Research Assistant, Dept. of Mechanical Engrg., Southern Methodist University.

and engulfment action of the large eddies can be traced to the reduction of available turbulence energy for diffusion to free-stream fluid. This reduction of available energy is due to the negative normal stresses turbulence energy production term. Spectral distributions of the streamwise fluctuation F(n) possess a frequency region where nF(n) is constant for laminar-like boundary layers at large K values.

TABLE OF CONTENTS

NOMENCLATURE

A, B, C, D	constants.
$C_f/2$	$= \tau_w/\rho U_\infty^2$, friction factor.
E, e	mean and fluctuation voltages.
F(n)	spectral density defined by equation (9).
F, F_δ	defined by equations (18) and (20), respectively.
f, f'	U/U_∞ and $\partial f/\partial\eta$, respectively.
H	$= \delta^*/\theta$, shape factor.
K	$= \frac{\nu}{U_\infty^2}\frac{dU_\infty}{dx}$; also a constant in equation (12).
L_z	integral length scale defined by equation (14).
M	*constant.*
m	exponent in split-film calibration curve.
n	frequency, Hz.
n_{i_Y}	frequency of intermittent bulge passage at $\overline{Y}$.
dP/dx	pressure gradient.
Q_i	power dissipation in split-film sensor i.
$\overline{q^2}$	$= \overline{u^2} + \overline{v^2} + \overline{w^2}$.
$s\hat{R}_{\tau\tau}(z, T_s)$	normalized spatial cross-correlation of two τ surface fluctuation signals during sample time T_s.
$s\hat{R}(z)$	$s\hat{R}(z, T_s)$ as T_s becomes very large.
Re_θ	$= U_\infty\theta/\nu$, momentum thickness Reynolds number.
Re_λ	$= \frac{(\overline{u^2})^{1/2}\lambda}{\nu}$, microscale Reynolds number.
T_s	length of sample time.
t	time delay; time.

U_τ $= (\tau_w/\rho)^{1/2}$, shear velocity.

u, v, w, velocity fluctuations in the streamwise, normal, and spanwise directions.

U, V, W mean velocities in the streamwise, normal, and spanwise directions.

$-\overline{uv}$ kinematic Reynolds shearing stress.

V_E entrainment velocity.

x, y, z cartesian co-ordinates in the streamwise, normal, and spanwise directions, respectively.

$\overline{Y}$ distance from the wall to where $\gamma = 0.5$.

SUBSCRIPTS

b denotes "bursting" value.

eff denotes effective cooling velocity.

i split-film sensor index.

ℓ denotes linearized signal.

w denotes wall value.

∞ free-stream condition.

GREEK

α constant in equation (10); split-film probe yaw parameter.

γ intermittency, long-time averaged fraction of time that the flow is turbulent.

δ $\delta_{0.99}$ = y where f = 0.99; $\delta_{0.995}$ = y where f = 0.995.

δ^* $= \int_0^\infty \left(1 - \frac{U}{U_\infty}\right) dy$, displacement thickness.

ε dissipation rate

η $= yU_\infty/\nu$

θ $= \int_0^\infty \frac{U}{U_\infty} \left(1 - \frac{U}{U_\infty}\right) dy$, momentum thickness.

λ	$= (15\nu\overline{u^2}/\varepsilon)^{1/2}$, a turbulence microscale.
λ_z	spanwise wavelength in wall sensors cross-correlations.
λ^+_{z1}, λ^+_{z2}	defined by equations (15).
ν	kinematic viscosity.
ρ	density.
σ	standard deviation for intermittency distribution.
τ	shearing stress.
ϕ	angle of flow incidence to split-film probe.
Ω	logarithmic equation (5) constant.

1. INTRODUCTION

The strong acceleration of turbulent boundary layers in a nozzle can produce the benefit of a substantially reduced convective heat transfer rate when relaminarization occurs (Moretti and Kays, 1965). The accelerational parameter K, defined as $\nu U_\infty^{-2} dU_\infty/dx$, must increase to a value in excess of about 3.6×10^{-6} (Kline et al., 1967) for relaminarization to occur. The practical consideration that flow acceleration extends over a finite length then requires that K decrease to zero downstream. Narasimha and Sreenivasan (1973) reexamined the behavior of this type of flow from the time-averaged results of many previous experiments. However, there is little information on the flow structure that would explain the mechanisms for relaminarization. Exceptions are the space-time correlations of Blackwelder and Kovasznay (1972) for the large-scaled motion and the wall region structure reported by Schraub and Kline (Kline, et al., 1967).

The work described here is the second part of a program to provide experimental flow structure information for strongly-accelerated turbulent boundary layers under different K distributions. In the first part (Simpson and Wallace, 1975) results were obtained for two asymptotic sink-flow type turbulent boundary layers with constant K distributions (flow A, $K = 2.17 \times 10^{-6}$; flow B, $K = 3.19 \times 10^{-6}$). Here results are presented for a flow in which K increases linearly with x (flow C) and a flow in which K increases linearly with x to a maximum value, stays constant at this level for a short distance, and then decreases linearly with x (flow D). Flow C models the rapid increase in K encountered in nozzles while flow D models both the increase and decrease in K. Since the acceleration of both flows took place in the same length of wind tunnel test section, dK/dx for the increasing K portion of flow D was more than double dK/dx for flow C.

The type of measurements reported here for flows C and D are similar to those obtained for flows A and B. In addition to mean velocity and Reynolds' stresses measurements, spectra of the streamwise fluctuations were obtained. This was partly motivated by the presence of a flat nF(n) spectrum for flow B and the question as to whether this behavior accompanies true relaminarization. Other measurements are the turbulent/non-turbulent interfacial intermittency and frequency of passage of intermittent turbulent bulges, the wall "bursting" frequencies or rate of passage of eddies over the wall, and the spanwise spatial structure at the wall. This latter group of measurements provides further insight as to the roles that the bursting behavior, spanwise structure, and intermittency play in relaminarization. Since these measurements have been obtained for four different K distribution flows on the same apparatus, the effect of the K distribution on the developing flow structure can be determined.

2. EXPERIMENTAL APPARATUS

In general, all of the apparatus and instrumentation described by Simpson and Wallace (1975) for flows A and B were used for flows C and D. The SMU wind tunnel with a sixteen feet long, three feet wide, test section was used to produce the desired boundary layer on the flat bottom wall by adjusting the plexiglas top wall. In the current experiments the freestream flow upstream of the acceleration was uniform within 0.066% in the spanwise direction and within 1% in the vertical direction, with a streamwise turbulence intensity of 0.6% at 9.1 fps. At the tunnel exit the free-stream streamwise turbulence intensity dropped to below 0.55% and 0.5% for flows C and D, respectively. Of this intensity, about 0.5% was due to unsteadiness at about 20 Hz. Figure 1 is a side view schematic of the test section with the upper wall locations for flows A, C, and D. In all four flows the flat upper wall was 15 inches above the test wall at the entrance and 19.5 inches above it at the 96 inches location. For flow C the parabolic-shaped upper wall section began at 96 inches and was 1.72 inches above the test wall at the exit at 190.8 inches. For flow D the antisymmetric ogee-shaped upper wall began at 96 inches and was 1.84 inches above the test wall at 189.7 inches. All experimental data were obtained with the temperature maintained constant at 77 ±1/2°F and a constant stagnation pressure at the exit.

The 1/4 inches blunt leading edge trip on the test wall and the boundary layer smoke injection arrangement upstream of the trip were the same as used for flows A and B. The same smoke generation system with a mean particle size of about 1 micron was used when smoke was used to mark turbulent fluid upstream of relaminarization. For these intermittency measurements the optics and traversing equipment of the SMU laser anemometer were used as for flows A and B.

Standard Thermo-Systems, Inc., model 1050 constant temperature anemometers, model 1055 linearizers, model 1057 signal conditioners,

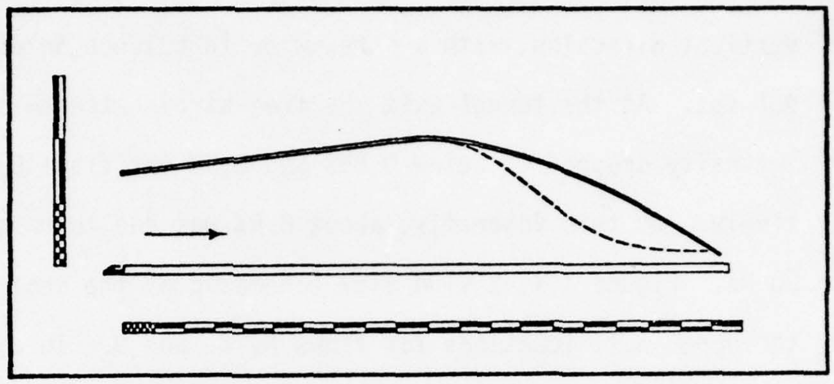

Figure 1. Sideview schematic of the test section: solid line, flow C; dashed line, flow D. Major divisions on abscissa and ordinate: 10 inches. Note 2:1 scale ratio.

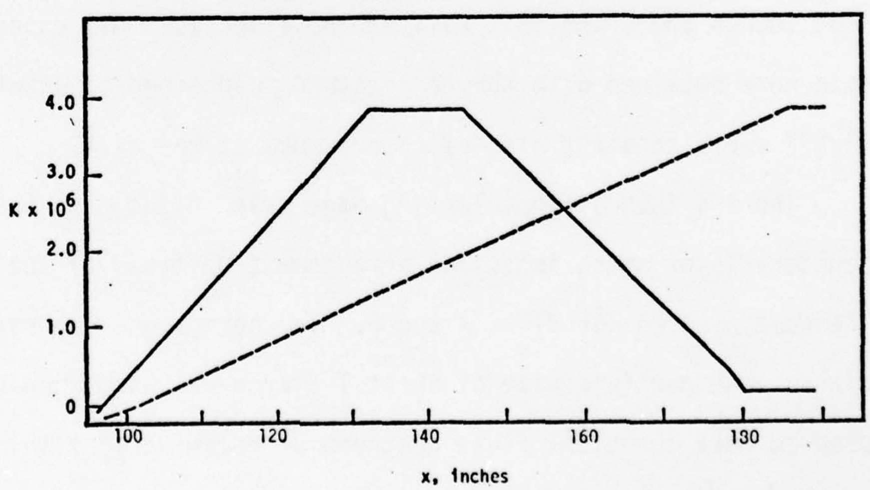

Figure 2. K distributions for flows C and D: flow C - dashed line; flow D - solid line.

and model 1015C correlator were used. A TSI model 1274-10 boundary layer hot-film probe was used in measuring the mean and streamwise fluctuation velocities in flow C while a model 1218-T1.5 boundary layer hot-wire probe was used for flow D. The sensing element for the hot-film is a 0.001 inches diameter platinum coated quartz rod with a sensing length of 0.04 inches. The 0.00015 inches diameter platinum-plated tungsten wire had a 0.05 inches sensing length. Based on the Collis and Williams (1959) equation for the anemometer bridge output calibration, the linearizers were adjusted. The linearizer output was directly checked with the known calibrator velocity for accuracy and linearity, the maximum tolerable deviation being less than about 1/2%. Consequently, the uncertainty on velocity measurements is about ±1/2%.

The split-film probe (TSI model 1287) was used to determine U, V, $\overline{u^2}$, $\overline{v^2}$, and $-\overline{uv}$ for flow C. This relatively new hot-film probe was selected because of its relatively small size since the boundary layers under study were thin. The split-film sensor is a modification of the basic platinum coated cylindrical film sensor. Two electrically independent films each cover one-half of the circumference of a 0.006 inches diameter quartz rod. Each film is operated by a separate constant temperature circuit. The non-uniform heat transfer distribution around a constant temperature cylinder is utilized to measure the fluctuating components of the instantaneous velocity vector. To avoid thermal variations in the substrate the sensors must be held at closely identical temperatures. The resulting output voltages are used in the same manner as those from an x-wire probe to determine mean and fluctuation quantities.

Using a right-handed coordinate system, the plane of the two splits that separate the two platinum films from one another are in the x-z plane, being nominally parallel to the test wall in these experiments. Following Spencer and Jones (1971), the power dissipated in each film can be related to the velocity by

$$Q_i = (A + BU^m_{eff})(1 + \alpha_i \frac{V}{U_{eff}}) \qquad i = 1, 2$$

neglecting axial cooling. The constants A, B, and m were obtained by velocity calibration as done for a single sensor probe; α_i was determined by azimuthal yaw calibration. The power dissipated is proportional to the square of the anemometer bridge output minus the zero flow voltage:

$$E_i = M_i(Q - Q_o)_i = M_i U^m_{eff} (1 + \alpha_i \frac{V}{U_{eff}})$$

The voltage E_i can be linearized directly in terms of U_{eff} using m = 0.5. Thus

$$E_{\ell i} = M_{\ell i} E_i^{1/m} = MU_{eff} (1 + \alpha_i \frac{V}{U_{eff}})^2$$

or when neglecting higher ordered terms the instantaneous voltage is

$$E_{\ell i} + e_{\ell i} = MU_{eff} [1 + \frac{u}{U_{eff}} + 2\alpha_i \frac{(V + v)}{U_{eff}}]$$

When calibrated in a steady flow

$$\frac{(E_{\ell i})_\phi}{(E_{\ell i})_{\phi=0}} = 1 + 2\alpha_i \sin\phi$$

Second order effects, which occur for angles larger than 20°, are negligible for this particular flow.

The following calibration procedure was repeated before and after each velocity profile was obtained. The probe was mounted in a specially constructed support with orientation adjustment, the "dial calibrator," that permitted a ±50° rotation of the split-film sensor about a fixed location. The sensor was supported over the potential core of the near jet produced by a TSI model 1125 calibrator. The dial calibrator was used for both the velocity and azimuthal yaw calibrations. The uncertainty in the angle was less than 0.2°. The use of the split-film probe requires closely equal temperatures of the films, so that very fine overheat adjustment of one film is mandatory to match temperatures.

Both films were exposed to 77° air flow directed along the plane of splits. Cold resistances were measured and found to be about 11 and 12 ohms. Both films were then overheated by a factor of 0.5. One film was left without further adjustment while the other film overheat was adjusted using a 1 ohm precision ten turn potentiometer. The temperature matching was achieved when the ratio of the two output bridge voltages remained constant (within 0.2%) as the velocity directed along the plane of the splits was varied from 9 fps to 70 fps. Temperature matching was checked again immediately after taking data from flow C in order to estimate any possible anemometer drift.

The bridge outputs were then each linearized and checked with the known calibrator velocity. A calibration equation of the form:

$$E_{\ell i} = C_i U_{eff} + D_i$$

was determined from a least squares fit with less than 4% standard deviation. The background noise level in the steady laminar calibrator flow was also measured. This noise took the form of a triangular wave with no phase change between channels. We suspect the noise was due to vortex shedding off of the relatively large diameter sensor. The probe was then calibrated for several azimuthal yaw angles to determine α_i. Yaw characteristics were found to be independent of the magnitude of U_{eff}.

The equations governing the split film are a combination of the above equations

$$E_{\ell i} + e_i = C_i U_{eff} \left[1 + u/U_{eff} + 2\alpha_i (V + v)/U_{eff}\right] + D_i$$

$$i = 1, 2$$

or
$$E_{\ell 1} = C_1 [U_{eff} + 2\alpha_1 V] + D_1$$

and
$$E_{\ell 2} = C_2 [U_{eff} + 2\alpha_2 V] + D_2$$

Since C_i, D_i, and α_i are known from calibration, then $E_{\ell 1}$ and $E_{\ell 2}$ are measured and U_{eff} and V are derived. The angle of flow, ϕ, at a point is then found from

$$\sin\phi = V/U_{eff}$$

Similarly, the fluctuation quantities are found from:

$$\overline{(e_{\ell 1})^2} = C_1^2\, \overline{u^2} + 4C_1^2\alpha_1\, \overline{uv} + (2C_1\alpha_1)^2\, \overline{v^2}$$

$$\overline{(e_{\ell 1} + e_{\ell 2})^2} = (C_1+C_2)^2\overline{u^2} + 4(C_1\alpha_1+C_2\alpha_2)(C_1+C_2)\overline{uv} + 4(C_1\alpha_1+C_2\alpha_2)^2\overline{v^2}$$

$$\overline{(e_{\ell 1} - e_{\ell 2})^2} = (C_1-C_2)^2\overline{u^2} + 4(C_1\alpha_1-C_2\alpha_2)(C_1-C_2)\overline{uv} + 4(C_1\alpha_1-C_2\alpha_2)^2\overline{v^2}$$

$\overline{e^2_1}$, $\overline{(e_{\ell 1} + e_{\ell 2})^2}$, and $\overline{(e_{\ell 1} - e_{\ell 2})^2}$ were measured, corrected for the above mentioned noise, and used to solve simultaneously for $\overline{u^2}$, $-\overline{uv}$, and $\overline{v^2}$ using the latter equations. These results are discussed in section 3.4 below.

The traversing mechanism used for the boundary layer velocity measurements was mounted on the supporting frame for the upper wall and provided for precise positioning of the probe sensors as described by Strickland and Simpson (1973). A cathetometer was used to accurately locate the probe sensor from the wall within an uncertainty of about ±0.001 inches. The detailed streamwise free-stream velocity distributions were obtained using a TSI model 1210-20 hot-film probe (0.002 inches diameter platinum-coated quartz rod) attached to a probe support rod inserted from the tunnel exit or mounted on the toy racing car shown in figure 3 of Simpson and Wallace (1975). The car was easily positioned along the flow by fishing line. It could not be used near the exit since substantial flow blockage effects would have been produced.

The flush surface mounted hot-film sensors for the wall "bursting" and spanwise measurements are described in detail by Strickland and Simpson (1973). The basic sensing part is a very thin layer of platinum (Engelhard Ind. Liquid Bright Platinum #05) fired on the end of a 2mm diameter quartz rod. Gold leads (Engelhard Ind. Gold Alloy Paste A-1199) were fired on the sides of the rod and short wire leads were soldered to the gold. A casing made from 1/4 inch diameter plexiglas rod was used to protect the sensor from damage due to handling.

The resulting unit was mounted in the wind tunnel wall with the platinum portion flush with the test wall. A unit containing two flush surface 0.020 inches diameter platinum sensors was also fabricated to permit one of the sensors to be traversable. This unit was used in the surface spanwise structure measurements and is described in more detail by Simpson and Wallace (1975). All of these sensors were operated at an overheat ratio of 0.03 in the current experiments. A higher overheat ratio would have permanently damaged the sensors. The constant temperature frequency response for each sensor was determined to be down 3 db at 4 KHz using the method of Freymuth (1967).

Other electronic equipment included Krohn-Hite model 3202 and 330B filters, HP model 400E rms voltmeters, an Anadex model CF-600 timer-frequency counter, a SAICOR model 41 digital correlation and probability analyzer, an Applied University Research four-channel FM tape recorder (response down 3 db at 2 KHz), a voltage comparator or schmitt trigger using an operational amplifier integrated circuit and a multiplier using an Analog Devices AD533 JH integrated circuit trimmed to within ±1% fullscale nonlinearity error. A true integrating voltmeter consisting of a voltage-controlled oscillator (Tektronix FG501 Function Generator) and a digital counter (Tektronix DC503 Universal Counter) was found to be superior to RC-type meter circuits used in most voltmeters. A HP 5451A/71A Fast Fourier Analyzer System was used to process data recorded on the tape recorder.

For the intermittency measurements in flow C, the laser optics, and photo-multiplier tube of the SMU laser anemometer (Simpson, et al., 1974) was used to scatter light from the smoke filled boundary layer and collect the signal. A focal volume of 0.32 mm diameter and 3.56 mm long was produced from a laser beam 1.1 mm in diameter at the $1/e^2$ intensity locations. Since the laser anemometer is mounted on a single traversable cart, accurate location of the focal volume could be determined.

3. EXPERIMENTAL RESULTS

3.1 Description of the test flows

Because of the strong influence of acceleration on these boundary layers, careful measurements of the freestream velocity were made every one inch along the test section using the rake and car probe mounts. For flow C the following velocity and K distributions were obtained:

$$1/U_\infty = -1.525\text{x}10^{-2} + (2.307\text{x}10^{-3})(x) - (1.133\text{x}10^{-5})(x^2)$$

for $96 \le x \le 178$ inches and

$$1/U_\infty = 4.273\text{x}10^{-1} - (2.466\text{x}10^{-3})(x) + (1.473\text{x}10^{-6})(x^2)$$

for $178 \le x \le 190$ inches with

$$K = -4.622 \times 10^{-6} + (4.5427 \times 10^{-8})(x)$$

for $96 \le x \le 185$ and $K = 3.83 \times 10^{-6}$ for $186 \le x \le 191$ inches. U_∞ is in fps and x is in inches. The maximum deviation of U_∞ data from these equations is less than 0.4% while the rms deviation is about 0.1%. The different x ranges for the $1/U_\infty$ distributions and their respective K distribution reflect the fact that the upstream velocity equation produces K values in closer agreement with data for $178<x<185$ inches. The single-sample uncertainty (Kline and McClintock, 1953) in K at 20:1 odds is about 2%.

For flow D, with both increasing and decreasing K regions, the following velocity and K distributions are presented:

$$1/U_\infty = 9.898 \times 10^{-2} + (6.568 \times 10^{-5})(x)$$

for 64 < x < 96 inches

$$1/U_\infty = -1.449 \times 10^{-1} + (5.167 \times 10^{-3})(x) - (2.675 \times 10^{-5})(x^2)$$

for 96 < x < 132 inches

$$1/U_\infty = 3.243 \times 10^{-1} - (1.917 \times 10^{-3})(x)$$

for 132 < x < 144 inches

$$1/U_\infty = 8.497 \times 10^{-1} - (9.1869 \times 10^{-3})(x) + (2.5138 \times 10^{-5})(x^2)$$

for 144 < x < 180 inches and

$$1/U_\infty = 2.475 \times 10^{-2} - (7.8147 \times 10^{-5})(x)$$

for 180 < x < 190 inches.

$$K = -1.32 \times 10^{-7} \text{ for } 64 < x < 96 \text{ inches}$$

$$K = -1.037 \times 10^{-5} + (1.0737 \times 10^{-7})(x) \text{ for } 96 < x < 132 \text{ inches}$$

$$K = 3.85 \times 10^{-6} \text{ for } 132 < x < 144 \text{ inches}$$

$$K = 1.8438 \times 10^{-5} - (1.009 \times 10^{-7})(x) \text{ for } 144 < x < 179 \text{ inches}$$

$$K = 1.568 \times 10^{-7} \text{ for } 180 < x < 190 \text{ inches}$$

The maximum deviation of U_∞ data from these equations is less than 1% while the rms deviation is about 0.2%. The discontinuity in K at the ends of each region is of the order of 10^{-7}. The single-sample uncertainty in K is about 4%. The smoothed K distributions for both flows C and D are shown in figure 2.

As was done for flows A and B, observations were made to assess the three-dimensionality of flows C and D. Because of the care used in adjusting the spanwise elements of the upper wall parallel to the test wall, the thin boundary layers in a large aspect ratio channel, and the fact that the flow was accelerating, minimal three-dimensional effects were expected. At the 88 inches location there was less than 1% spanwise difference in the momentum thickness, so no gross three-dimensionality due to the upstream flow was present. The side wall boundary layers of the converging section for each flow tended to remain at about a constant thickness due to the reduction of the side wall surface area simultaneously with acceleration of the freestream. Thus convergence or divergence effects on the test wall boundary layer by the side wall boundary layers appears to be negligible.

As discussed in section 3.3 below, the skin friction was deduced by analyzing mean velocity profiles near the wall. The smoothed "best estimate" skin friction coefficients and other required and experimentally deduced quantities were used to check the balance of terms in the two-dimensional momentum integral equation. In both flows C and D this equation was balanced well within the uncertainty of the most uncertain term, $d\theta/dx$, or about 5% of that term.

3.2 Mean velocity profile measurements

Figure 3 shows the mean velocity profile results for flow C. A distinct logarithmic region exists for each upstream profile, with the last evidence of any logarithmic region occurring at about station 160 inches. As shown in figure 4, the shape factor H is near a minimum at station 165 inches. The wake-like tail of each profile near the freestream is observed to progressively decrease in wake strength,

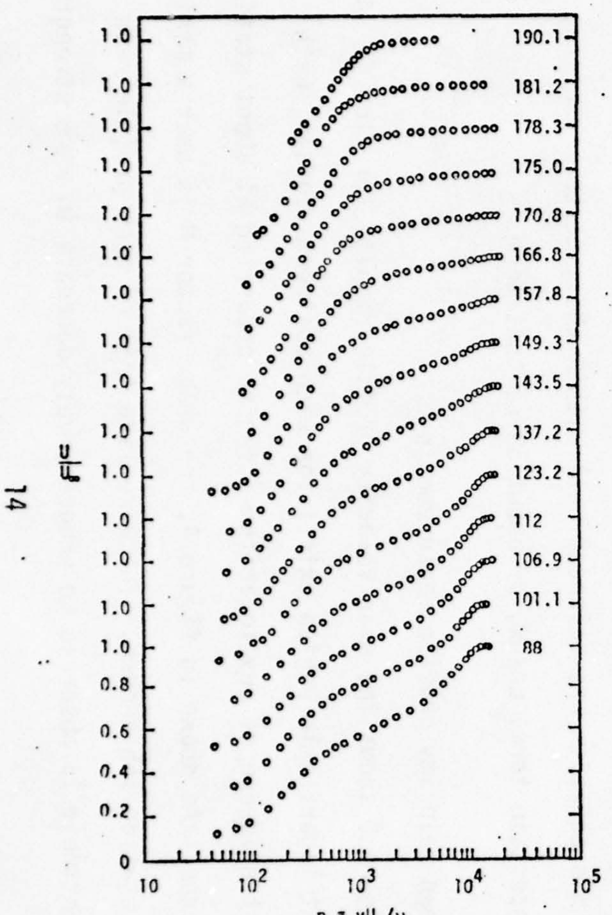

Figure 3. Experimental mean velocity profiles for flow C, linearly increasing K. Note displace ordinates. Station position in inches at right of each profile.

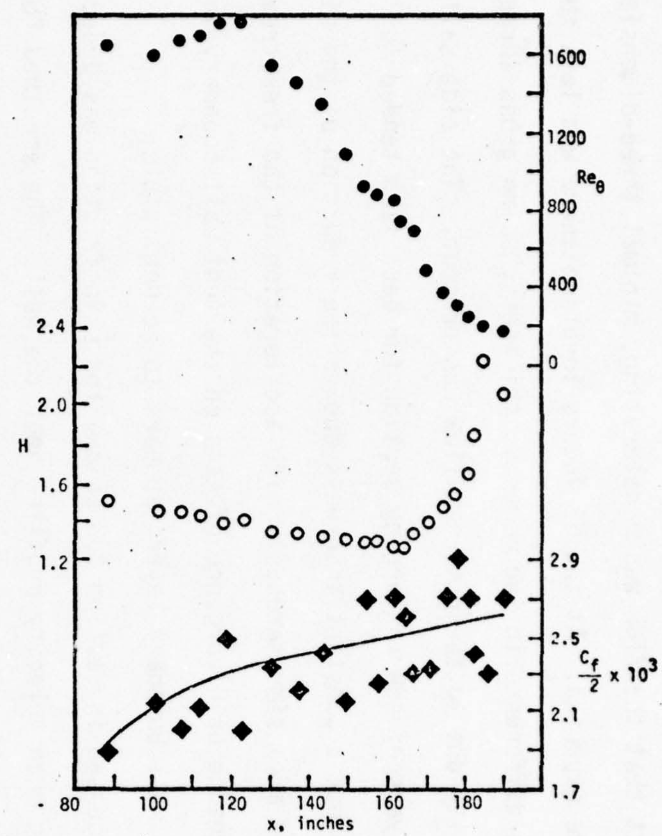

Figure 4. Re_θ, H, and $C_f/2$ for flow C. Friction factors from table 1: solid symbols - wall profile results; line - best estimate curve.

Station (inches)	U_∞^a (fps)	$(K\times10^6)^b$	Re_θ	H	$\delta_{0.99}$ (inches)	$\frac{C_f}{2}\times10^3$ wall profile ±15%	$\frac{C_f}{2}\times10^3$ best estimate[c] ±15%
88.0	8.94	-0.59	1647	1.505	2.62	1.90	1.93[d]
101.1	8.51	-0.029	1600	1.456	2.81	2.15	2.14[d]
106.9	8.59	0.234	1681	1.450	2.91	2.04	2.20
112.0	8.80	0.466	1698	1.437	2.90	2.12	2.23
117.9	9.27	0.733	1765	1.388	2.91	2.48	2.27
123.2	9.71	0.974	1778	1.407	2.89	2.01	2.30
130.6	10.06	1.31	1546	1.344	2.74	2.32	2.34
137.2	10.79	1.61	1465	1.341	2.62	2.2	2.38
143.5	11.42	1.90	1353	1.320	2.53	2.40	2.41
149.3	12.10	2.16	1096	1.313	2.24	2.15	2.44
154.5	13.36	2.40	923	1.290	2.02	2.7	2.46
157.8	14.00	2.55	890	1.307	1.94	2.25	2.48
162.0	15.53	2.74	868	1.274	1.77	2.7	2.50
164.2	16.67	2.84	747	1.262	1.60	2.6	2.51
166.8	17.89	2.96	697	1.335	1.47	2.30	2.52
170.8	20.42	3.14	484	1.407	1.09	2.32	2.54
175.0	23.98	3.33	373	1.481	0.698	2.70	2.56
178.3	29.62	3.48	314	1.559	0.395	2.9	2.57
181.2	33.12	3.61	257	1.647	0.302	2.7	2.58
182.3	36.11	3.66	264	1.850	0.197	2.4	2.58
185.8	44.46	3.82	201	2.223	0.098	2.3	2.60
190.1	80.30	3.83	182	2.049	0.048	2.7	2.61

(a) measured when velocity profile measured.
(b) from least squares fit of rake and cart data.
(c) with exceptions noted, from faired curve of data on figure 4.
(d) determined from logarithmic velocity profile, equation (5).

Table 1. Values of parameters along flow C.

the wake strength being defined as the maximum deviation of the measured velocity profile from the extrapolated logarithmic region profile. Downstream of the location of the minimum H the velocity profiles take on an increasingly more laminar-like character, although the streamwise fluctuation measurements clearly show that a relatively large turbulence intensity still exists. Since the last 5 inches of the test flow has a constant K of about 3.83×10^{-6}, this is the only region where constant K asymptotic velocity profile similarity of $f(=U/U_\infty)$ and $\eta(=yU_\infty/\nu)$ is possible. In this region the velocity profiles for $\eta > 1000$ are similar well within a deviation of 0.01 f. However, the streamwise fluctuation intensity profiles discussed in section 3.4 do not posses similarity in this region and H and Re_θ do not reach constant values, as required for true asymptotic similarity (Simpson and Wallace, 1975). Re_θ drops well below the value of about 360 (Kays 1966) where normal transition from a laminar to turbulent boundary layer occurs, so true laminar behavior could be expected downstream had the test section been longer and the level of acceleration maintained.

Flow D also has a linearly increasing K distribution but only for $x < 132$ inches. dK/dx is more than twice that for flow C. As in flow C, the initial upstream logarithmic velocity profile progressively decays downstream. Figure 5 shows that the wake strength also decreases to zero near the minimum H location, shown at about 135 inches in figure 6. The location of the minimum H occurs in the region where K is a maximum, while in flow C it occurs at a much

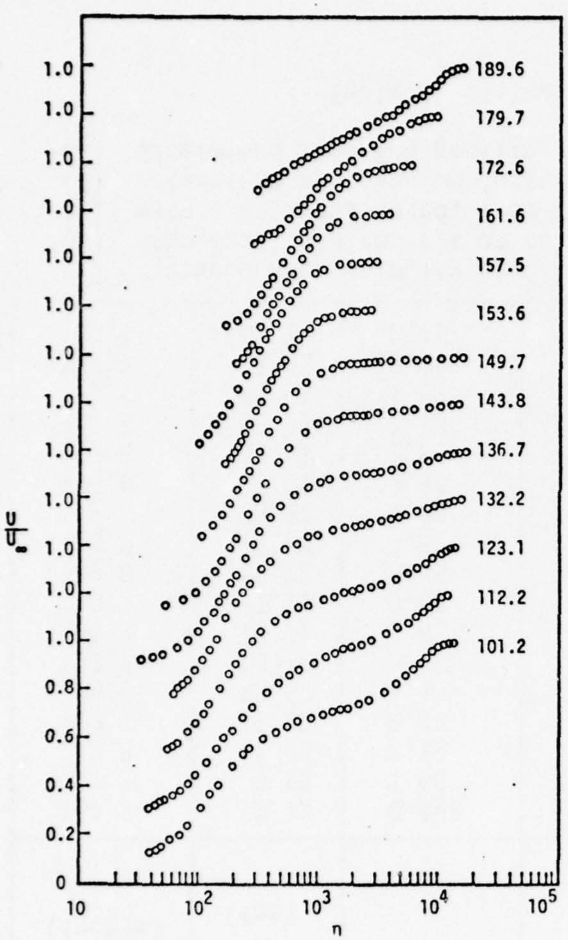

Figure 5. Mean velocity profiles for flow D. Streamwise location in inches to right of each profile. Note displaced ordinate scales.

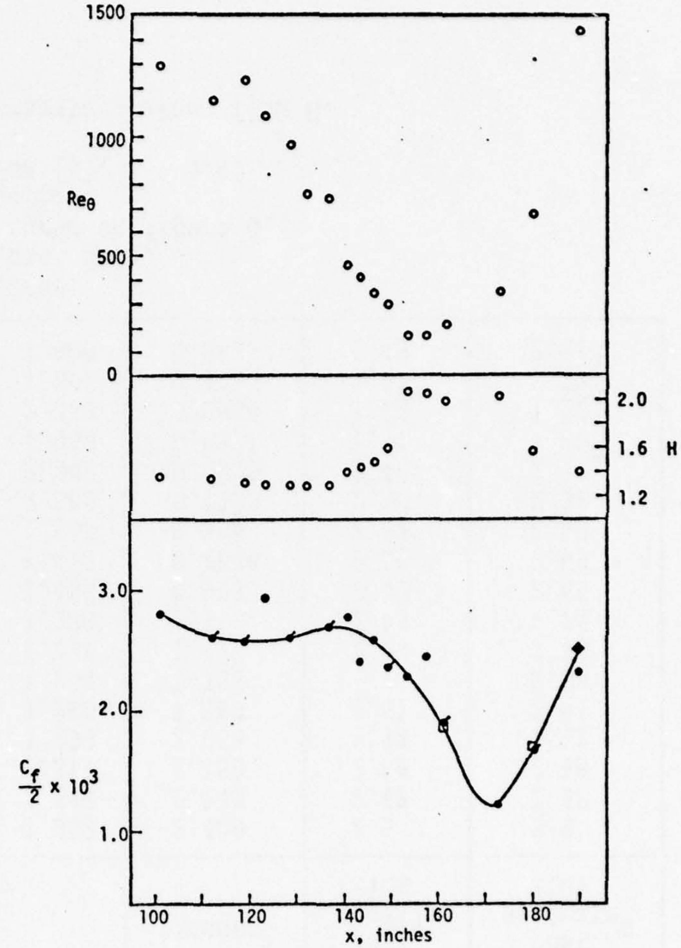

Figure 6. Re_θ, H, and $C_f/2$ for flow D. $C_f/2$ values from table 2: ◐, unshifted wall profile; ●, shifted wall profile; ◆, logarithmic profile with K = 0.4; □, momentum integral equation.

Station (inches)	U_∞^a (fps)	$(K\times10^6)^b$	Re_θ	H	$\delta_{0.99}$ (inches)	$\frac{C_f}{2}\times10^3$ wall profile ±10%	best estimate[c] ±10%
101.2	9.12	0.495	1294	1.352	2.409	2.9	2.9
112.2	9.55	1.68	1156	1.346	2.243	2.62	2.62
118.8	11.26	2.39	1236	1.311	2.168	2.58	2.58
123.1	11.22	2.85	1087	1.293	2.053	2.94	2.58
128.6	13.53	3.44	965	1.286	1.889	2.61	2.61
132.2	13.72	3.85	761	1.264	1.756	?	2.65
136.7	16.71	3.85	740	1.281	1.477	2.70	2.70
140.7	17.75	3.85	464	1.388	1.113	2.79	2.70
143.8	21.02	3.85	419	1.436	0.908	2.42	2.65
146.8	22.67	3.62	347	1.478	0.7544	2.60	2.59
149.7	26.37	3.33	307	1.583	0.535	2.37	2.49
153.6	30.68	2.94	168	2.069	0.1183	2.30	2.32
157.5	37.81	2.55	166	2.043	0.0900	2.46	2.12[d]
161.6	48.39	2.13	219	1.980	0.0871	1.91	1.87[d]
172.6	83.55	1.02	355	2.028	0.0984	1.22	1.22[d]
179.7	94.82	0.306	677	1.567	0.1436	1.67	1.72[d]
189.6	102.1	0.157	1432	1.408	0.2477	2.43	2.54[e]

(a) measured when velocity profile measured.
(b) from least squares fit of rake and cast data.
(c) with exceptions noted, from faired curve on figure 6.
(d) determined by momentum integral equation.
(e) determined from log profile, equation (5), Ω = 0.40.

Table 2. Values of parameters along flow D.

lower K value. Downstream the profiles assume an increasingly more laminar-like character as Re_θ drops below 360 until about 157.5 inches, even though K decreases downstream of 144 inches. No profile similarity is observed.

Between 157.5 inches and about 172.6 inches the momentum and displacement thicknesses, θ and δ^*, remain about constant, giving rise to about a constant shape factor ($H \equiv \delta^*/\theta$) of about 2.0. As noted in section 3.7 below, intermittency measurements downstream of 157.5 inches indicate that considerable turbulence is redeveloping. At the 189.6 inches location a thick logarithmic region $500 < \eta < 5000$ is observed, so that this flow is developing into a typical low acceleration turbulent boundary layer. The wake strength is also observed to be increasing.

Simpson and Wallace (1975) found that for each of flows A and B the location of the H minimum was closely related to where the wake strength was zero and where entrainment of free-stream fluid ceased. For flows C and D, the mass flux in each boundary layer as reflected by $U_\infty(\delta - \delta^*)$ increases until about 165 inches and 135 inches, respectively, as shown in figures 7 and 8. This parameter decreases downstream in both flows but again increases downstream of about 157.5 inches in flow D as a low acceleration turbulent boundary layer develops. These plots of experimentally deduced values indicate that there was entrainment of non-turbulent fluid into each boundary layer until the minimum H locations. As in the cases of flows A and B, the intermittency measurements discussed below indicate that after the

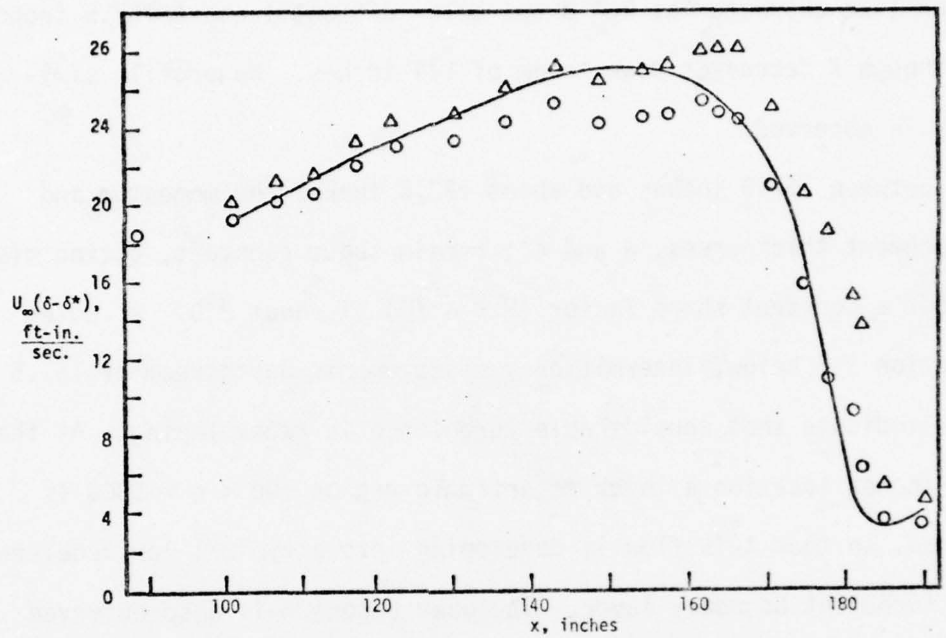

Figure 7. Mass flux in boundary layer of flow C, $U_\infty(\delta-\delta^*)$: O, $\delta = \delta_{0.99}$; △, $\delta = \delta_{0.995}$. Solid line - equation (21) results.

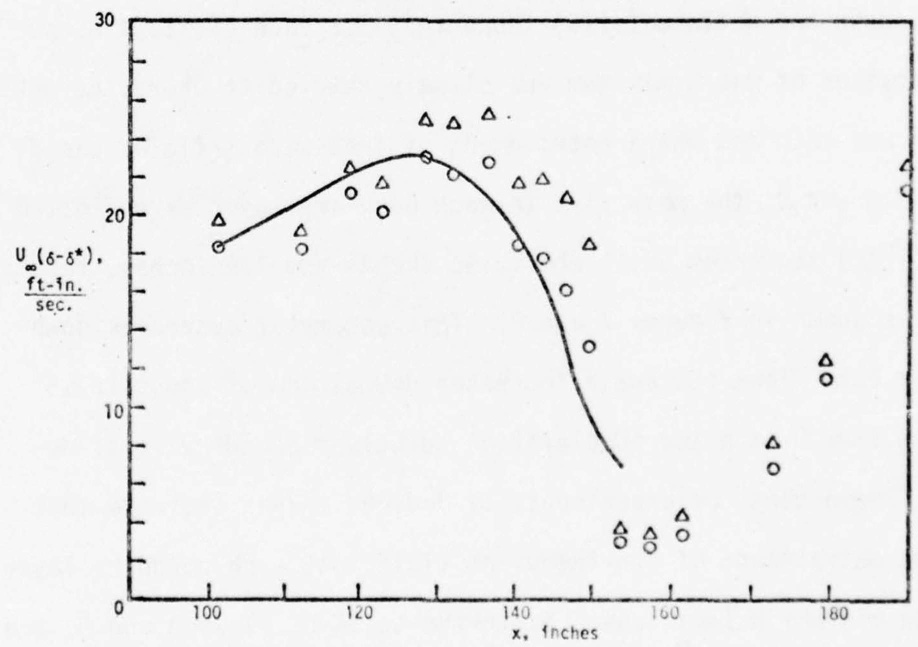

Figure 8. Mass flux in boundary layer of flow D, $U_\infty(\delta - \delta^*)$: O, $\delta = \delta_{0.99}$, △, $\delta = \delta_{0.995}$. Solid line - equation (21) results.

cessation of entrainment the intermittent turbulent/non-turbulent region lies outside δ. Thus there is no mean velocity gradient $\partial U/\partial y$ and no wake-like tail in this region and no mechanism for engulfment of non-turbulent fluid by the intermittent bulges is possible. The model proposed by Simpson and Wallace for the entrainment process in a strongly accelerated boundary layer is discussed in section 4 below.

3.3 Skin-friction results

The skin-friction coefficient $C_f/2$ was primarily determined by two methods: the velocity profile near the wall and the logarithmic velocity profile relationship for unaccelerated flow regions. The momentum integral equation

$$\frac{C_f}{2} = \frac{d\theta}{dx} + KRe_\theta(2 + H) \qquad (1)$$

was used some for flow D when both terms of the right side were positive and relatively certain.

The velocity profile near the wall can be derived from the differential momentum equation, neglecting the convective and turbulent transport terms:

$$\nu \frac{\partial^2 U}{\partial y^2} = \frac{1}{\rho}\frac{dP}{dx} = \frac{-U_\infty^3 K}{\nu} \qquad (2)$$

Integrating equation (2) produces

$$\frac{C_f}{2} = \frac{\partial f}{\partial \eta} + K\eta \qquad (3)$$

and the velocity profile upon integration of equation (3)

$$\frac{U}{U_\infty} = f = \frac{C_f}{2}\eta - \frac{K\eta^2}{2} \qquad (4)$$

Equation (4) was used with experimental velocity measurements for $5 \le y^+ = \eta\sqrt{C_f/2}$ to determine $C_f/2$. Oka and Kostić (1972) noted that hot-film and hot-wire measurements are strongly influenced by conduction to the test wall for $y^+ < 4$. For velocity profiles with logarithmic regions it is known that equation (4) does not well describe the velocity profile for $y^+ > 6$, so only points in the range $5<y^+<6$ were used. For the more laminar-like profiles experimental data with $y^+ > 6$ were also used.

Logarithmic velocity profiles in unaccelerated or weakly accelerated flow regions are described by the relation

$$\frac{U}{U_\infty\sqrt{\frac{C_f}{2}}} = \frac{1}{\Omega}\,\ln\left|\eta\left(\frac{C_f}{2}\right)^{1/2}\right| + C \tag{5}$$

where $\Omega = 0.40\,(Re_\theta/6000)^{-1/8}$ (Simpson, 1970) for low Reynolds number boundary layers with $Re_\theta < 6000$. A fit of equation (5) to experimental data was made for the two upstreammost profiles of flow C and to the downstreammost profile of flow D. In the latter case $\Omega = 0.40$ was used since a large logarithmic region that normally accompanies high Reynolds number boundary layers was observed. Results using this latter method are about ±10% uncertain.

For flow C the 0.001 inches diameter cylindrical hot-film sensor was located from the test wall within an uncertainty of about 0.001 inches. Considering the ±1/2% uncertainty of the velocity, the $C_f/2$ values shown in figure 4 appear to be about ±15% uncertain at 20:1 odds. This uncertainty value seems reasonable due to the scatter of the data. The logarithmic velocity profile results from equation (5) are in close agreement with these results.

For flow D the 0.00015 inches diameter hot-wire sensor was located from the test wall with somewhat more uncertainty than for flow C since the wire was more difficult to illuminate and to observe by the cathetometer. This more fragile sensor was located at a safe distance of about 0.005 inches from the wall to prevent breaking the wire. Data from this smaller diameter sensor are less suceptible to velocity gradient effects so the near wall velocity profiles for $y^+ > 4$ are believed to be of higher quality than those of flow C. For each velocity profile point a least squares fit of equation (4) to the five surrounding data points was made to deduce the slope $\partial f/\partial n$ at that point. $C_f/2$ can be eliminated from equations (3) and (4) to produce

$$\eta = \frac{-\frac{\partial f}{\partial n} + \sqrt{\left(\frac{\partial f}{\partial n}\right)^2 + 2Kf}}{K} \qquad (6)$$

from which the proper sensor distance from the test wall could be computed from K, f, and $\partial f/\partial n$. For flow D equation (6) was used to determine the required change in the y direction for a self-consistent velocity distribution near the wall. Values within about 5% of one another were obtained for successive points in a given velocity profile. As given in Appendix B these shifts in the y direction are no more than ±0.005 inches and therefore are reasonable.

Figure 6 shows relatively less scatter in the wall profile results than shown for flow C, thus an estimated uncertainty of ±10%

seems reasonable. The logarithmic profile $C_f/2$ result at 189.6 inches is in good agreement with the $C_f/2$ result from equation (4) with no y direction shifting. Results from equation (1) at 161.6 and 179.7 inches are also in good agreement with the wall profile results.

Smooth curves of "best estimate" values for $C_f/2$ are shown on figures 4 and 6 with values given in Tables 1 and 2. While these curves were just faired among the points shown on those figures within about 15% and 10%, respectively, they are probably representative of the variation of $C_f/2$ along each flow. From the laminar sink flow (Schlichting, 1968), i.e. a constant K flow, one can obtain the expression

$$\frac{C_f}{2} = \sqrt{\frac{4}{3} K} \qquad (7)$$

so for the maximum K of about 3.83×10^{-6} achieved in these two flows, $C_f/2 = 2.26 \times 10^{-3}$. Near the maximum K for each of flows C and D the experimental $C_f/2$ values are above this value as they should be since considerable turbulent momentum transport is still present. While one cannot exactly compare results from different K distributions, it is interesting that the experimental results shown in figure 6 for flow D are always greater than or about equal to those given by equation (7) with the local K value. In the region near 165 inches where the turbulence intermittency is near zero at the wall, as discussed in section 3.7 below, the skin friction values are about equal. Downstream of this region the experimental $C_f/2$ values increase rapidly as turbulence redevelops.

3.4 Reynolds stresses distributions

Figures 9 and 10 show intensity $\sqrt{\overline{u^2}}/U_\infty$ profiles for flows C and D from the fluctuation portion of the linearized hot-film and hot-wire signals. In flow C the maximum intensity remains at about 0.1 and is located in the range of $300 < \eta < 400$ up until $K > 3.6 \times 10^{-6}$ at about 181 inches, after which the normalized intensity decays and the maximum intensity location moves to a greater η value. The hump in the outer region of the upstream intensity profiles vanishes just downstream of the cessation of entrainment at about 165 inches. Between 165 inches and 181 inches the acceleration of the wall region flow alone is apparently sufficient to maintain the same level of turbulence production as upstream. In other words the entrainment of high momentum free-stream fluid performs no role.

Flow D exhibits the same behavior but the outer region hump does not completely vanish until about 143.8 inches. The maximum intensity is located in the range of $200 < \eta < 400$. Beginning at about 153.6 inches, where $C_f/2$ begins to drop rapidly, the value and n location of the maximum intensity decreases. After retransition to a low acceleration turbulent boundary layer begins, the maximum intensity remains at about 0.08 but the η location of the maximum increases. At 189.6 inches the intensity profile of a normal low acceleration turbulent boundary layer is emerging.

The split-film probe was used to determine $\overline{u^2}$, $\overline{v^2}$, and $-\overline{uv}$ for flow C. No split-film probe measurements were attempted for flow D. The mean velocity profiles showed very good agreement with those

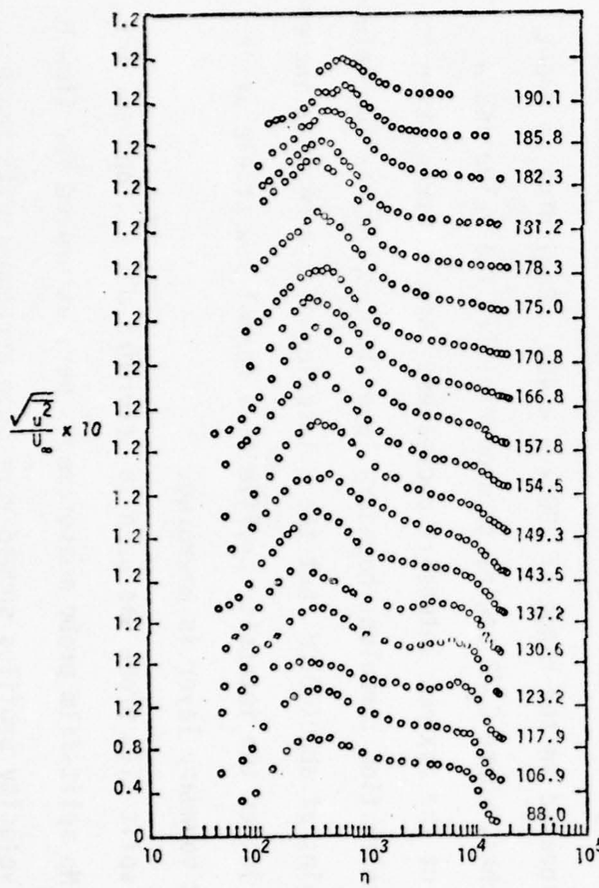

Figure 9. Streamwise intensity profiles for flow C. Note displaced scales. Station position in inches at right of each profile.

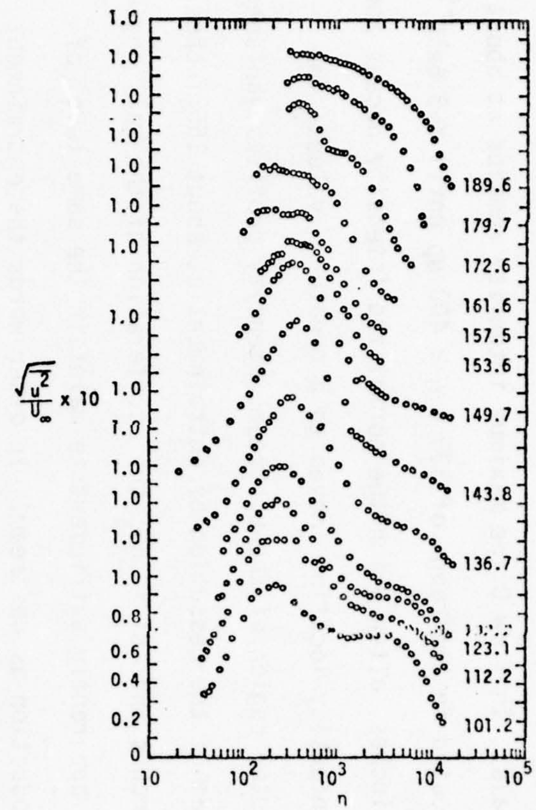

Figure 10. Streamwise intensity profiles for flow D. Note displaced scales. Station position in inches at right of each profile.

measured with a single film boundary layer probe. The deviation was within the uncertainty of the calibration except at locations 171.3, 178.8, and 187.6 inches. At these locations the mean velocities below $\eta = 10^3$ were as much as 47% high nearest the wall yet were less than 2% high at $\eta=10^3$ and were less than 0.5% high at η = 1300 and beyond. At locations 101.7, 137.8, 149.6 and 162.4 inches, the mean velocity deviated from the single film probe by less than 3% from the wall to the freestream. The large deviation near the wall at higher freestream velocities may be due to the significantly greater velocity gradient effects which tend to cool the top film more than the bottom film.

The V component of velocity, when normalized against U_{eff} allowed comparison of the angle of flow ϕ with respect to the test wall since $\sin \phi = V/U_{eff}$. After accounting for the angle of the plane of the splits with the test wall, the angle of flow measured by the split-film probe at a point in the freestream was at worst within 1.4° of the flow angle at that point derived from the displacement thickness gradient and freestream velocity gradient. This difference is beyond 0.6° uncertainty in computing ϕ from the calibration equations plus the 0.2° uncertainty in ϕ due to approximation of the displacement thickness gradient. However, for 6 of the 8 profiles taken, the angles measured agree within that 0.6° uncertainty in ϕ.

The $\overline{u^2}$ fluctuations, as seen in figure 11, tend to show very poor agreement with those measured with the single film probe for $\eta < 10^3$. At x = 137.8 and 149.6 the discrepancy is apparent to

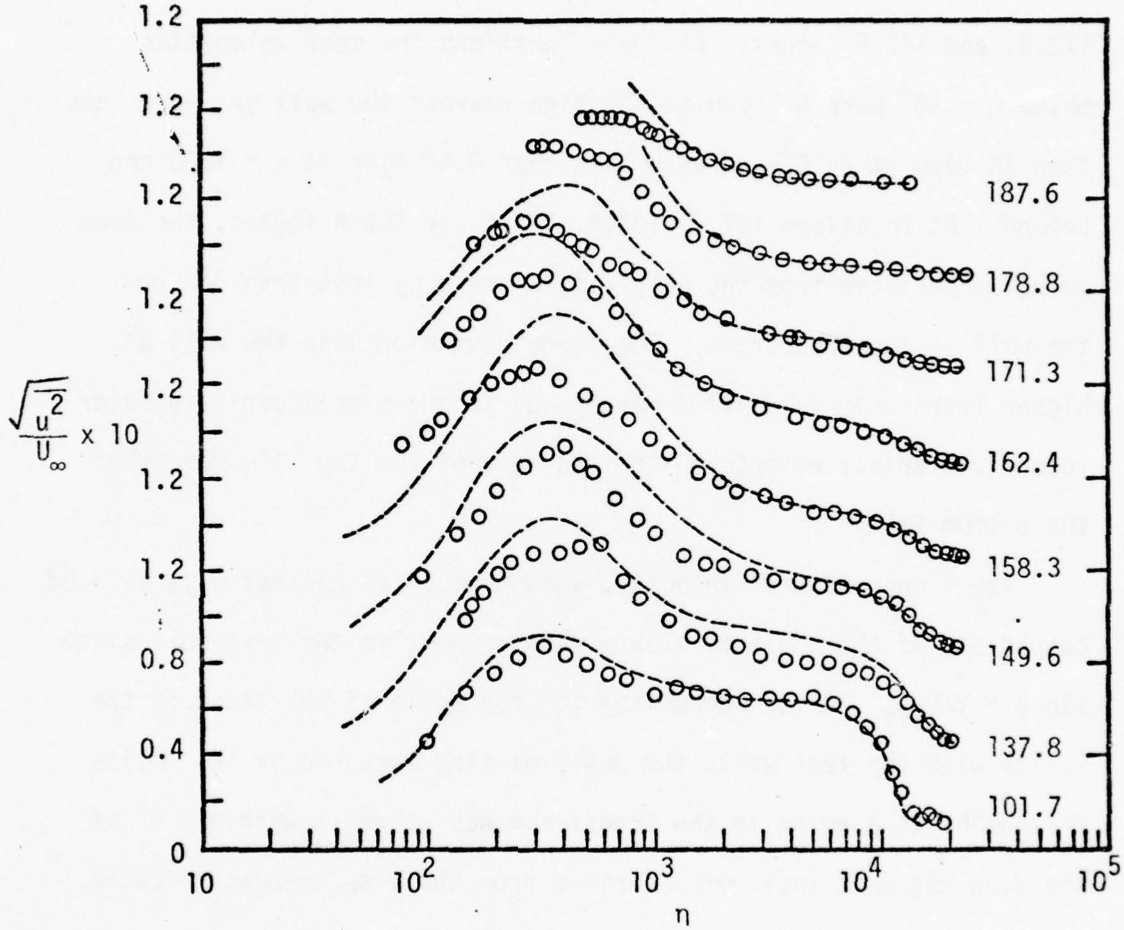

Figure 11. Streamwise fluctuation distributions from the split-film sensor for flow C. Profile location in inches at right of each profile. Dashed lines - normal hot-film results from figure 9 for nearby location. Note displaced ordinate scales.

$\eta = 10^4$. In all other cases the agreement is good from $\eta = 10^3$ to the freestream except at x = 158.3 where agreement is poor until η reaches 5000. The kinematic Reynolds shearing stress $-\overline{uv}$ also shares the $\eta = 10^3$ cutoff above which the data begin to seem reasonable. There is a rapid decrease in $-\overline{uv}$ as the flow accelerates as shown in figure 12. Also shown on this figure is the shearing stress profile for 190.1 inches generated from the momentum equation and U/U_∞ vs. η similarity. The outer region mean velocity profiles at 185.8 and 190.1 inches are similar well within 0.01 in U/U_∞ and K is constant. Thus the similarity assumptions are met for an asymptotic flow and the equation

$$\frac{-\overline{uv}}{U_\infty^2} = K \int_\eta^\infty (1 - f^2)d\eta - \frac{df}{d\eta} \tag{8}$$

describes the Reynolds shearing stress (Simpson and Wallace, 1975). The agreement must be considered good for $\eta > 2600$. Thus the results from the split-film for $-\overline{uv}$ are credible at least in locations where $\overline{u^2}$ is credible. The $\overline{v^2}$ quantities measured by the split-film are high in the viscous sublayer due to the high velocity gradient there. The data in the outer region, $\eta > 3000$, are more believable.

Many problems were encountered in using the split-film sensor. The calibration process was time-consuming and frequent checks were required to overcome anemometer drift. Anemometer drift at times caused the films to operate with different temperatures, thus producing thermal interference between films as well as introducing a slight velocity dependence on the yaw characteristics. The resistance

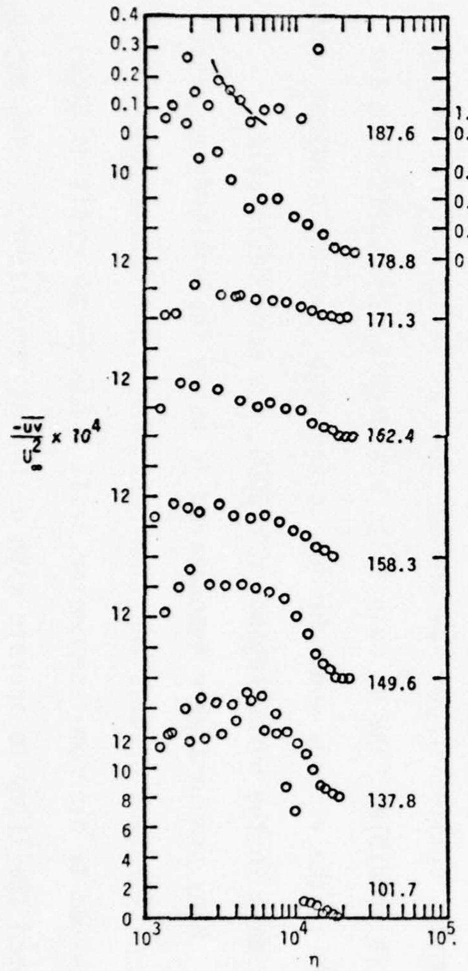

Figure 12. Reynolds shearing stress distributions from split-film sensor for flow C. Profile location in inches at right of each profile. Dashed line - mean velocity profile similarity result from eqn. (8). Note displaced ordinate scale.

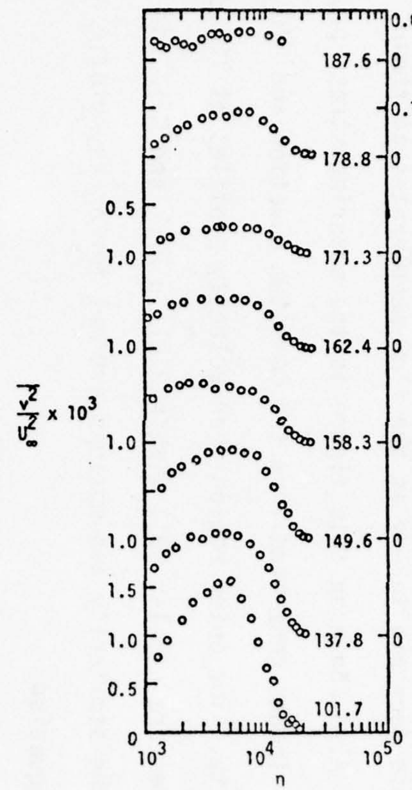

Figure 13. $\overline{v^2}/U_\infty^2$ distributions from the split-film sensor for flow C. Profile location in inches at right of each profile. Note displaced ordinate scales.

of the probe support structure sometimes changed when the probe was unplugged and then replaced in its support. Vortex shedding from the sensors produced high noise levels at increasing velocities. This noise introduced greater uncertainty in the fluctuation quantities. Velocity gradients near the wall produced unusually high V values at those points where V should be lowest. Several schemes were tried to correct for the influence of the high velocity gradient. Unfortunately, those corrections did not produce consistent results.

This experience with the split-film probe seems to be reasonably consistent with that of Sandborn (1976). He found $\sqrt{\overline{u^2}}/U_\infty$ to be closely the same as that measured by a single hot wire parallel to the test wall. $-\overline{uv}$ values from split-film data appeared to be close to the estimated true shear stress profile away from the wall where velocity gradients are sufficiently small. On the other hand, Young (1976) found that the split-film probe consistently produced a low $\sqrt{\overline{u^2}}$ by about 22% and a low $-\overline{uv}$ by about 26% in a two-dimensional channel flow. Thus, clearly the split-film results should be critically compared with results from other sensors for consistency.

3.5 Spectra measurements and dissipation estimates

The spectrum function F(n) of $\overline{u^2}$ was obtained throughout each boundary layer at several streamwise locations, where

$$\overline{u^2} \int_0^\infty F(n)dn = \overline{u^2} \qquad (9)$$

and n is the frequency in Hz. Simpson and Wallace (1975) discovered that a portion of F(n) varied like n^{-1} for locations in the region $\eta > 1000$ after the cessation of entrainment in flow B. They found that Tchen's high mean vorticity spectral model (Hinze, 1975) relating F(n) to the turbulence dissipation ε by

$$\frac{\varepsilon\nu}{U_\infty^4} = \frac{3}{2}\,\alpha[nF(n)]\left(\frac{\overline{u^2}}{U_\infty^2}\right)\frac{\partial f}{\partial \eta} \qquad (10)$$

seemed to hold.

Their data indicate that α is about 0.77 for flow B. Data from flow B were reanalyzed using equation (10) above. Equation (21) of Simpson and Wallace should have contained $\overline{u^2}$. The spectral data of Laufer (1954) in the logarithmic region of a pipe flow indicate that $\alpha \approx 0.88$ while Klebanoff's (1955) flat plate turbulent boundary layer produced flat nF(n) spectra with $\alpha \approx 0.80$. In both of these latter cases, ε was evaluated by the equilibrium relationship

$$\varepsilon = -\overline{uv}\,\frac{\partial U}{\partial y} \qquad (11)$$

that is applicable for the logarithmic velocity profile region (Rotta, 1962). Here we wish to examine the spectra obtained for flows C and D and the range of applicability of equation (10) using $\alpha = 0.8$.

Representative first moments of the spectra nF(n) for flows C and D are presented in figures 14 through 23. The hot-film and hot-wire sensor response was down 5% at 15 KHz, and 25 KHz, respectively. The data were recorded on tape and processed on the fast Fourier analyzer with a bandwidth of 2 Hz and 50 seconds record times. The

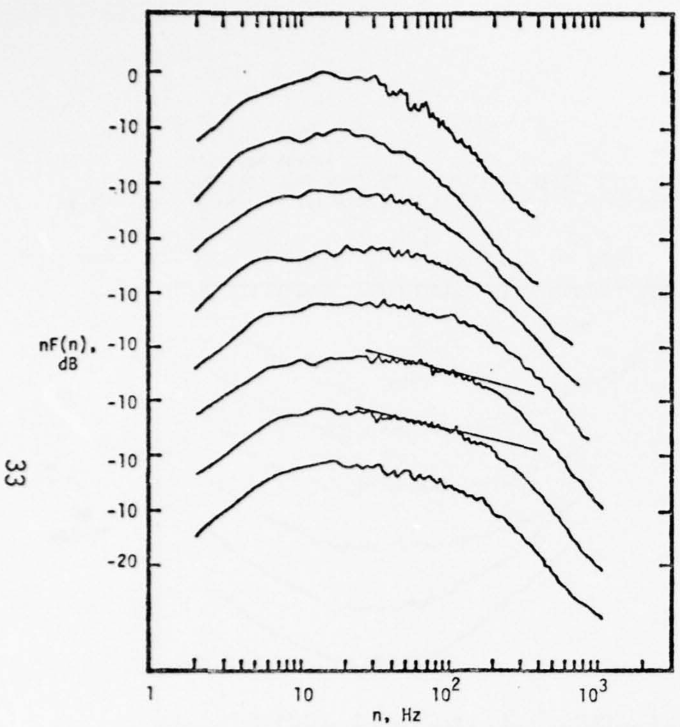

Figure 14. $\overline{u^2}$ spectra for flow C at 137.2 inches; from top to bottom η = 54, 108, 350, 673, 1346, 2154, 4307, and 8076. Note displaced ordinate scales. Straight lines, $n^{-2/3}$ slope.

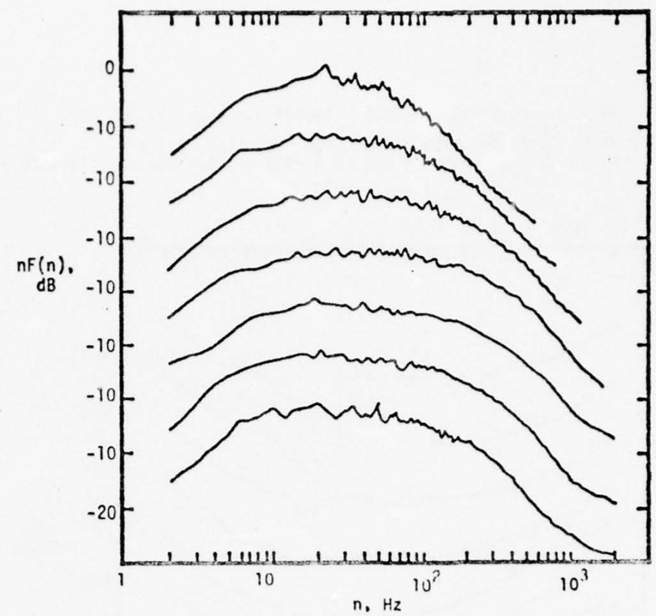

Figure 15. $\overline{u^2}$ spectra for flow C at 157.8 inches; top to bottom η = 70, 454, 873, 1397, 2794, 5589, and 8733. Note displaced ordinate scales.

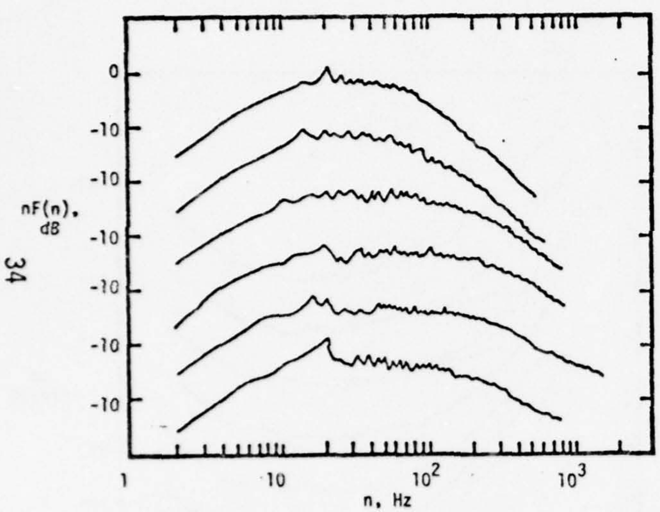

Figure 16. $\overline{u^2}$ spectra for flow C at 170.8 inches; top to bottom n = 153, 306, 815, 1528, 3057, and 8152. Note displaced ordinate scales.

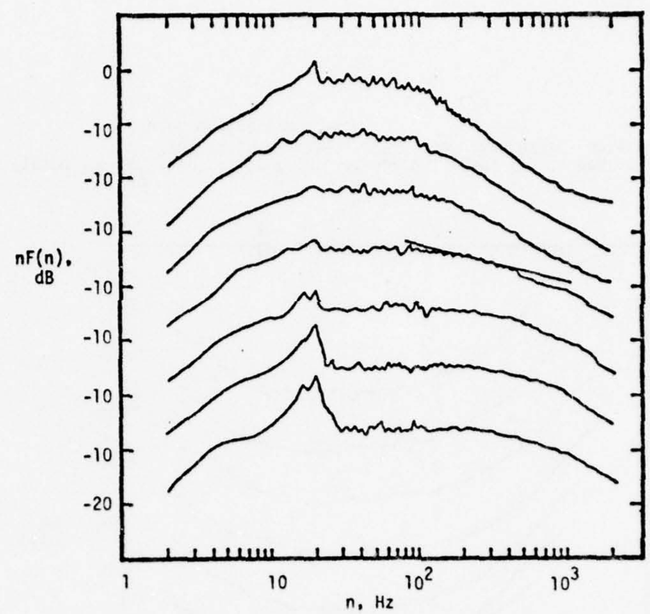

Figure 17. $\overline{u^2}$ spectra for flow C at 182.3 inches; top to bottom n = 180, 541, 901, 1532, 2252, 3604 and 7208. Note displaced ordinate scales. Straight line, $n^{-2/3}$ slope.

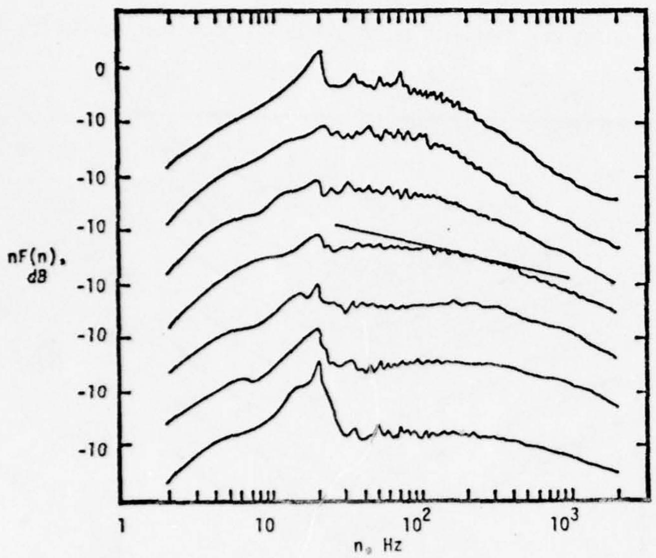

Figure 18. $\overline{u^2}$ spectra for flow C at 185.8 inches; top to bottom η = 222, 444, 887, 1331, 1886, 2662, and 7765. Note displaced ordinate scales. Straight line, $n^{-2/3}$ slope.

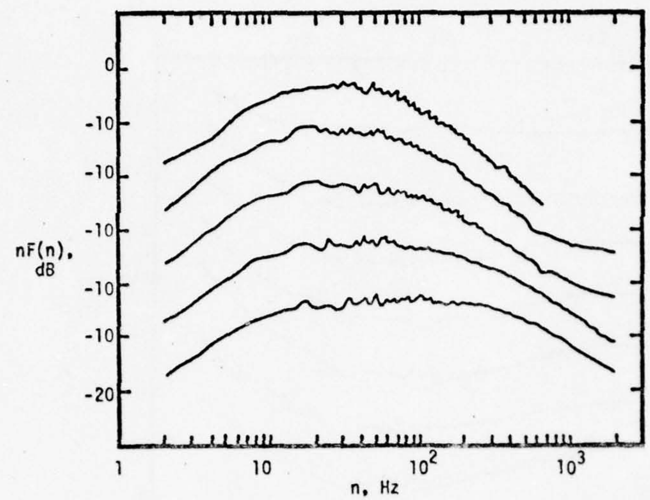

Figure 19. $\overline{u^2}$ spectra for flow D at 153.6 inches; from top to bottom η = 153, 367, 673, 1131, and 2201. Note displaced ordinate scales.

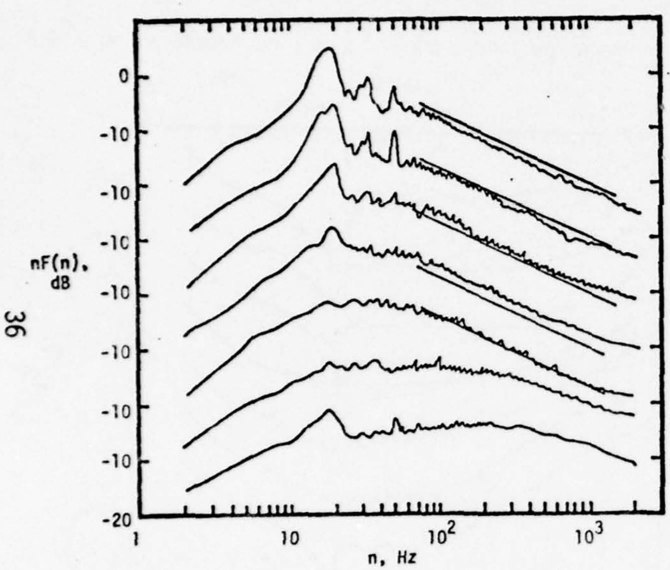

Figure 20. $\overline{u^2}$ spectra for flow D at 161.6 inches; from top to bottom n = 135, 231, 328, 473, 834, 1919 and 3848. Note displaced ordinate scales. Straight lines, $n^{-1.3}$ slope.

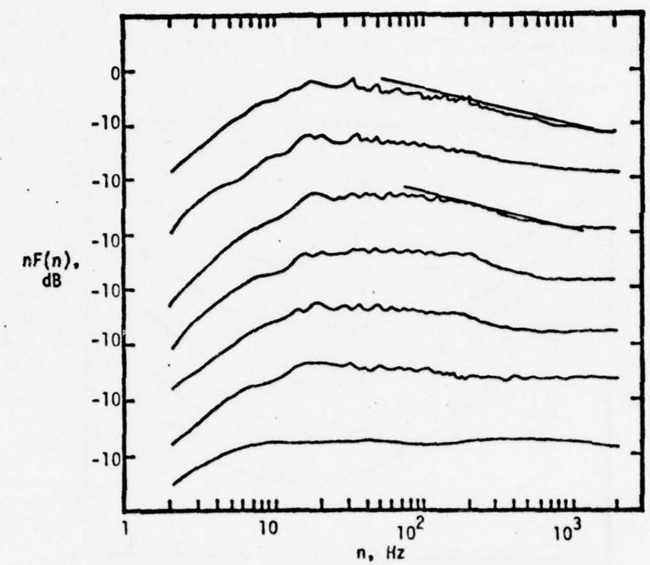

Figure 21. $\overline{u^2}$ spectra for flow D at 172.6 inches; from top to bottom n = 333, 791, 1166, 1582, 2623, 4288 and 6786. Note displaced ordinate scales. Straight lines, $n^{-2/3}$ slope.

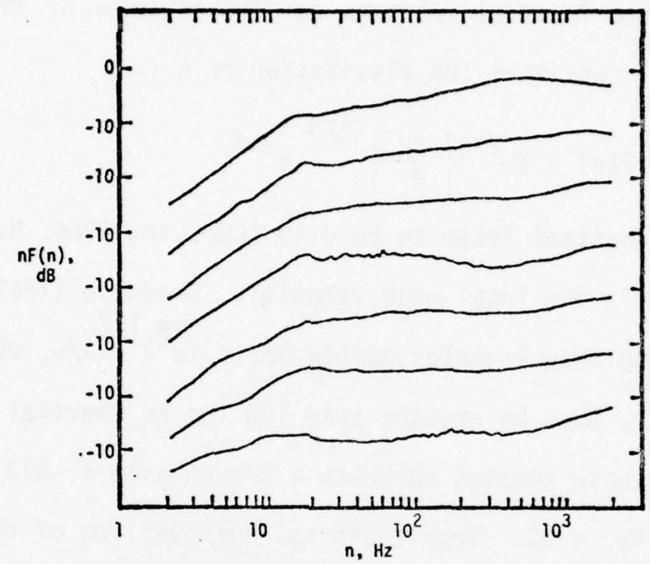

Figure 22. $\overline{u^2}$ spectra for flow D at 179.7 inches; from top to bottom η = 283, 945, 1890, 3780, 5669, 7559, and 9449. Note displaced ordinate scales.

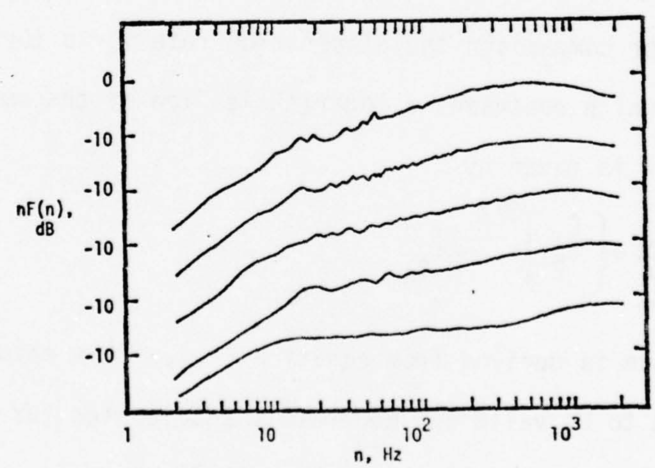

Figure 23. $\overline{u^2}$ spectra for flow D at 189.6 inches; from top to bottom η = 305, 2034, 4069, 8138, and 15259. Note displaced ordinate scales.

2 KHz upper frequency limit on the analyzer was not a serious limitation except for the data at the downstream stations in flow D.

For several of the spectral distributions, a small range of the -5/3 law of the inertial subrange existed as shown in figure 14, so it was used to estimate the dissipation rate ε:

$$\overline{u^2}\, F(n) = K\varepsilon^{2/3} \left(\frac{2\pi}{U} \right)^{-2/3} n^{-5/3} \qquad (12)$$

Here K is a constant taken to be 0.49 (Corrsin, 1964; Bradshaw, 1967a) and U is the local mean velocity. Bradshaw (1967b) suggested that the turbulence Reynolds number $Re_\lambda = (\overline{u^2})^{1/2} \lambda/\nu$, where $\lambda^2 = 15\nu\, \overline{u^2}/\varepsilon$, must be greater than 100 for an inertial subrange to exist. For those spectra on which a region with a -5/3 slope was found, $35 < Re_\lambda < 80$. Thus there is some question of the validity of equation (12) even for these cases.

Figures 24 and 25 show the dissipation rate results for flows C and D. For comparison the dissipation rate for a turbulent boundary layer which possesses a logarithmic "law of the wall" mean velocity profile is given by

$$\frac{\varepsilon\nu}{U_\infty^4} = \left(\frac{C_f}{2} \right)^{3/2} \frac{1}{0.4\eta} \qquad (13)$$

This equation is derived from equation (11). This result would also be expected to be valid for moderately accelerated turbulent boundary layers since a logarithmic mean velocity profile would still exist. At the upstream stations the dimensionless dissipation $\varepsilon\nu/U_\infty^4$ is the same order of magnitude for each flow from equations (10),

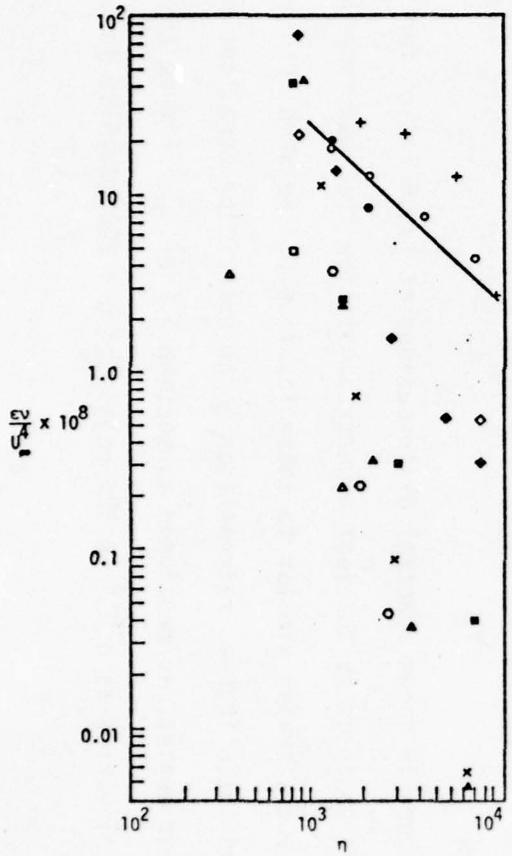

Figure 24. Dissipation results for flow C. Eqn. (12) results: + 106.9, ○ 137.2, ◇ 157.8, □ 170.8, △ 182.3. Eqn. (10) results: ● 137.2, ◆ 157.8, ■ 170.8, × 178.3, ▲ 182.3, ⬭ 185.8. Solid line - eqn. (13) with $C_f \times 10^3 = 2.2$.

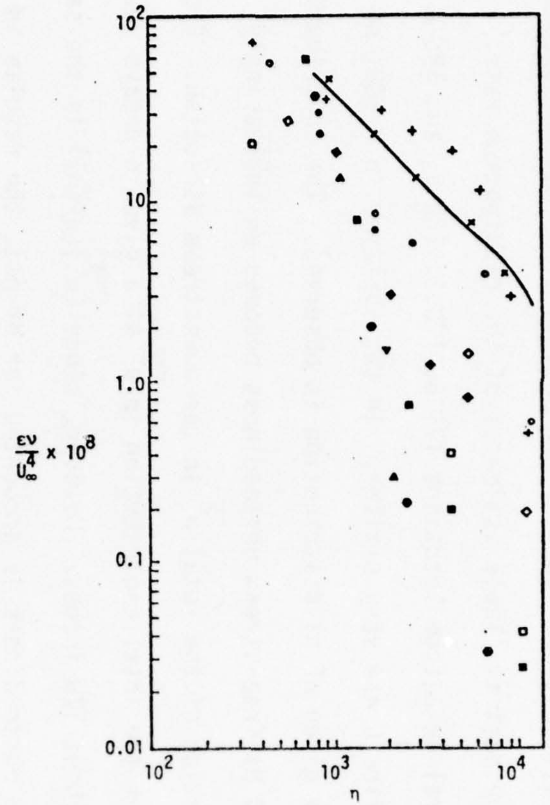

Figure 25. Dissipation results for flow D. Eqn. (12) results: + 101.2, X 112.2, 0 123.1, ◇ 132.2, □ 140.7. Eqn. (10) results: ● 123.1, ◆ 132.2, ■ 140.7, ⬢ 146.8, ▲ 153.6, ▼ 161.1. Solid line - eqn. (13) with $C_f/2 \times 10^3 = 2.9$.

(12), and (13). The results from equation (12) for each flow near the 100 inches location are closely the same. At 137.2 inches in flow C the results from equations (10) and (12) are reasonably close for a given η when $\alpha = 0.8$ is used. Since the nF(n) spectra at downstream stations are flat for $\eta > 800$, the results from equation (10) are the best available estimates of the dissipation rate.

Spectral data from locations 170.8, 178.3, 182.3, and 185.8 inches of flow C are very similar. In the sublayer, $\eta < 800$, no flat region of a given nF(n) distribution is observed. The contribution from the 20 Hz free-stream unsteadiness becomes an increasingly greater portion of the total $\overline{u^2}$ in the downstream direction. Figure 9 shows that the total contribution to $\overline{u^2}$ at a given η decays downstream of about 178 inches. However, since $(\overline{u^2})(nF(n))$ is the same whether the unsteadiness is accounted for or not, the results in figure 24 should be unaffected. For a given η in the outer region, $\epsilon\nu/U_\infty^4$ decreases two orders of magnitude from 137.2 inches to 170.8 inches. Thereafter the decrease is much slower. In the inner region, $\eta < 1000$, $\epsilon\nu/U_\infty^4$ remains about the same order of magnitude all along the flow.

Figure 19 shows spectral distributions at 135.6 inches for flow D. This location is the last downstream station that was recorded with spectra shapes similar to those for flow C. Between this location and 161.6 inches, retransition to an entraining turbulent boundary layer begins, as mentioned in section 3.7 below. Figure 20 shows that F(n) varies as $n^{-2.3}$ in the region of $\eta < 800$ at 161.6 inches, where the intermittency is about 0.01. In the outer region at this location flat nF(n) spectra are found. Note the relative importance of the 20 Hz unsteadiness. Downstream where the intermittency is progressively increasing, the spectral distributions are flatter. At 179.7 and 189.7 inches the peaks shift progressively toward 1 KHz as the low accelerated turbulent boundary layer redevelops. Notice that 20 Hz unsteadiness does not dominate the near wall spectra.

The dissipation results for flow D from equations (10) and (12) are in reasonably good agreement at 123.1 inches and in fair agreement at 132.2 and 140.7 inches. Between 132.2 and 161.1 inches the results from equation (10) are considered the best available estimates of the dissipation rate. For a given η in the outer region, $\varepsilon\nu/U_\infty^4$ decreases two orders of magnitude from 123.1 to 161.1 inches, as was observed for flow C. As for flow C, $\varepsilon\nu/U_\infty^4$ remains about the same order of magnitude in the inner region along this length of flow. Certainly the spectral behavior downstream of retransition needs further research.

3.6 Wall bursting frequencies and spanwise structure

The more or less periodic lift off or bursting process in the viscous sublayer has become accepted as the sequence of events that create the Reynolds shearing stress near the wall (Wallace et al., 1972; Nychas et al., 1973; Willmarth, 1975). On a short-time basis the velocity fluctuations in the sublayer produced by the bursting process vary across the sublayer in the spanwise direction. The data of Gupta et al. (1971) indicate that the short-record-time normalized cross-correlation of fluctuations $s\hat{R}_{uu}(z, Ts)$ could be represented by a spanwise periodic function. Their results indicate that the short-record-time T_s over which the cross-correlation is averaged must be less than about 20 bursting periods in order for the periodic spanwise structure to be detectable. Simpson and Wallace (1975) measured the average frequency of bursting and the long-time spanwise cross-correlation of fluctuations for two sink-flow type strongly accelerated turbulent boundary layers, flows A and B. Here the results from flows C and D are presented.

Strickland and Simpson (1973, 1975) assumed that the short-time autocorrelation time scale from a flush wall hot-film sensor and the bursting period were equal. Histograms of the frequency characterized by the time to the first peak on these autocorrelations were constructed and the corresponding frequency of the peak of each histogram was taken as the characteristic frequency. The histograms appeared to have a log-normal probability distribution, so this peak frequency was also the median frequency. They also proved a one to one correspondence between this characteristic frequency and the peak of the first moment of the wall shearing stress spectra nF(n). Also, examination of spectral data from zero pressure gradient boundary layers produced bursting frequencies in agreement with those previously reported. More recently, Simpson (1976) used a pattern recognition algorithm to determine the average bursting frequency from flush surface hot-film signals produced in the Max-Planck-Institut für Strömungsforschung oil channel. This average bursting frequency closely agreed with the peak of the nF(n) spectral distribution of these signals.

As was done for flows A and B, the peak of each nF(n) curve for flows C and D was deduced as the bursting frequency for a given wall spectral distribution. The results are given in table 3. As it is clear from figures 26 and 27, it is difficult to select a precise single frequency at which nF(n) is a maximum for a given distribution. Consequently, a range over which the peak frequency definitely occurs is also presented in table 3.

Two types of non-dimensionalizing parameters have been used in previous bursting frequency studies, inner variables and outer variables. Inner variables are the shear velocity U_τ for the velocity scale and ν/U_τ for the length scale. This scaling does not correlate other available bursting data. The bulk of available bursting frequency results for turbulent boundary layers correlate using the outer flow velocity and length scales, U_∞ and δ. For zero pressure gradient boundary layers $U_\infty/\delta n_b$ is about 5 (Rao et al., 1971) and varies between 11.7 and 8.35 for the separating turbulent boundary layer of Simpson et al. (1974). It should be noted that this large eddy outer variables scaling continued even after the boundary layer separated.

For flow A presented by Simpson and Wallace (1975), $U_\infty/\delta n_b$ started at about 5 at 89.2 inches, decreased to about 3.5 at about 139 inches or the location of minimum H, and then monotonically increased to a value above 50 at the last measurement station. The

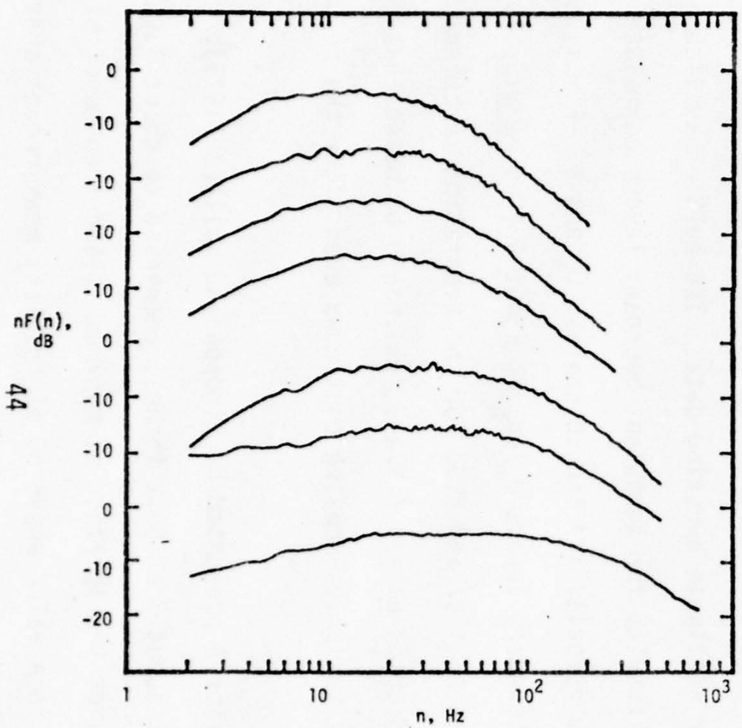

Figure 26. Typical flush-wall hot-film spectra, flow C. Station location from top to bottom: 105.0, 122.0, 135.5, 156.3, 171.8, 184.2, and 186.2. Record times 100 sec. Note displaced ordinate scale.

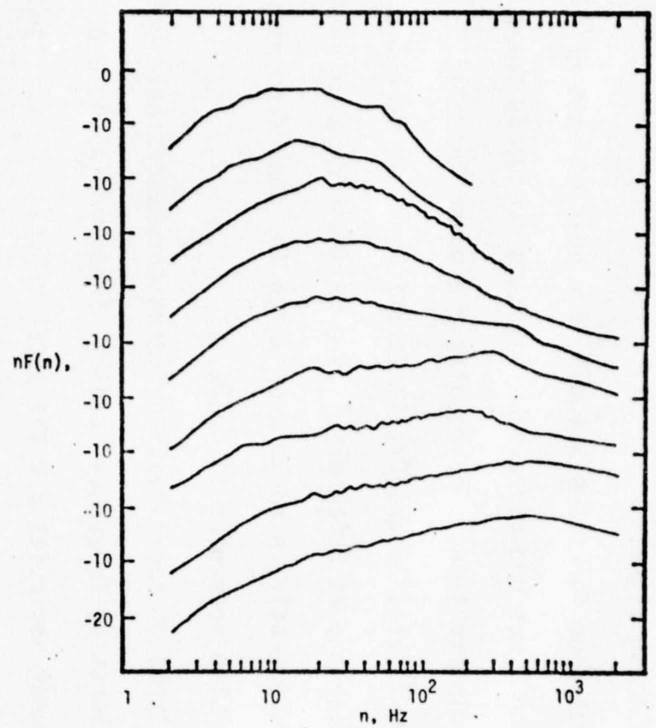

Figure 27. Typical flush-wall hot-film spectra, flow D. Station location from top to bottom: 122.0, 135.5, 158.3, 171.8, 175.2, 177.4, 182.0, 184.2, and 186.2. Record times 50 sec. Note displaced ordinate scale.

bursting frequency n_b apparently reached about a constant value after the asymptotic condition was achieved, so an increasing $U_\infty/\delta n_b$ reflects the fact that U_∞ increases and δ decreases faster than n_b increases. For flow B $U_\infty/\delta n_b$ remained nearly constant at about 3(±1) until the location of a minimum in H, downstream of which it also increased monotonically to a value of about 90 at the last measurement station. The bursting frequency n_b was virtually constant all along flow B. The outer variables parameter $U_\infty/\delta^* n_b$ was no better a correlation parameter for these data.

The results for flow C indicate that the bursting frequency increased up to about 165.3 inches or where H was about a minimum and where entrainment ceased. The plateau on the nF(n) spectral distributions existed over an increasingly wider frequency range at downstream locations. The low frequency end of the plateau remained at about 25 Hz. The results from these three flows indicate that they are non-equilibrium flows at least up until the cessation of entrainment. Thus no equilibrium non-dimensional parameter such as $U_\infty/\delta n_b$ should have a constant value upstream of the minimum in H. Downstream of the minimum H location there was no entrainment, so the large eddy structure and the intermittent turbulent/non-turbulent outer region flow were not creating new bulges. Thus the bursting frequency and the frequency of passage of the intermittent bulges (see section 3.7 below) were constant in this downstream region.

For flow D the bursting frequency increased until near the location where H was a minimum, after which it remained constant until

Flow C			Flow D		
Station (inches)	Peak frequency, n_b, Hz	Range of peak, Hz	Station (inches)	Peak frequency, n_b, Hz	Range of peak, Hz
90.2	15	13-18	105.0	12	10-15
105.0	12	10-15	110.4	15	10-20
110.4	13	10-20	122.0	15	10-20
117.3	15	10-20	129.9	19	15-25
122.0	16	13-20	133.5	18	15-25
129.9	16	11-20	135.5	18	15-20
131.6	16	11-20	139.7	20	15-25
135.5	20	14-22	147.6	20	15-25
138.6	16	10-20	158.3	25	20-30
139.7	16	10-20	171.8	20	15-30
147.6	20	15-30	175.2	25	20-40
156.3	20	15-20	177.4	300	250-350
158.3	20	15-25	182.0	200	150-250
165.3	25	20-30	184.2	500	400-700
171.8	25	20-30	186.2	500	400-700
175.2	25	15-35	189.6	500	400-700
177.4	26	20-30			
182.0	26	20-30			
184.2	--	20-45			
186.2	--	20-100			

Table 3. Peak frequencies of nF(n) spectral distributions from flush surface hot-film sensors.

Station (inches)	Z_{max}, mm	λ^+_{Z1}	Z_{min}, mm	λ^+_{Z2}	L_Z, mm	L^+_Z	$\frac{1}{2t_{min-max}}$, Hz
117.3	7.62	6.7	5.59	99	4.88	43.4	19
138.6	---	---	7.11	151	4.46	47.3	16
156.3	10.16	135	5.33	142	3.23	43.0	--
165.3	9.40	157	3.56	119	1.42	23.8	--
182.0	8.38	302	3.86	278	1.79	64.5	28
126.3	14.48	179	5.33	132	2.70	33.3	22
138.6	9.40	160	4.83	164	2.60	44.3	21
156.3	8.38	274	2.41	158	1.11	36.4	22
165.3	7.87	332	3.30	279	3.61	152.5	--
182.0	---	---	21.6	3480	12.50	1007	--

Table 4. Experimental results from the wall spanwise spatial cross-correlatives. First five entries, flow C; second five, flow D.

the beginning of retransition to a low accelerated turbulent boundary layer. As discussed in section 3.7 below, high velocity pulses are first detected at about 165.3 inches. Figure 27 shows that the wall sensor spectra are not appreciably affected until about 175.2 inches.

Figure 28(c) shows a typical signal trace for this location. Between 175.2 and 182.0 inches, a distinct local peak is observed in the spectra at frequencies an order of magnitude higher than observed upstream. This indicates that the high frequency oscillations that are contained in the higher velocity pulses are increasingly important. Downstream of 184.2 inches the laminar-like low velocity regions such as seen in figure 31 for 182.0 inches were no longer observed on signal traces. Thus the flow at the wall was always turbulent. Peak frequencies are observed in figure 27 to occur at an even higher frequency of about 500 Hz.

Several researchers have proposed that during the bursting process a hairpin or horseshoe vortex with trailing legs is formed (Willmarth, 1975). With this model, the counter-rotating trailing legs would produce fluctuations in the sublayer that are periodic in the spanwise or z direction on a short-time basis. Simpson (1976) noted that this model suggests motions too coherent to be consistent with experimental observations.

He alternatively proposed that "fingers" of high velocity fluid come from the outer region at a velocity much higher than sublayer mean velocities toward the wall and displace the low velocity fluid

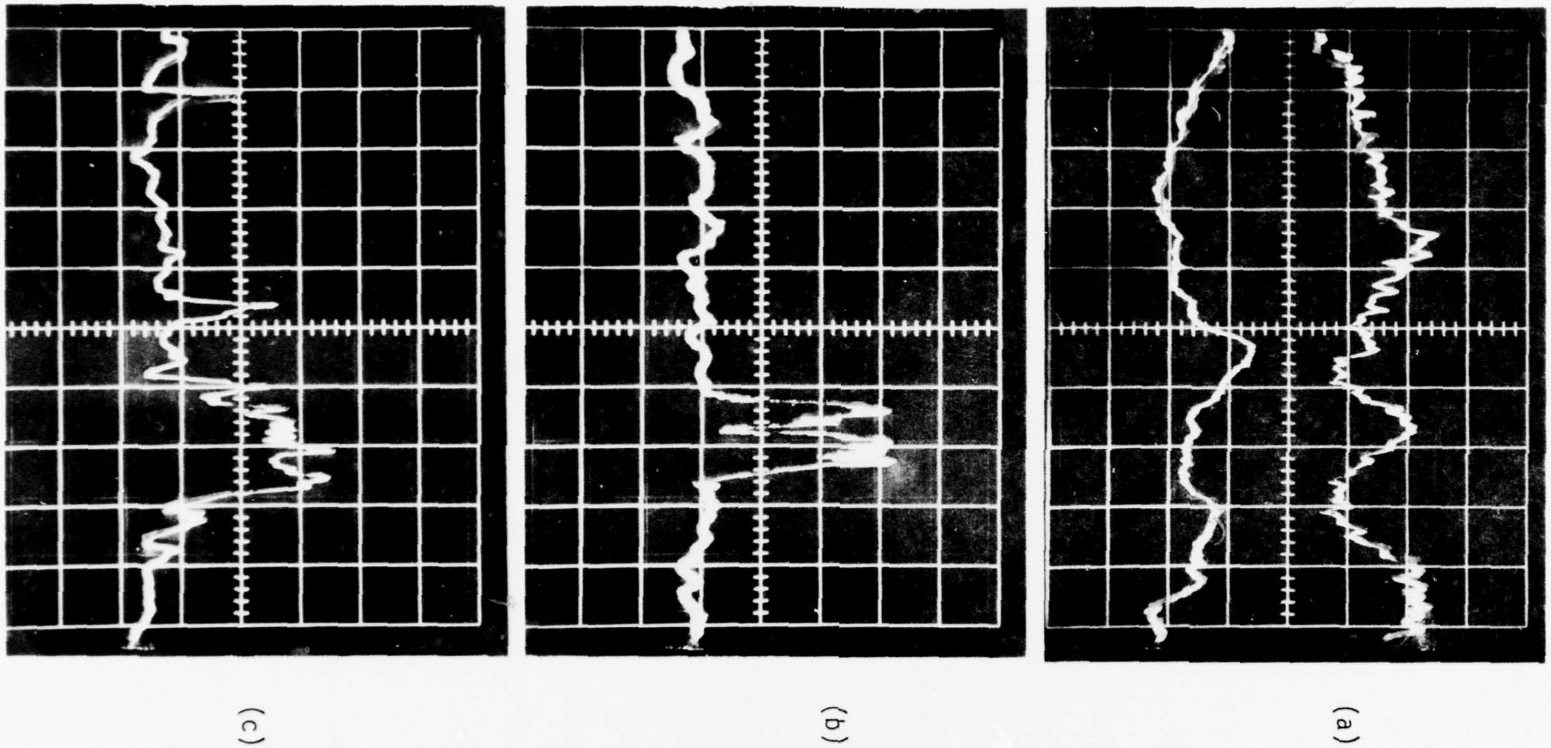

Figure 28. Flush surface hot-film signals for flow D. Top photo: 138.6 inches, $\Delta Z = 4.83$ mm; top trace-movable sensor, 500 Hz low pass filtered, lower trace-fixed sensor, 1 kHz low pass filtered; 10 msec/div. Middle photo: 171.5 inches, 20 msec/div. Bottom photo: 175.0 inches, 5 msec/div.

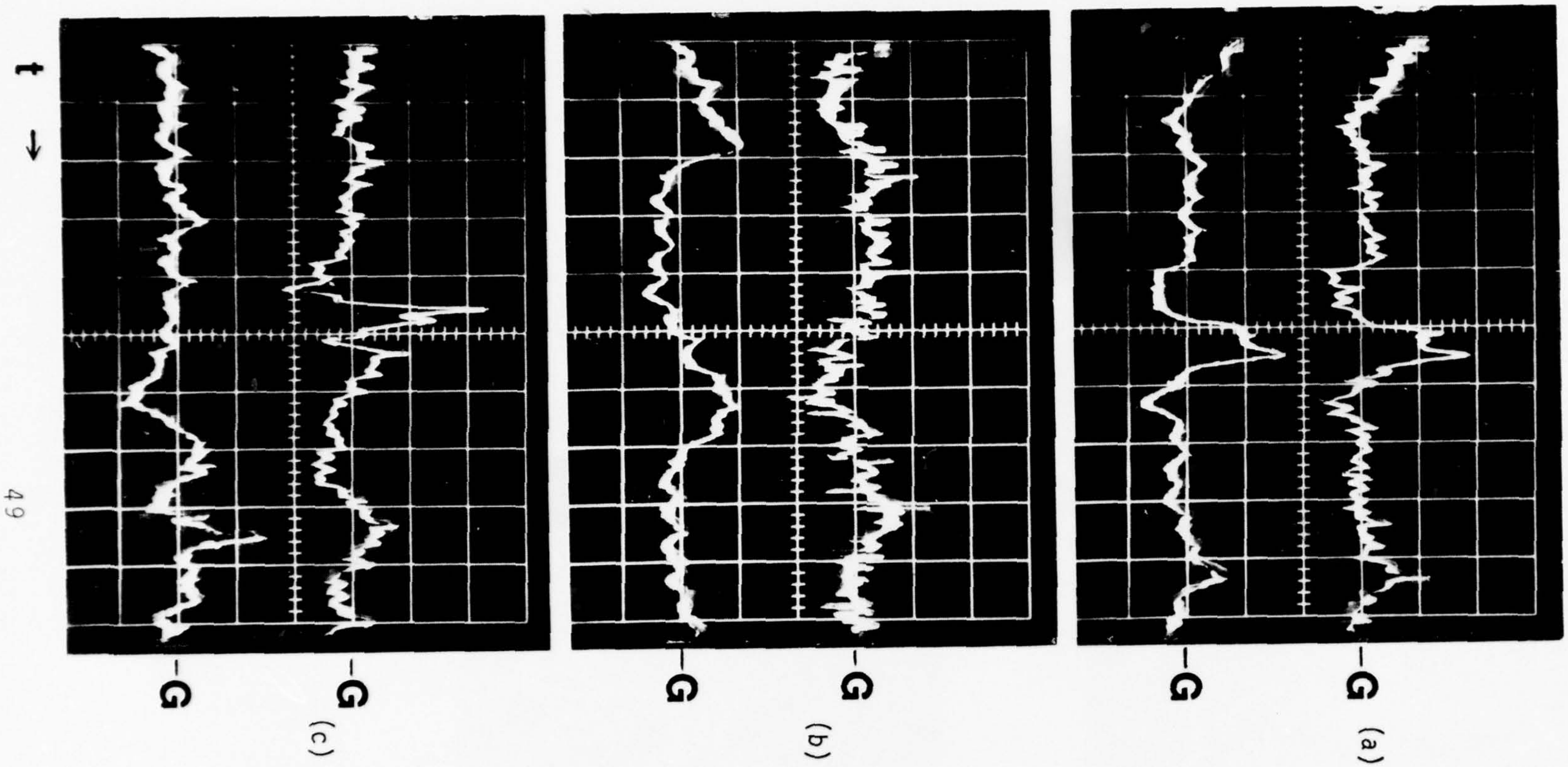

Figure 29. Flush surface hot-film signals from two-sensor unit at 156.3 inches for flow D. Top trace of each photo - moveable sensor; bottom trace - fixed sensor. From top to bottom Z = 0 mm, 2.29 mm, and 8.38 mm. Abscissa - 10 msec/div. Low pass filter: 500 Hz moveable sensor; 2 kHz - fixed sensor. G denotes mean signal level.

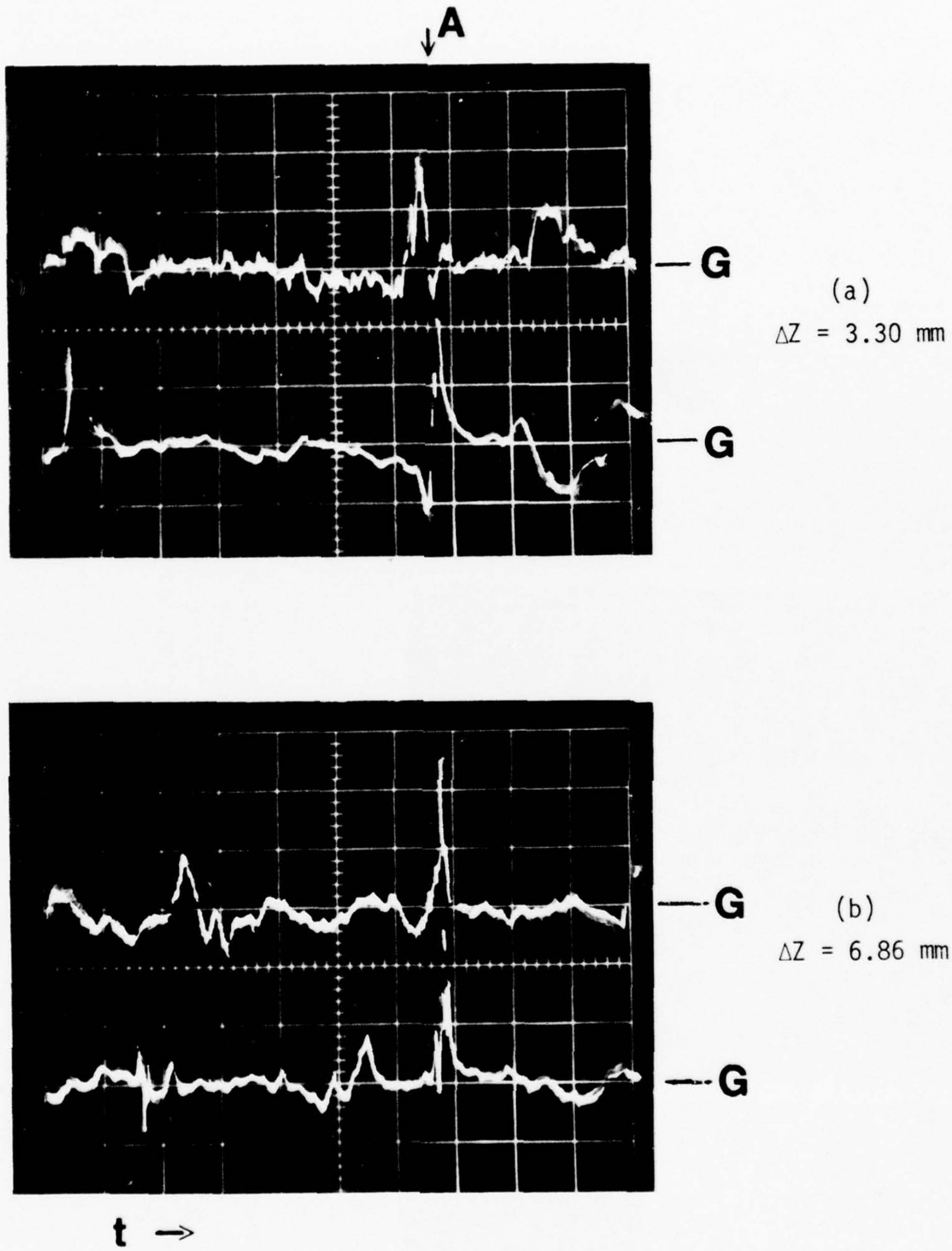

Figure 30. Flush surface hot-film signals from two-sensor unit at 165.3 inches for flow D. Top trace of each photo - moveable sensor; bottom trace - fixed sensor. Abscissa - 10 msec/div. low pass filtered at 2 kHz. G denotes mean signal level.

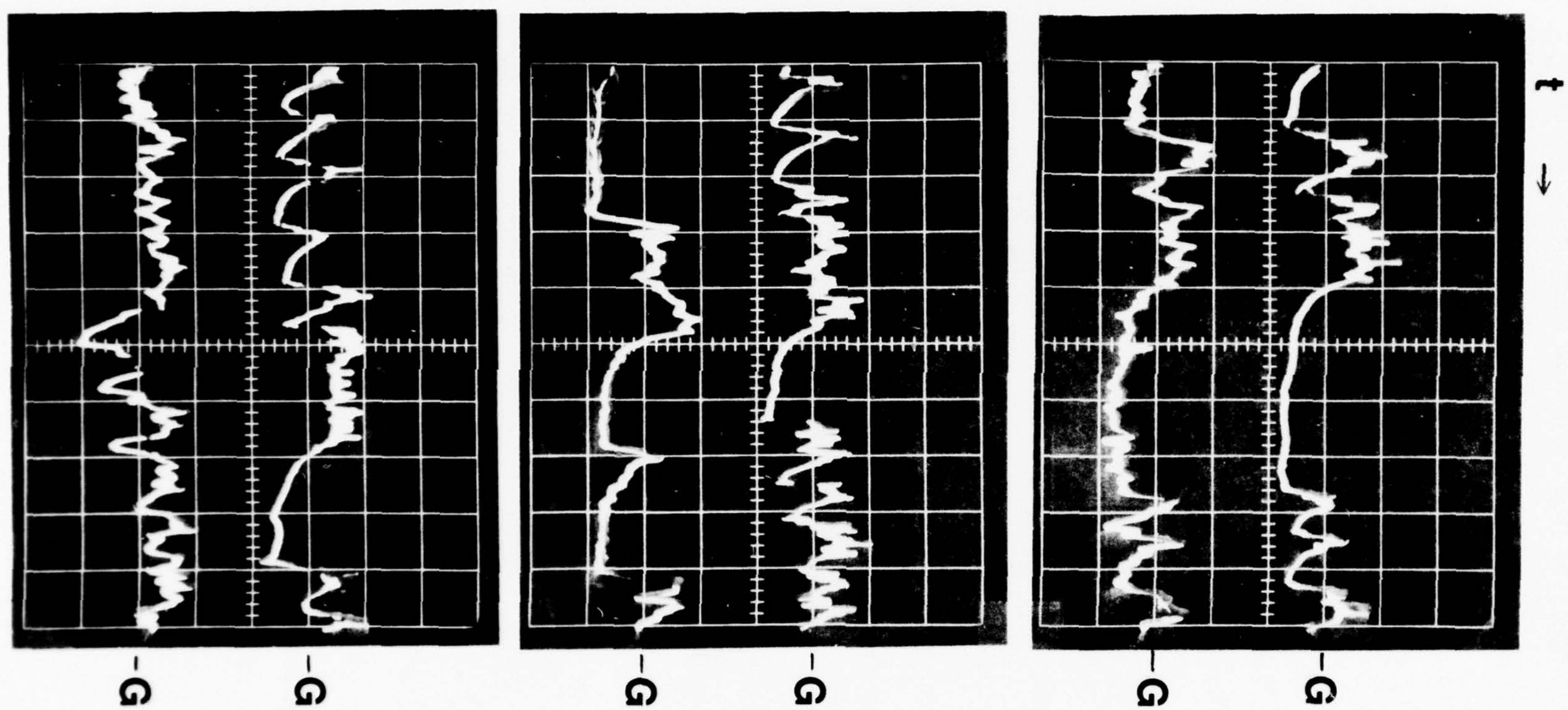

Figure 31. Flush surface hot-film signals from two-sensor unit at 182.0 inches for flow D. Top trace of each photo - fixed sensor; bottom trace - moveable sensor. From top to bottom ΔZ = 0 mm, 8.13 mm, and 19.56 mm. Abscissa - 5 msec/div. Low pass filter: 1 kHz - moveable sensor; 5 kHz - fixed sensor. G denotes mean signal level.

to each side. These fingers of high velocity fluid were found for the MPI oil channel flow to be no less than $\Delta z^+ \simeq 11$ nor greater than about $\Delta z^+ \simeq 44$ in size and are spaced spanwise across the flow at average distances of about $\lambda_z^+ \simeq 100$. There are curved fronts on these higher velocity fluid fingers so that the low velocity fluid just downstream at that instant must move aside to satisfy continuity requirements. Thus low velocity fluid trapped between two high velocity fluid fingers must move outward from the wall.

After the low velocity fluid has been "ejected" away from the wall, the two adjacent higher velocity fluid fingers coalesce. Since this fluid now occupies the wall region it progressively gives up its momentum until new high velocity fingers from the outer region force this fluid away from the wall and the process is repeated downstream. The spanwise locations of these high velocity fingers vary randomly for successive burst occurrences.

An interesting point is that these high velocity fingers must be formed so that the low velocity fluid can be ejected between them. Otherwise a blanket of higher velocity fluid would trap the low velocity fluid beneath. Stability considerations then require regions of high velocity fluid separated by low velocity ejections. The bulk of available experimental results for low pressure gradient flows show that the most preferred spacing of these higher velocity regions is $\lambda_z^+ \simeq 100$. It appears unlikely that streamwise vortices that rotate more than one revolution are produced by the ejection process.

Some characteristics of the spanwise sublayer spatial structure for flows C and D were determined using the two sensor wall unit described by Simpson and Wallace (1975). The unit was located spanwise across the tunnel with the direction of travel of the slider plate perpendicular to the streamwise flow direction. The signals from the two sensors were time-delay cross-correlated using the SAICOR model 41 correlator, with the record time for a given z-spacing time-delayed correlation being 65.5 seconds. For zero time delay, normalized spanwise cross-correlations $s\hat{R}_{\tau\tau}(z)$ such as shown in figures 32 and 34 result. Three characteristic lengths were deduced, the distance to the first correlation maximum z_{max}, the distance to the first correlation minimum z_{min}, and the integral length scale

$$L_z = 2\int_0^{z_i} s\hat{R}(z)dz \qquad (14)$$

The limit of integration z_i was taken as the largest available location for which data were available.

Figure 32 and table 4 indicate that for flow C the integral length scale progressively decreased until 165.3 inches and slightly increased thereafter. The parameters z_{min} and z_{max} are relatively easy to interpret, within 10% for the former and 20% for the latter. The results of Gupta et al.(1971) and Simpson (1975) indicate that z_{min} is a somewhat more reliable spatial parameter than z_{max}. These two parameters are normalized by the wall length scale ν/U_τ to produce the quantities

$$\lambda^+_{z1} = \frac{U_\tau z_{max}}{\nu} \quad \text{and} \quad \lambda^+_{z2} = \frac{2U_\tau z_{min}}{\nu} \qquad (15)$$

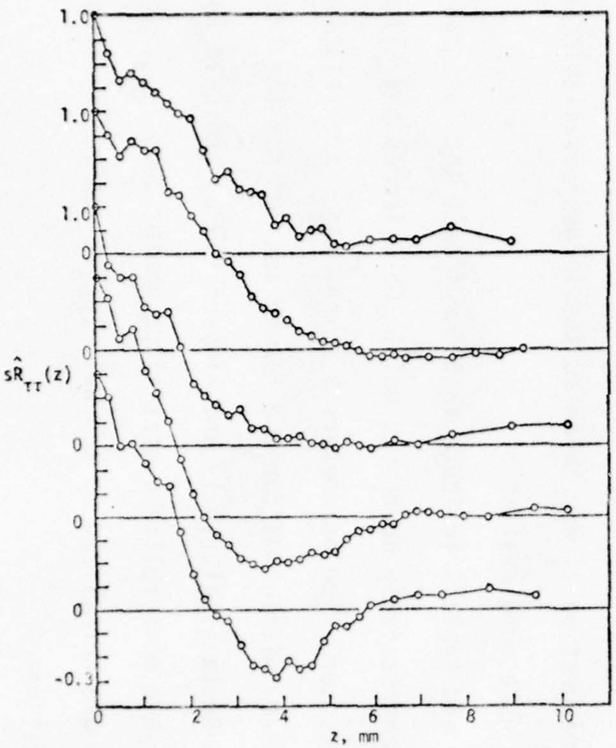

Figure 32. Normalized long time-averaged spanwise correlation $s\hat{R}_{\tau\tau}(z)$ results at the wall for flow C. Station locations from top to bottom: 117.3, 138.6, 156.3, 165.3, and 182.0 inches. Note displaced ordinate scales.

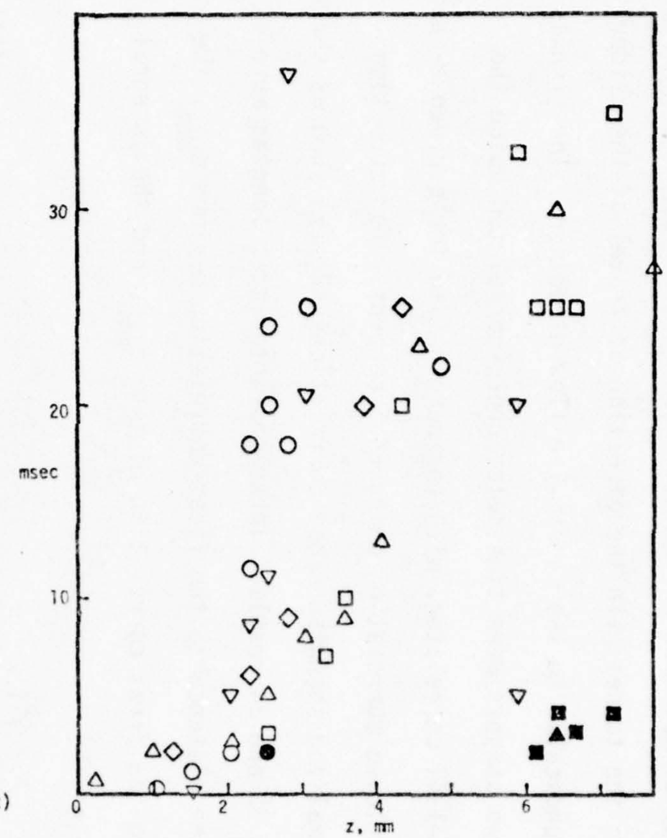

Figure 33. Observed minima and maxima from $\hat{R}_{\tau\tau}(z,t)$ data, flow C. Open symbols - maxima; solid symbols - minima: △, 117.3; □, 138.6; ◇, 156.3; O, 165.3; ▽, 182.0.

which have the value of about 100 for zero pressure gradient boundary layers. Only at 182.0 inches does λ^+_{z2} increase appreciably from this value. At the two downstream locations, $s\hat{R}_{\tau\tau}(z)$ behaves more like the low Reynolds number cross-correlation computed by Simpson (1976). He used the Gupta el al. spanwise spacing probability distribution to compute $s\hat{R}_{\tau\tau}(z)$ when no large eddy outer region structures were present, i.e. $L_z/z_{min} \to 0$.

Figure 34 and table 4 indicate the same type of behavior for flow D up to 156.3 inches with $L_z/z_{min} \simeq 1/2$. Figures 28(a) and 29 shows typical simultaneous signal traces for the two sensors. For the two downstream stations, the signals contained high velocity pulses intermittently as shown in figures 30 and 31 and as discussed in section 3.7 below. The length scale ratio L_z/z_{min} was about 1.1 at 165.3 inches and 0.579 at 182 inches. The parameter λ^+_{z2} is significantly larger than 100 at these two stations.

Several different models were examined in an attempt to correlate these λ^+_{z2} results. As attempted for flows A and B, λ^+_{z2} was compared with the data of Schraub and Kline(1965) when presented versus K. Just as Schraub and Kline found, λ^+_{z2} is of the order of 300 for $K \approx 3 \times 10^{-6}$. However, for lower K values λ^+_{z2} varied rather randomly between 100 to 164. In flow D λ^+_{z2} remained only at about 158 at 156.3 inches even after the flow had been subjected to a K of 3.85×10^{-6} and K was decreasing. After retransition to a low accelerated turbulent boundary layer had begun λ^+_{z2} was very large even though K was of the order of 10^{-6}. It does not appear that λ^+_{z2}

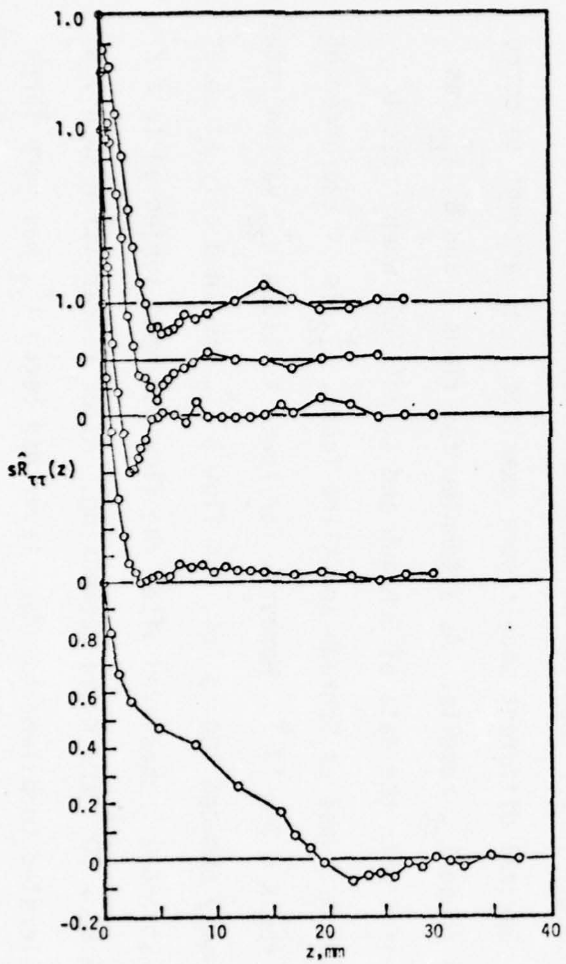

Figure 34. Normalized long time-averaged spanwise correlation $s\hat{R}_{\tau\tau}(z)$ results at the wall for flow D. Station locations from top to bottom: 126.3, 138.6, 156.3, 165.3, and 182.0 inches. Note displaced ordinate scales.

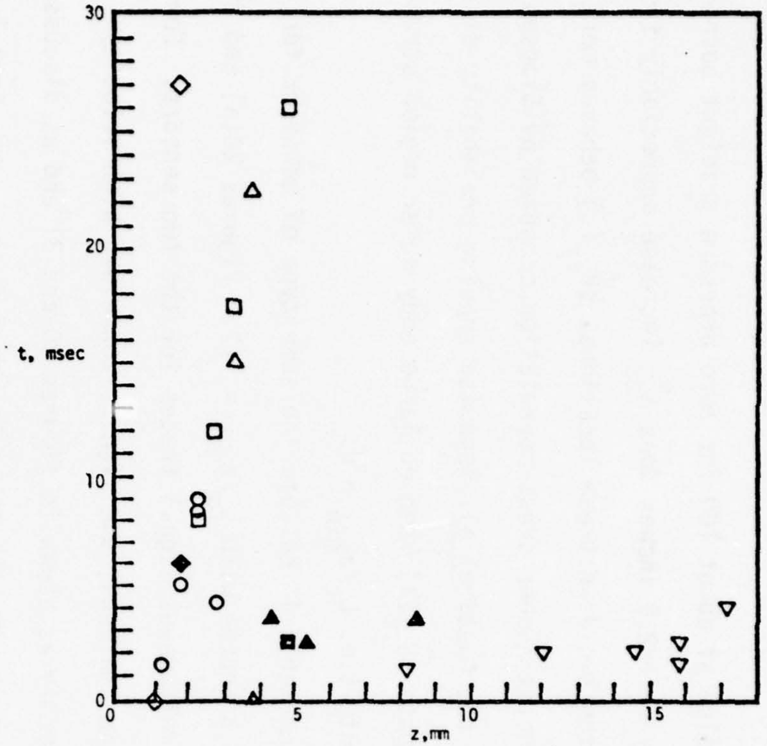

Figure 35. Observed minima and maxima for $s\hat{R}_{\tau\tau}(z, t)$. Maxima: △ 126.3, □ 138.6, ◇ 156.3, ○ 165.3, ▽ 182.0; Minima: ▲ 126.3, ■ 138.6, ◆ 156.3

is solely a function of K. After retransition began, the flow character with high velocity pulses is entirely different than that found upstream.

Simpson et al. (1974) found that for adverse pressure gradient turbulent boundary layers, the maximum turbulent shearing stress should be used in the velocity scale in order to produce $(-\overline{uv}_{max})^{1/2} z_{max}/\nu$ values of about 100. This model was not successful for flows A and B (Simpson and Wallace). Unfortunately the split-film results for $-\overline{uv}$ presented in section 3.4 are not reliable in the wall region where it is a maximum. Since $-\overline{uv}/U_\infty^2$ decreases along a strongly accelerated flow, $(-\overline{uv}_{max})^{1/2} z_{max}/\nu$ would also decrease. This parameter would fall well below 100 since $(-\overline{uv}_{max})/\tau_w$ would be below 1/4 at say, 156.3 inches. Another correlation parameter, $(KU_\infty^2/\nu n_b)(C_f/2)^{-1/2}$, used by Simpson et al. was also not successful in correlating these data.

It appears that the λ_z^+ spacing lags behind local conditions. In other words, the spatial parameters z_{max} and z_{min} remain large due to upstream conditions in these non-equilibrium flows. For example, at 182.0 inches in flow C, U_τ/ν is more than twice that at 165.3 inches but z_{min} and z_{max} are only slightly different. In retrospect, there is no reason to expect flows C and D to possess equilibrium characteristics.

Figures 33 and 35 show the local maxima and minima from the time-delayed cross-correlations for a given z spacing which were clearly distinguishable from noise. The wavelike nature of the viscous sublayer behavior is illustrated by the fact that the maximum correlation at a given z spacing is time-delayed. The bursting frequency results given in table 3 above are somewhat crudely supported by the frequency corresponding to twice the time delay between the first minima and the first maxima, as given in table 4. In other words, if there is a repetitive wave-like nature of the sublayer flow in both z and t, the time-averaged characteristic bursting frequency should be approximately the same at all z sensor spacings.

For flow D figures 29(b) and 30(a) show that for the z spacings of sensors at which the spanwise cross-correlations were a minimum, the two signals were strongly out of phase. At time A in the latter oscilloscope photograph a short period of high velocity fluid passed over the moveable sensor. At the same time lower velocity fluid passed over the fixed sensor. A short time later, of the order of 3 msec, high velocity fluid passed over the fixed sensor while low velocity fluid passed over the moveable sensor. About 15 msec later the two traces again appear to be strongly out of phase. These data are consistent with the observations of Simpson (1976) regarding fingers of high velocity fluid as mentioned above.

3.7 Intermittency measurements

The intermittency factor γ, or the fraction of time that the flow is turbulent at a given spatial location, was determined for flow C using smoke in the boundary layer as the marker of turbulent fluid and scattered light from this smoke at a given location as the detected signal, using the optical apparatus described in section 2 above. Due to the large-scale mixing in the turbulent region the smoke is rapidly diffused while smoke is carried across the turbulent/non-turbulent interface by the much slower process of molecular diffusion. Thus, the smoke was assumed to be effectively confined to the turbulent regions of the flow. Fiedler and Head (1966) verified that values obtained by this method agree with those obtained by analysis of hot-wire signals.

The signal passed from the photomultiplier tube through a trigger circuit which produced positive rectangular pulses when the input was above a preset discrimination level. The discrimination level was set at approximately 10% of the peak PM tube sign amplitude. The counter-timer determined the fraction of time the positive pulses were present, which is the intermittency. Due to the steep slope of the PM output pulses, γ was not very sensitive to slightly different discriminator levels. Preliminary data taken in a zero pressure gradient flow were found to be in close agreement with the data of Klebanoff (1954).

The intermittency factor γ of this turbulent/non-turbulent interface has been previously found to be well represented by the integral of the normal distribution curve

$$\gamma = \frac{1}{\sqrt{2\pi}\,\sigma} \int_{\xi}^{\infty} \exp\left(-\frac{1\xi^2}{2\sigma^2}\right) d\xi \qquad (16)$$

where $\xi = y - \overline{Y}$, $\overline{Y}$ is the mean distance from the wall to the interface where $\gamma = 0.5$, and σ is the deviation from the mean. If this interface is viewed as a wavy pattern moving approximately at the free-stream velocity, then σ characterizes the amplitude of this pattern. γ was in good agreement with equation (16) for flow C. Table 5 presents the characterizing parameters which describe these intermittency distributions.

The results of Fiedler and Head (1966) showed that the parameters $\overline{Y}/\delta^*$ and σ/δ^* are strongly dependent on the shape factor H for values of H less than about 2. This dependence is quite strong as the lower limiting value of H is approached. The minimum H found for flow C was about 1.26 at about 165 inches. Upstream of the minimum in H for flow C,at 130.6 and 149.3 inches, values of these parameters were well within the scatter of the Fiedler and Head results for their "normally developing" boundary layers. As pointed out in section 3.2 above, no entrainment of non-turbulent fluid takes place after the minimum H value occurs so it is not unexpected that $\overline{Y}/\delta^*$ and σ/δ^* downstream do not follow the results of Fiedler and Head.

The celerity and mean velocity profile measurements for flows A and B reveal that when there is no entrainment, the entire intermittent region is moving with the free-stream velocity. This means that there cannot be any relative streamwise motion of the intermittent region nor any engulfment of non-turbulent fluid by turbulent bulges. $U_\infty(\overline{Y} - \delta^*)$ and $U_\infty\sigma$ remain approximately constant downstream. As for flows A and B, the intermittent region plays no role in the momentum transport after entrainment.

Measurements of the frequency with which turbulent bulges pass a fixed point were made by counting the number of pulses per unit

Station (inches)	$\overline{Y}$, inches	σ, inches	$n_Y \times 10^{-4}$	$\frac{\sigma U_\infty}{\nu} \times 10^{-3}$	n_{i_Y}, Hz
130.6	3.00	0.491	1.506	2.465	47.7
149.3	2.55	0.417	1.540	2.518	45.4
164.2	1.93	0.440	1.605	3.660	50.2
170.8	1.59	0.437	1.620	4.453	53.0
178.3	1.19	0.306	1.759	4.523	54.8
185.8	0.704	0.193	1.562	4.281	58.7

Table 5. Intermittency parameters for flow C.

Station, inches	γ
165.3	0.02
171.8	0.15
175.2	0.55
177.4	0.78
182.0	0.96
184.2	1.0
186.2	1.0

Table 6. Surface intermittency parameters for flow D.

time from the schmitt trigger output. A serious problem with this method arises due to the fact that several short duration pulses may occur as the probe volume enters and leaves the turbulent bulge thus giving rise to frequencies which are perhaps an order of magnitude higher than the actual.

In order to reduce the effects of this problem, the signal from the schmitt trigger was processed through a low pass filter which attenuated the short duration pulses responsible for the higher frequency. It was found that the resulting frequency obtained was quite dependent on the filter setting, so the filter setting was obtained by visual comparison of the unfiltered PM tube signal with the filtered schmitt trigger signal on a dual trace storage oscilloscope. Typical signal and oscilloscope traces from this method are given by Strickland and Simpson (1973). The filter was set such that there was a single zero crossing from negative to positive for each "significant" peak on the unfiltered PM tube signal. The filter setting chosen for all the results here was 300 Hz.

Figure 33 of Simpson and Wallace (1975) shows a typical bell-shaped frequency distribution such as obtained for flow C. The frequency distributions across the intermittent region for flow C are rather similar when the frequency is normalized on the frequency at $\overline{Y}$, n_{i_γ}. As for flows A and B, the peak frequency for each profile occurred at about the location where $\gamma = 0.6$. The n_{i_γ} for flow C was about twice the bursting frequency n_b when tables 3 and 5 are compared. Since the technique used to obtain the intermittency frequency requires a certain amount of arbitrary judgment, as do techniques using hot-wires, it cannot be determined if the absolute values of these measurements are accurate. However, since for each flow n_b was proportional to n_{i_γ}, it appears that the large motion influencing the intermittency also influences the wall bursting frequency even downstream of the cessation of entrainment. Strickland and Simpson (1973) also found n_b to be proportional to n_{i_γ} for an adverse pressure gradient turbulent boundary layer. Thus, apparently this proportionality is present in turbulent boundary layers over a wide range of pressure gradient conditions.

For flow D the intermittency at the surface was determined for the retransition region downstream from the flush-surface hot-film signals. The taped signals were examined for high frequency content since considerable mixing and high frequency oscillations are associated with turbulent fluid. These signals were passed through the model 330B filter with a 200 Hz-2KHz bandpass and then through the multiplier used as a squarer in order to rectify the negative portions. This signal was low-pass filtered at 300 Hz using the model 3202 filter and passed through a schmitt trigger. The resultant pulses were visually compared with the original signals on a storage oscilloscope for validity as regions of high frequency content. These pulse periods were accumulatively counted for 50 sec. by the digital timer-counter. The fraction of time pulses were present was the intermittency γ. These results are presented in table 6. These same signals were processed by using the schmitt trigger on the output signal of the model 330B filter. The resulting fraction of time positive pulses were present was doubled to get the intermittency since contributions from negative pulses had not been rectified. These latter results were within 5% of the results of table 6.

The results in table 6 follow a curve of the form of the integral of the normal distribution curve. γ increases slowly from about 165.3 inches to 171.8 inches, increases more rapidly up to 177.4 inches, and thereafter increases slowly to unity at about 184.2 inches. Upstream of 165.3 inches the flow had low frequency oscillations as shown in figures 28(a) and 29. It is clear in figures 30 that higher amplitude pulses were occasionally present at 165.3 inches. Figures 28(b) and (c) show the relatively high frequency oscillations in the high velocity pulses at 171.5 and 175.0 inches. The clearest oscilloscope traces are shown in figures 31 for 182.0 inches. The higher velocity regions contain high frequency oscillations. Regions of laminar-like flow follow each high velocity pulse. These velocity signals slowly decay, not because of limited sensor response but because of temporarily high velocity laminar flow that follows the turbulent pulses.

It is clear that in the low velocity wall regions downstream of the cessation of entrainment in flow D, the flow became progressively more laminar-like. The magnitude of the oscillations in these regions progressively decreased. However, beginning at 165.3 inches, high velocity fluid moved in toward the wall. The average frequency of occurrence of high velocity pulses in this downstream region was about 25 Hz, as determined by counting these pulses. Further analysis of these data is planned.

4. DISCUSSION

Many aspects of flows C and D are similar to previous results reported by other investigators and by Simpson and Wallace (1975). In flow D and in the flow of Blackwelder and Kovasznay (1972), K increased to a value which exceeded 3.8×10^{-6} and decreased downstream to zero. In both flows, a local maximum in $C_f/2$ occurred at the same streamwise position as the K maximum; the minimum in $C_f/2$ occurred downstream of the minimum of the intermittency at the wall; the maximum H occurred upstream of the $C_f/2$ minimum and approximately at the minimum intermittency at the wall.

In all four flows measured in this research program, the behavior of the turbulent boundary layer after the beginning of strong acceleration was very similar. An initially normal low-pressure-gradient boundary layer first became distorted. The wake-like tail of the mean velocity profile became progressively weaker until at the cessation of entrainment none remained. It appears that the shape factor H is about a minimum at this location. The bursting frequency and intermittent bulge passage frequency downstream either increased or remained about constant along this length. The surface spanwise structure was not appreciably different from a low Reynolds number low-pressure-gradient boundary layer. Downstream the entire intermittent turbulent/non-turbulent interface was outside the boundary layer thickness δ and the celerity of this region was the free-stream velocity.

Simpson and Wallace (1975) showed that normal stresses production was important in the mean turbulence kinetic energy balance

$$\frac{1}{2}\left\{U\frac{\partial\overline{q^2}}{\partial x}+V\frac{\partial\overline{q^2}}{\partial y}\right\}+\frac{\partial}{\partial y}\left[\frac{\overline{pv}}{\rho}+\frac{1}{2}\overline{q^2v}\right]+\varepsilon=-\overline{uv}\frac{\partial U}{\partial y}-(\overline{u^2}-\overline{v^2})\frac{\partial U}{\partial x} \quad (17)$$

Here the terms are from left to right: advection, turbulent diffusion, dissipation, shear production, and normal stresses production. This last term is of opposite sign to the shear production term in strongly accelerated flows. The net turbulence energy production is less than the shear production by the factor

$$F = 1 - \frac{(\overline{u^2} - \overline{v^2})\partial U/\partial x}{(-\overline{uv})\partial U/\partial y} \quad (18)$$

which represents total production to shear production.

They also found that the normal stresses term reduces the diffusion of turbulence kinetic energy into the freestream, or the entrainment of non-turbulent fluid into the boundary layer. The velocity difference between turbulent fluid in the intermittent region and the irrotational freestream fluid approaches zero with strong acceleration. Thus, velocity profile instabilities which produce the eruption and eventual engulfment of free-stream fluid are eliminated. There could be no creation or merging of adjacent large eddies that accompanies the entrainment process. This also explains why the intermittency and bursting frequencies for all four flows remained about constant after cessation of entrainment.

Simpson and Wallace found that

$$V_E = 10F_\delta(-\overline{uv})_{max}/U_\infty \qquad (19)$$

described the entrainment velocity upstream of cessation for flows A and B. This scale characterizes the large eddy structure that is not only largely responsible for the various turbulence intensity levels in the turbulent fluid, but is directly responsible for the entrainment. When the negative normal stresses turbulence energy production term arises under strong acceleration, the available turbulence kinetic energy in the outer region is reduced so less large eddy energy is available for entrainment. This equation reduces to Bradshaw's relation for low acceleration boundary layers when $F_\delta = 1$. F_δ is given by equation (18) with all quantities evaluated at the boundary layer thickness δ. Using the relations $-\overline{uv} \simeq 0.15\,\overline{q^2}$, $\overline{u^2} \approx \frac{1}{2}\,\overline{q^2}$, and $\overline{v^2} \simeq 0.2\overline{q^2}$, which apply to entraining flows, they obtained

$$F_\delta = 1 - \frac{2K}{(\partial f/\partial \eta)_\delta} \qquad (20)$$

Figure 36 shows this quantity along flows C and D. Note that negative values of F_δ occur after engulfment of non-turbulent fluid ceases. This does not mean that turbulent fluid is instantaneously reverting to a laminar state, but simply that progressively more turbulent fluid lies outside the δ location.

Figures 7 and 8 show the results obtained by integrating equation (19)

$$U_\infty(\delta - \delta^*)\Big]_{x_0}^{x} = \int_{x_0}^{x} V_E\,dx \qquad (21)$$

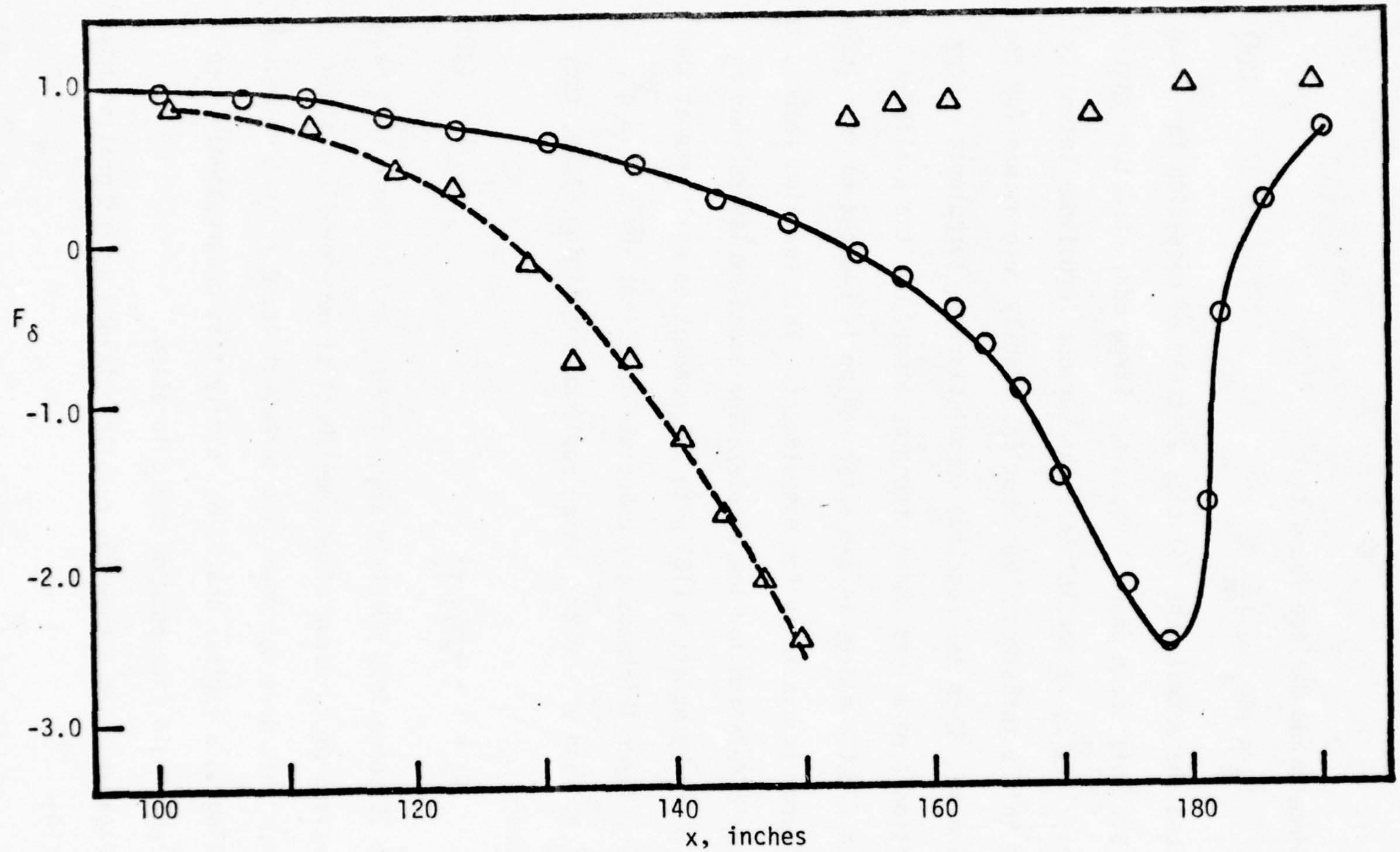

Figure 36. F_δ vs. x. Experimental values in eqn. (20): O, flow C; Δ, flow D. Lines for visual aid only.

For these computations the relation $(-\overline{uv})_{max} \approx 0.3(\overline{u^2})_{max}$ was used with experimental $(\overline{u^2})_{max}$ values. The results are in good agreement with values determined directly from the mean velocity profiles, especially for flow C. Thus the growth and decline of the mean flow boundary layer is fairly well predicted by this model, at least to just downstream of the cessation of entrainment.

The observed flat nF(n) region for $\overline{u^2}$ spectra emerges after some length of acceleration. The streamwise location where this behavior is first noticed does not seem to be directly related to the location where entrainment ceases. For flow A with $K = 2.17 \times 10^{-6}$, the nF(n) spectra examined by Simpson and Wallace had no flat region, even downstream of the cessation of entrainment. For flow B with $K = 3.19 \times 10^{-6}$, no flat region was present in the spectra obtained upstream of the minimum H, while such a region was observed for spectra downstream. In flow C presented here, the flat region in some spectra began at about 137 inches while the cessation of entrainment did not occur until about 165 inches. Similarly for flow D entrainment ceased at about 132 inches while the flat nF(n) region began at about 123 inches. A preliminary exploration of this behavior is that with strong acceleration, progressively weaker new low frequency oscillations are produced by the large-scaled motion while the higher frequency oscillations are produced by the breakdown of the more intense upstream large-scaled motions. Further analysis of these data is needed.

In flows A and B, asymptotic similarity flows were approached near the downstream end of the test section. This means that $\sqrt{\overline{u^2}}/U_\infty$ vs. η similarity was present for $K < 3.19 \times 10^{-6}$. For flow C when $K > 3.6 \times 10^{-6}$, $\sqrt{\overline{u^2}}/U_\infty$ profiles decayed. This means that had this K level been maintained downstream, true relaminarization would have eventually resulted, as suggested by Kline et al. (1967). Since there is a much shorter distance from the beginning of acceleration to the maximum K in flow D, the intensity $\sqrt{\overline{u^2}}/U_\infty$ did not begin to decay near the wall until about 157 inches. At 161.6 inches, as shown in figure 20, a considerable amount of the intensity was due to unsteadiness rather than turbulence. Since K decreased downstream of 144 inches, retransition to a low acceleration turbulent boundary layer began at about 165 inches. In this region the flow possessed a highly laminar-like behavior, so $-\overline{uv}$ was extremely small. Evidently $\sqrt{\overline{v^2}}$ decays considerably. As mentioned above, the surface spanwise structure upstream of the onset of decay of $\sqrt{\overline{u^2}}/U_\infty$ was not appreciably different from that of a low Reynolds number low pressure gradient boundary layer. After the onset of decay of $\sqrt{\overline{u^2}}/U_\infty$, λ_z^+ increased. Evidently the upstream λ_z values in these non-equilibrium flows persist downstream, so when normalized with a higher U_τ/ν, λ_z^+ is higher.

In the relaminarizing nozzle-type flow of Schraub and Kline (Kline et al. 1967), λ_z^+ was reported for the region of maximum K to be of the order of 200 for $K = 2.75 \times 10^{-6}$ and of the order of 300 for $K - 3.25 \times 10^{-6}$. On the surface, it would appear that they found

λ_z^+ to vary directly with K. However, their estimates of $C_f/2$ for these two streamwise locations seem high by about a factor of two when compared to the $C_f/2$ behavior in flow D and in the Blackwelder and Kovasznay (1972) nozzle flow. In that case, values of about 150 and 220 for λ_z^+ would result, respectively, and would agree reasonably well with the flow D results in the vicinity of the maximum K.

Schraub and Kline did not present λ_z results downstream of the K maximum, so the data from flow D are the only available on this downstream structure. λ_z^+ is still of the order of 300 while K decreases below 2×10^{-6}. After retransition to a low-accelerated low-pressure-gradient turbulent boundary layer begins, λ_z^+ is an order of magnitude greater. This behavior is as yet incompletely explained, so further analysis of these data is needed.

5. CONCLUSIONS AND RECOMMENDATIONS

The following conclusions can be made about turbulent boundary layers subjected to strong acceleration.

a. The parameter K must be greater than about 3.6×10^{-6} for the decay of the upstream generated turbulence.

b. For practical use in a nozzle only one short region downstream of the maximum K will possess a laminar-like behavior with significantly lower $C_f/2$ and heat transfer coefficients.

c. The large eddy structure of the outer region governs the bursting frequency, the intermittent bulge passage frequency, and influences the wall flow behavior downstream. These frequencies seem to approach constant values after the cessation of entrainment of non-turbulent fluid.

d. The wall spanwise structure appears to lag behind local conditions and to reflect upstream flow behavior. λ_z^+ seems to steadily increase to about 300 even after K has dropped below its maximum value in a nozzle flow. After retransition to a low accelerated turbulent boundary layer, a large λ_z^+ of the order of 3000 is observed.

e. The proposed modified entrainment model accounts for the reduction of available turbulence kinetic energy by the negative normal stresses production term of the turbulence kinetic energy equation.

f. A nF(n) spectral distribution of $\overline{u^2}$ for $\eta > 1000$ appears to possess a flat region for laminar like boundary layers at large K values.

As a result of the large quantity of experimental data provided by the research program, the following recommendations for future work are suggested.

a. Further analysis of these data, some of which was not presented in this report because of the lack of time. Afterwards a manuscript should be submitted for journal publication. At that time a more intelligent assessment for future work can be made.

b. A generalized computational effort incorporating flow models reflected by all available data should be undertaken. Communication between the senior author and predictors has begun, but no results are yet available.

REFERENCES

Blackwelder, R. F. and Kovasznay, L.S.G. (1972), "Large-scale Motion of a Turbulent Boundary Layer during Relaminarization," J. Fluid Mech., 53, pp. 61-83.

Bradshaw, P. (1967a) "The Turbulence Structure of Equilibrium Boundary Layers," J. Fluid Mech., 29, pp. 625-645.

Bradshaw, P. (1967b), "Conditions for the Existence of an Inertial Subrange in Turbulent Flow," Nat. Phys. Lab., Aero. Rept. No. 1220.

Collis, D. C. and Williams, M. J. (1959), "Two-Dimensional Convection from Heated Wires at Low Reynolds Numbers," J. Fluid Mech., 6, pp. 357-384.

Corrsin, S. (1964), "Further Generalizations of Onsager's Cascade Model for Turbulent Spectra," Phys. Fluids, 7, p. 1156.

Fiedler, H. and Head, M. R. (1966), "Intermittency Measurements in the Turbulent Boundary Layer," J. Fluid Mech., 25, pp. 719-735.

Freymurth, P. (1967), "Feedback Control Theory for Constant-Temperature Hot-Wire Anemometers," Rev. Sci. Inst., 38, pp. 677-681.

Gupta, A. K., Laufer, J., and Kaplan, R. E. (1971), "Spatial Structure in the Viscous Sublayer," J. Fluid Mech., 50, pp. 493-512.

Hinze, J. (. (1975), Turbulence, Second Edition, McGraw-Hill Book Co.

Kays, W. M. (1966), Convective Heat and Mass Transfer, McGraw-Hill Book Co.

Klebanoff, P. S. (1955), "Characteristics of Turbulence in a Boundary Layer with Zero Pressure Gradient," NACA Rept. 1247.

Kline, S. J., and McClintock, F. A. (1953), "Describing Uncertainties in Single-Sample Experiments," Mech. Eng., 75, pp. 3-8.

Kline, S. J., Reynolds, W. C., Schraub, F. A., and Runstadler, P. W. (1967), "The Structure of Turbulent Boundary Layers," J. Fluid Mech., 30, pp. 741-773.

Laufer, J. (1954), "The Structure of Turbulence in Fully-developed Pipe Flow," NACA Rept. 1174.

Moretti, P. M. and Kays, W. M. (1965), "Heat Transfer to a Turbulent Boundary Layer with Varying Free-stream Velocity and Varying Surface Temperature--An Experimental Study," Int. J. Heat Mass Trans., 8, pp. 1187-1202.

Narasimha, R. and Sreenivasan, K. R. (1973), "Relaminarization in Highly Accelerated Turbulent Boundary Layers," J. Fluid Mech., 61, pp. 417-447.

Nychas, S. G., Hershey, H. C., and Brodkey, R. S. (1973), "A Visual Study of Turbulent Shear Flow," J. Fluid Mech., 61, pp. 513-540.

Oka, S. and Kostić, Ž. (1972), "Influence of Wall Proximity on Hot-Wire Velocity Measurements," DISA Information, No. 13, pp. 29-33.

Rao, K. Narahari, Narasimha, R., and Badri Narayanan, M. A. (1971), "The 'Bursting' Phenomenon in a Turbulent Boundary Layer," J. Fluid Mech., 48, pp. 339-352.

Rotta, J. C. (1962), "Turbulent Boundary Layers in Incompressible Flow," Progress in Aeronautical Sciences, Vol. 2, Pergamon Press.

Sandborn, V. A. (1976), "Effect of Velocity Gradients in Measurements of Turbulent Shear Stress," AIAA Journal, 14, pp. 400-402.

Schlichting, H. (1968), Boundary Layer Theory, 6th Edition, McGraw-Hill Book Co.

Simpson, R. L. (1970), "Characteristics of Turbulent Boundary Layers at Low Reynolds Numbers with and without Transpiration," J. Fluid Mech., 42, pp. 769-802.

Simpson, R. L. (1975), "Interpreting Signals of the Spanwise Spatial Structure in the Viscous Sublayer," Phys. Fluids., 18, pp. 1068-1069.

Simpson, R. L. (1976), "An Investigation of the Spatial Structure of the Viscous Sublayer," Max-Planck-Institut für Strömungsforschung Bericht 118/1976.

Simpson, R. L., Strickland, J. H., and Barr, P. W. (1974), "Laser and Hot-Film Anemometer Measurements in a Separating Turbulent Boundary Layer," Rept. WT-3, Southern Methodist University, Thermal and Fluid Sciences Center. Available from NTIS as AD-A001115.

Simpson, R. L., Strickland, J. H., and Barr, P. W. (1977), "Features of a Separating Turbulent Boundary Layer in the Vicinity of Separation," J. Fluid Mech., 79, pp. 553-594.

Simpson, R. L. and Wallace, D. B. (1975), "Laminariscent Turbulent Boundary Layers: Experiments on Sink Flows," Project SQUID Tech Rept. SMU-1-PU.

Spencer, B. W. and Jones, B. G. (1971), "Turbulence Measurements with the Split-Film Anemometer Probe," Proceedings of Symposium on Turbulence in Liquids, Univ. Mo.- Rolla, pp. 7-15.

Strickland, J. H. and Simpson, R. L. (1973), "The Separating Turbulent Boundary Layer: An Experimental Study of an Airfoil Type Flow," Rept. WT-2, Thermal and Fluid Sciences Center, Southern Methodist University. Available from NTIS as AD-771170/8GA.

Strickland, J. H. and Simpson, R. L. (1975), "Bursting Frequencies Obtained from Wall Shear Stress Fluctuations in a Turbulent Boundary Layer," Phys. Fluids, 18, pp. 306-308.

Wallace, J. M., Eckelmann, H., and Brodkey, R. S. (1972), "The Wall Region in Turbulent Shear Flow," J. Fluid Mech., 54, pp. 39-48.

Willmarth, W. W. (1975), "Structure of Turbulence in Boundary Layers," Advances in Applied Mechanics, 15, pp. 159-253. Academic Press.

Young, M. F. (1976), "Calibration of Hot-wires and Hot-films for Velocity Fluctuations," Rept. TMC-3, Thermosciences Div., Dept. Mechanical Engrg., Stanford Univ.

APPENDIX A - Mean velocity and streamwise fluctuation intensity $\overline{(u^2)}^{1/2}/U_\infty$ profile data, flow C, linearly increasing K

X = 101.2

N	F	INTENSITY
27.	.1327	0.0339
32.	.1382	0.0361
39.	.1491	0.0392
45.	.1809	0.0484
57.	.2039	0.0549
65.	.2412	0.0651
91.	.3136	0.0776
114.	.3717	0.0883
136.	.4112	0.0922
182.	.4879	0.0947
227.	.5329	0.0959
273.	.5636	0.0940
364.	.6053	0.0860
454.	**.6229**	0.0804
565.	.6535	0.0784
692.	.6721	0.0736
909.	.6875	0.0708
1135.	.7039	0.0669
1363.	.7171	0.0657
1590.	.7215	0.0661
1818.	.7257	0.0667
2272.	.7522	0.0667
2726.	.7643	0.0673
3635.	.7971	0.0668
4544.	.8322	0.0639
5453.	.8629	0.0610
6362.	.8904	0.0571
7271.	.9178	0.0525
8179.	.9408	0.0474
9088.	.9627	0.0421
10224.	.9828	0.0333
11360.	.9934	0.0289
12496.	.9989	0.0234
13632.	1.0000	0.0203

X = 112.2

N	F	INTENSITY
38.	.1152	0.0337
43.	.1215	0.0384
48.	.1351	0.0436
52.	.1495	0.0478
62.	.1649	0.0549
71.	.1869	0.0614
83.	.2157	0.0692
95.	.2482	0.0778
119.	.3016	0.0902
143.	.3581	0.0951
167.	.4021	0.0998
190.	.4335	0.1005
238.	.4901	0.1035
285.	**.5319**	0.1035
381.	.5927	0.1004
476.	.6356	0.0897
595.	.6670	0.0891
714.	.6869	0.0853
952.	.7194	0.0752
1190.	.7414	0.0696
1428.	.7600	0.0653
1665.	.7717	0.0637
1903.	.7822	0.0626
2379.	.7969	.0597
2855.	.8136	0.0583
3807.	.8408	0.0576
4758.	.8649	0.0548
5710.	.8869	0.0519
6662.	.9110	0.0516
7613.	.9330	0.0494
8565.	.9518	0.0467
9517.	.9717	0.0444
10706.	.9937	0.0379
11896.	1.0000	0.0275

X = 118.8

N	F	INTENSITY
22.	.1172	0.0258
28.	.1208	0.0288
34.	.1252	0.0327
45.	.1439	0.0409
56.	.1599	0.0457
70.	.1874	0.0538
84.	.2176	0.0620
112.	.2457	0.0802
140.	.3632	0.0898
168.	.4130	0.0950
224.	.4840	0.1021
281.	.5453	0.1020
337.	.5888	0.1011
449.	**.6448**	0.0949
561.	.6821	0.0868
701.	.7114	0.0795
842.	.7291	0.0726
1122.	.7549	0.0646
1403.	.7735	0.0576
1683.	.7842	0.0549
2244.	.8078	0.0519
2805.	.8162	0.0506
3366.	.8313	0.0502
4488.	.8579	0.0502
5610.	.8819	0.0523
6732.	.8996	0.0515
7855.	.9236	0.0494
8977.	.9432	0.0462
10099.	.9645	0.0408
11221.	.9787	0.0340
12623.	.9947	0.0264
14026.	1.0000	0.0184

X = 123.1

N	F	INTENSITY
56.	.1604	0.0494
61.	.1693	0.0505
67.	.1863	0.0570
81.	.2282	0.0648
95.	.2674	0.0752
109.	.3004	0.0811
123.	.3431	0.0867
151.	.4091	0.0954
179.	.4733	0.0997
207.	.5178	0.0999
235.	.5588	0.1024
291.	.6096	0.1007
347.	.6506	0.0952
458.	**.6970**	0.0875
570.	.7228	0.0813
710.	.7487	0.0699
850.	.7602	0.0661
1129.	.7825	0.0598
1409.	.7968	0.0551
1688.	.8102	0.0524
1969.	.8191	0.0516
2247.	.8316	0.0498
2806.	.8396	0.0497
3365.	.8485	0.0488
4484.	.8708	0.0480
5602.	.8948	0.0467
6720.	.9180	0.0448
7838.	.9385	0.0416
8956.	.9572	0.0372
10074.	.9742	0.0306
11192.	.9875	0.0233
12590.	.9973	0.0157
13987.	1.0000	0.0103

y shift = 0.002

BEST AVAILABLE COPY

X = 128.6

N	F	INTENSITY
27.	.1109	0.0198
34.	.1168	0.0246
40.	.1271	0.0311
54.	.1523	0.0400
67.	.1826	0.0481
81.	.2084	0.0554
94.	.2449	0.0645
108.	.2712	0.0705
121.	.3045	0.0764
135.	.3333	0.0801
152.	.3622	0.0860
169.	.3976	0.0909
252.	.4545	0.0982
278.	.5432	0.1009
337.	.6174	0.1009
404.	.6649	0.0990
539.	.7302	0.0885
674.	.7605	0.0817
843.	.7923	0.0730
1011.	[illegible]	0.0676
1349.	.8103	0.0573
1685.	.8455	0.0506
2022.	.8564	0.0470
2357.	.8662	0.0445
2697.	.8744	0.0432
3371.	.8825	0.0408
4045.	.8905	0.0382
5393.	.9207	0.0367
6741.	.9327	0.0344
8099.	.9490	0.0317
9439.	.9638	0.0288
10786.	.9741	0.0250
12135.	.9867	0.0192
13483.	.9948	0.0132
15168.	1.0000	0.0100

X = 132.2

N	F	INTENSITY
62.	.1902	0.0551
68.	.2150	0.0618
75.	.2259	0.0623
82.	.2456	0.0659
92.	.2813	0.0727
109.	.3302	0.0809
126.	.3724	0.0871
144.	.4176	0.0919
178.	.5080	0.0963
212.	.5729	0.0994
246.	.6137	0.0998
280.	.6531	0.0996
349.	.7114	0.0958
417.	.7422	0.0921
554.	.7915	0.0819
690.	.8171	0.0741
863.	.8418	0.0656
1032.	.8557	0.0600
1374.	.8695	0.0508
1716.	.8817	0.0457
2058.	.8885	0.0426
2399.	.8958	0.0405
2741.	.9052	0.0373
3425.	.9155	0.0354
4108.	.9227	0.0343
4792.	.9308	0.0328
5476.	.9375	0.0318
6843.	.9526	0.0293
8210.	.9657	0.0267
9577.	.9767	0.0226
10945.	.9854	0.0170
12312.	.9913	0.0129
13679.	.9956	0.0093
15388.	1.0000	0.0071

y shift = 0.001

X = 136.7

N	F	INTENSITY
33.	.1317	0.0265
42.	.1413	0.0304
50.	.1508	0.0343
67.	.1807	0.0415
83.	.2118	0.0514
100.	.2490	0.0584
117.	.2896	0.0657
133.	.3291	0.0705
150.	.3698	0.0761
167.	.4069	0.0797
187.	.4518	0.0839
208.	.4857	0.0873
250.	.5577	0.0941
291.	.6145	0.0967
333.	.6679	0.0969
416.	.7289	0.0918
500.	.7708	0.0870
666.	.8223	0.0813
833.	.8510	0.0699
1041.	[illegible]	0.0606
1249.	.8833	0.0508
1665.	.8983	0.0407
2081.	.9037	0.0360
2498.	.9102	0.0335
2914.	.9144	0.0316
3330.	.9186	0.0300
4163.	.9276	0.0280
4996.	.9378	0.0267
6661.	.9515	0.0249
8326.	.9659	0.0226
9991.	.9755	0.0196
11656.	.9874	0.0159
13321.	.9940	0.0122
14987.	.9982	0.0090
16652.	1.0000	0.0072

X = 140.7

N	F	INTENSITY
115.	.2952	0.0731
124.	.3132	0.0738
133.	.3386	0.0754
150.	.3701	0.0797
168.	.4113	0.0819
186.	.4462	0.0869
203.	.4794	0.0892
226.	.5149	0.0910
248.	.5532	0.0923
292.	.6169	0.0928
336.	.6738	0.0928
380.	.7138	0.0915
469.	.7718	0.0826
557.	.8135	0.0745
734.	.8552	0.0604
911.	.8845	0.0613
1132.	.9025	0.0561
1353.	.9177	0.0490
1795.	.9324	0.0360
2238.	.9416	0.0290
2680.	.9538	0.0264
3122.	.9577	0.0251
3564.	.9611	0.0248
4449.	.9696	0.0232
5333.	.9713	0.0226
7102.	.9775	0.0222
8871.	.9865	0.0167
10639.	.9921	0.0154
12408.	.9977	0.0090
14177.	1.0000	0.0065

y shift = 0.003

X = 143.8

N	F	INTENSITY
10.	.1185	0.0134
21.	.1232	0.0170
31.	.1308	0.0232
42.	.1418	0.0291
52.	.1541	0.0346
73.	.1789	0.0448
94.	.2079	0.0528
115.	.2578	0.0593
136.	.2940	0.0667
157.	.3406	0.0717
183.	.3925	0.0787
209.	.4377	0.0830
262.	.5303	0.0918
314.	.6028	0.0961
367.	.6670	0.0991
471.	.7550	0.0946
576.	.8173	0.0873
786.	.8782	0.0682
995.	.9177	0.0545
1204.	.9282	0.0552
1414.	.9336	0.0391
1623.	.9436	0.0363
1833.	.9477	0.0349
2042.	.9510	0.0317
2304.	.9543	0.0301
2566.	.9586	0.0276
3091.	.9643	0.0267
4137.	.9705	0.0222
5180.	.9748	0.0193
6232.	.9764	0.0179
8326.	.9842	0.0150
10421.	.9924	0.0132
12516.	.9971	0.0102
14610.	1.0000	0.0077

y shift = -0.006

X = 146.8

N	F	INTENSITY
79.	.2016	0.0467
90.	.2254	0.0498
102.	.2492	0.0523
113.	.2722	0.0551
124.	.3008	0.0648
136.	.3304	0.0618
152.	.3599	0.0657
181.	.4217	0.0705
209.	.4784	0.0762
237.	.5404	0.0805
265.	.5893	0.0845
294.	.6317	0.0864
322.	.6698	0.0874
350.	.6974	0.0856
407.	.7472	0.0843
463.	.7949	0.0784
520.	.8350	0.0720
576.	.8510	0.0745
689.	.8827	0.0657
802.	.9087	0.0559
915.	.9272	0.0500
1141.	.9378	0.0424
1367.	.9493	0.0352
1593.	.9554	0.0305
1819.	.9596	0.0280
2044.	.9634	0.0251
2270.	.9656	0.0230
2553.	.9678	0.0214
2835.	.9696	0.0200
3400.	.9746	0.0184
4527.	.9788	0.0160
5657.	.9819	0.0152
6787.	.9859	0.0140
7918.	.9885	0.0134
9048.	.9912	0.0125
11307.	.9956	0.0100
13566.	.9987	0.0076
15825.	1.0000	0.0060

y shift = 0.001

X = 149.7

N	F	INTENSITY
92.	.2313	0.0513
105.	.2469	0.0553
131.	.2924	0.0628
158.	.3391	0.0694
184.	.3876	0.0743
210.	.4410	0.0802
237.	.4839	0.0832
263.	.5210	0.0874
296.	.5658	0.0883
328.	.6060	0.0899
394.	.6826	0.0889
460.	.7363	0.0857
526.	.7884	0.0813
657.	.8517	0.0708
788.	.8921	0.0618
1051.	.9358	0.0463
1314.	.9526	0.0378
1577.	.9632	0.0261
1839.	.9689	0.0270
2102.	.9735	0.0243
2365.	.9765	0.0222
2628.	.9784	0.0202
2956.	.9809	0.0184
3285.	.9818	0.0172
3942.	.9833	0.0155
5256.	.9871	0.0137
6570.	.9896	0.0128
7883.	.9917	0.0119
10511.	.9962	0.0099
13139.	.9989	0.0080
15767.	1.0000	0.0064

X = 152.6

N	F	INTENSITY
153.	.3481	0.0652
160.	.3677	0.0668
183.	.3954	0.0697
199.	.4221	0.0705
214.	.4449	0.0732
229.	.4733	0.0742
252.	.5212	0.0744
290.	.5727	0.0812
329.	.6177	0.0812
367.	.6646	0.0796
405.	.6978	0.0790
443.	.7304	0.0795
482.	.7634	0.0785
520.	.7898	0.0787
596.	.8364	0.0758
673.	.8755	0.0720
749.	.8998	0.0680
825.	.9175	0.0619
978.	.9469	0.0528
1131.	.9615	0.0446
1284.	.9716	0.0414
1590.	.9853	0.0307
1896.	.9922	0.0253
2201.	.9958	0.0214
2507.	.9977	0.0194
2813.	1.0000	0.0171

y shift = 0.004

X = 157.5

N	F	INTENSITY
100.	.2346	0.0660
119.	.2677	0.0719
138.	.3145	0.0768
156.	.3523	0.0776
175.	.3912	0.0779
213.	.4650	0.0780
251.	.5242	0.0753
288.	.5750	0.0753
326.	.6266	0.0756
364.	.6702	0.0764
401.	.7054	0.0761
448.	.7454	0.0754
495.	.7844	0.0733
532.	.8381	0.0658
684.	.8789	0.0606
778.	.9053	0.0566
966.	.9492	0.0460
1155.	.9638	0.0384
1532.	.9862	0.0282
1908.	.9944	0.0217
2295.	.9979	0.0177
2662.	.9992	0.0153
3039.	1.0000	0.0137

y shift = 0.0013

X = 161.6

N	F	INTENSITY
135.	.3218	0.0769
159.	.3513	0.0806
183.	.3668	0.0789
207.	.3776	0.0811
231.	.3947	0.0789
256.	.4212	0.0788
280.	.4528	0.0784
328.	.5232	0.0775
376.	.5844	0.0773
424.	.6212	0.0762
473.	.6565	0.0760
533.	.7146	0.0731
593.	.7495	0.0714
714.	.8105	0.0708
834.	.8543	0.0668
955.	.8981	0.0614
1196.	.9415	0.0504
1437.	.9626	0.0426
1919.	.9872	0.0259
2401.	.9944	0.0187
2884.	.9965	0.0145
3366.	.9986	0.0116
3848.	1.0000	0.0102

y shift = -0.0004

X = 172.6

N	F	INTENSITY
291.	.3290	0.0924
333.	.3512	0.0944
375.	.3852	0.0959
416.	.4260	0.0954
458.	.4622	0.0938
500.	.5034	0.0911
541.	.5356	0.0899
624.	.5972	0.0816
708.	.6451	0.0749
791.	.6865	0.0712
874.	.7229	0.0693
957.	.7566	0.0691
1062.	.7957	0.0682
1166.	.8236	0.0684
1374.	.8727	0.0558
1582.	.9099	0.0620
1790.	.9263	0.0589
2206.	.9516	0.0497
2623.	.9679	0.0414
3039.	.9776	0.0347
3455.	.9828	0.0278
3872.	.9883	0.0219
4288.	.9917	0.0179
5120.	.9969	0.0122
5953.	1.0000	0.0091

y shift = 0.003

X = 179.7

N	F	INTENSITY
283.	.4745	0.0865
331.	.4903	0.0882
378.	.5119	0.0899
425.	.5133	0.0895
472.	.5333	0.0895
567.	.5766	0.0867
661.	.6095	0.0849
756.	.6376	0.0838
850.	.6649	0.0825
945.	.7026	0.0834
1063.	.7262	0.0813
1181.	.7451	0.0797
1417.	.7727	0.0768
1654.	.7943	0.0746
1890.	.8157	0.0723
2362.	.8547	0.0687
2835.	.8849	0.0659
3307.	.9121	0.0624
3780.	.9360	0.0573
4724.	.9412	0.0492
5669.	.9677	0.0403
6614.	.9871	0.0307
7559.	.9991	0.0155
8504.	1.0000	0.0104

X = 189.63

N	F	INTENSITY
305.	.4988	0.0836
356.	.5244	0.0818
407.	.5436	0.0816
458.	.5585	0.0812
509.	.5732	0.0809
610.	.6020	0.0811
712.	.6162	0.0798
814.	.6297	0.0789
916.	.6451	0.0783
1017.	.6560	0.0773
1144.	.6687	0.0767
1272.	.6782	0.0760
1399.	.6956	0.0753
1526.	.7065	0.0743
1780.	.7234	0.0727
2034.	.7382	0.0710
2543.	.7596	0.0684
3052.	.7809	0.0661
3560.	.7993	0.0640
4069.	.8127	0.0620
4578.	.8331	0.0594
5086.	.8472	0.0576
6103.	.8759	0.0532
7121.	.8865	0.0501
8138.	.9105	0.0461
9155.	.9312	0.0423
10172.	.9537	0.0362
11444.	.9193	0.0283
12715.	.9904	0.0217
13987.	.9963	0.0152
15259.	1.0000	0.0112

APPENDIX B - Mean velocity and streamwise fluctuation intensity $(\overline{u^2})^{1/2}/U$ profile data, flow D, nozzle flow

X = 88.0

N	F	INTENSITY
45.	.1175	0.0190
67.	.1454	0.0320
89.	.1723	0.0407
134.	.2372	0.0623
178.	.2942	0.0789
223.	.3446	0.0863
290.	.4005	0.0897
357.	.4509	0.0885
446.	.4924	0.0896
558.	.5124	0.0834
669.	.5326	0.0821
892.	.5616	0.0766
1227.	.5986	0.0725
1561.	.6198	0.0702
2007.	.6467	0.0683
2676.	.6791	0.0669
3568.	.7194	0.0649
4460.	.7586	0.0649
5575.	.8011	0.0628
6690.	.8469	0.0614
7805.	.8883	0.0576
8920.	.9275	0.0516
10035.	.9588	0.0403
11150.	.9834	0.0270
12265.	.9969	0.0173
13380.	.9997	0.0130
14495.	1.0000	0.0111

X = 101.10

N	F	INTENSITY
64.	.1375	0.0288
85.	.1657	0.0388
127.	.2503	0.0648
170.	.3150	0.0802
212.	.3643	0.0897
276.	.4266	0.0926
340.	.4642	0.0947
425.	.5089	0.0941
531.	.5430	0.0874
637.	.5676	0.0834
849.	.5900	0.0792
1062.	.6099	0.0746
1274.	.6276	0.0710
1698.	.6628	0.0700
2123.	.6828	0.0656
2760.	.7122	0.0637
3397.	.7310	0.0629
4246.	.7815	0.0623
5308.	.8039	0.0594
6369.	.8415	0.0588
7431.	.8779	0.0558
8492.	.9143	0.0531
9554.	.9425	0.0438
10615.	.9696	0.0346
11677.	.9872	0.0227
12738.	.9960	0.0159
13800.	1.0000	0.0138
14861.	.9994	0.0114
15923.	.9989	0.0107

X = 106.90

N	F	INTENSITY
43.	.1199	0.0170
64.	.1420	0.0284
86.	.1735	0.0408
129.	.2410	0.0618
171.	.3062	0.0810
214.	.3597	0.0892
279.	.4261	0.0928
343.	.4610	0.0945
429.	.5006	0.0926
536.	.5425	0.0889
643.	.5623	0.0833
857.	.5972	0.0755
1179.	.6310	0.0711
1500.	.6496	0.0678
1929.	.6740	0.0634
2572.	.6997	0.0627
3429.	.7322	0.0609
4286.	.7625	0.0598
5358.	.7951	0.0571
6430.	.8300	0.0547
7501.	.8673	0.0534
8573.	.9034	0.0529
9644.	.9336	0.0451
10716.	.9639	0.0357
11788.	.9814	0.0253
12859.	.9942	0.0176
13931.	.9988	0.0140
15002.	1.0000	0.0107

X = 112.0

N	F	INTENSITY
66.	.1341	0.0263
88.	.1705	0.0398
132.	.2444	0.0635
176.	.3137	0.0790
219.	.3763	0.0909
285.	.4320	0.0939
351.	.4843	0.0948
439.	.5161	0.0899
549.	.5604	0.0862
658.	.5820	0.0820
878.	.6093	0.0745
1097.	.6298	0.0709
1317.	.6468	0.0668
1756.	.6695	0.0633
2195.	.6923	0.0614
2853.	.7127	0.0608
3512.	.7389	0.0590
4390.	.7662	0.0608
5487.	.8048	0.0585
6585.	.8355	0.0579
7682.	.8696	0.0574
8779.	.9026	0.0551
9877.	.9344	0.0495
10974.	.9611	0.0397
12072.	.9823	0.0264
13169.	.9947	0.0201
14267.	.9991	0.0141
15364.	1.0000	0.0117
16462.	.9991	0.0103

X = 117.90

N	F	INTENSITY
46.	.1942	0.0348
69.	.2622	0.0541
92.	.3324	0.0650
139.	.4122	0.0751
185.	.4737	0.0771
231.	.5083	0.0812
301.	.5363	0.0801
370.	.5601	0.0792
462.	.5795	0.0767
578.	.5903	0.0740
694.	.6043	0.0708
925.	.6237	0.0658
1156.	.6442	0.0648
1387.	.6626	0.0607
1850.	.6798	0.0613
2312.	.6986	0.0567
3006.	.7198	0.0568
3469.	.7457	0.0557
4624.	.7683	0.0571
5780.	.8072	0.0585
6936.	.8417	0.0614
8092.	.8751	0.0576
9249.	.9001	0.0533
10405.	.9409	0.0452
11561.	.9641	0.0335
12717.	.9824	0.0246
13873.	.9938	0.0169
15029.	.9982	0.0125
16185.	1.0000	0.0103
17341.	.9995	0.0096

X = 123.15

N	F	INTENSITY
48.	.1215	0.0172
73.	.1637	0.0359
97.	.2203	0.0531
121.	.2348	0.0567
145.	.2739	0.0664
194.	.3521	0.0813
242.	.4077	0.0885
315.	.4664	0.0946
388.	.5086	0.0933
485.	.5467	0.0906
606.	.5869	0.0835
727.	.6054	0.0746
969.	.6353	0.0685
1454.	.6703	0.0600
1939.	.6919	0.0560
2544.	.7136	0.0541
3150.	.7331	0.0560
3877.	.7547	0.0575
4846.	.7825	0.0589
6058.	.8196	0.0608
7269.	.8474	0.0579
8481.	.8814	0.0566
9693.	.9154	0.0501
10904.	.9452	0.0423
12116.	.9668	0.0345
13327.	.9843	0.0240
14539.	.9936	0.0170
15750.	.9989	0.0125
16720.	1.0000	0.0107

X = 130.60

N	F	INTENSITY
50.	.2098	0.0138
60.	.1452	0.0251
75.	.1701	0.0348
100.	.2248	0.0541
125.	.2904	0.0706
151.	.3461	0.0786
201.	.4286	0.0887
251.	.4863	0.0918
326.	.5579	0.0872
401.	.6007	0.0837
502.	.6325	0.0794
627.	.6604	0.0714
753.	.6743	0.0691
1003.	.6962	0.0635
1505.	.7230	0.0561
2007.	.7469	0.0537
2634.	.7638	0.0555
3261.	.7777	0.0573
4014.	.7996	0.0592
5017.	.8235	0.0574
6272.	.8593	0.0561
7526.	.8891	0.0540
8781.	.9150	0.0489
10035.	.9408	0.0436
11289.	.9597	0.0366
12544.	.9776	0.0272
13798.	.9906	0.0194
15052.	.9975	0.0137
16307.	1.0000	0.0108
17310.	.9975	0.0096

X = 137.20

N	F	INTENSITY
43.	.1288	0.0122
54.	.1297	0.0165
65.	.1446	0.0242
81.	.1705	0.0373
108.	.2132	0.0559
135.	.2623	0.0658
162.	.3142	0.0765
188.	.3531	0.0837
215.	.3939	0.0903
269.	.4541	0.1020
350.	.5236	0.1043
431.	.5737	0.1016
538.	.6237	0.0944
673.	.6617	0.0849
808.	.6877	0.0787
1077.	.7146	0.0680
1346.	.7368	0.0629
1615.	.7525	0.0606
2154.	.7720	0.0588
2692.	.7905	0.0565
3500.	.8100	0.0531
4307.	.8332	0.0526
5384.	.8545	0.0510
6730.	.8804	0.0491
8076.	.9110	0.0451
9422.	.9296	0.0425
10768.	.9518	0.0377
12115.	.9703	0.0299
13461.	.9852	0.0252
14807.	.9944	0.0177
16153.	.9981	0.0116
17499.	1.0000	0.0107
18845.	.9991	0.0097

BEST AVAILABLE COPY

X = 143.50

N	F	INTENSITY
57.	.1461	0.0294
85.	.1998	0.0500
114.	.2600	0.0630
142.	.3126	0.0765
171.	.3537	0.0829
228.	.4316	0.0930
285.	.4885	0.0950
370.	.5568	0.0956
456.	.6085	0.0934
570.	.6549	0.0917
712.	.6890	0.0833
855.	.7074	0.0769
1140.	.7275	0.0728
1425.	.7512	0.0688
1710.	.7748	0.0623
2280.	.8002	0.0565
2850.	.8212	0.0522
3705.	.8440	0.0480
4560.	.8606	0.0454
5700.	.8825	0.0435
7125.	.9044	0.0405
8549.	.9245	0.0370
9974.	.9455	0.0336
11399.	.9648	0.0289
12824.	.9779	0.0229
14249.	.9901	0.0169
15674.	.9960	0.0116
17099.	.9990	0.0092
18524.	1.0000	0.0082
19949.	.9992	0.0079

X = 149.30

N	F	INTENSITY
60.	.1380	0.0198
91.	.1815	0.0404
121.	.2394	0.0570
151.	.3024	0.0731
181.	.3635	0.0864
242.	.4602	0.0960
302.	.5222	0.1035
362.	.5742	0.1073
423.	.6169	0.1039
483.	.6552	0.1038
604.	.7040	0.0966
755.	.7403	0.0875
906.	.7643	0.0775
1208.	.7915	0.0654
1510.	.8155	0.0567
1812.	.8207	0.0551
2416.	.8461	0.0469
3020.	.8634	0.0450
3926.	.8808	0.0406
4832.	.8973	0.0388
6039.	.9146	0.0362
7549.	.9328	0.0336
9059.	.9510	0.0308
10569.	.9675	0.0277
12079.	.9807	0.0225
13589.	.9907	0.0164
15099.	.9962	0.0131
16608.	.9999	0.0110
18118.	1.0000	0.0077
19628.	.9986	0.0069

X = 154.50

N	F	INTENSITY
53.	.1497	0.0288
67.	.1804	0.0406
83.	.2193	0.0514
100.	.2560	0.0585
133.	.3256	0.0744
167.	.3780	0.0850
200.	.4356	0.0923
233.	.4050	0.1019
267.	.5240	0.1059
333.	.5891	0.1084
433.	.6639	0.1088
533.	.7186	0.0978
667.	.7522	0.0877
833.	.7882	0.0772
1000.	.8189	0.0693
1333.	.8428	0.0582
1667.	.8593	0.0499
2000.	.8743	0.0461
2667.	.8915	0.0400
3333.	.9019	0.0364
4333.	.9139	0.0319
5333.	.9251	0.0314
6667.	.9386	0.0297
8333.	.9543	0.0277
10000.	.9678	0.0254
11667.	.9798	0.0213
13333.	.9895	0.0177
15000.	.9963	0.0127
16667.	.9993	0.0093
18333.	1.0000	0.0079
20000.	.9993	0.0078

X = 157.80

N	F	INTENSITY
42.	.1293	0.0161
56.	.1343	0.0202
70.	.1493	0.0289
87.	.1743	0.0398
105.	.2150	0.0501
140.	.2936	0.0676
175.	.3643	0.0829
210.	.4221	0.0954
279.	.5193	0.1056
349.	.5936	0.1126
454.	.6757	0.1089
559.	.7229	0.1006
699.	.7707	0.0911
873.	.8021	0.0759
1048.	.8307	0.0626
1397.	.8550	0.0544
1747.	.8693	0.0454
2096.	.8829	0.0409
2794.	.8957	0.0356
3493.	.9071	0.0329
4541.	.9229	0.0305
5589.	.9336	0.0279
6986.	.9457	0.0266
8733.	.9593	0.0259
10479.	.9714	0.0226
12226.	.9836	0.0186
13972.	.9914	0.0139
15719.	.9979	0.0106
17465.	1.0000	0.0087
19212.	1.0000	0.0079

X = 162.00

N	F	INTENSITY
78.	.2814	0.0650
97.	.2840	0.0657
116.	.3143	0.0728
136.	.3439	0.0760
155.	.3825	0.0876
194.	.4624	0.0998
232.	.5139	0.1075
271.	.5712	0.1108
310.	.5982	0.1108
387.	.6736	0.1082
504.	.7302	0.0998
620.	.7721	0.0799
775.	.8114	0.0721
969.	.8371	0.0617
1162.	.8500	0.0513
1550.	.8681	0.0449
1937.	.8758	0.0410
2712.	.9015	0.0359
3875.	.9190	0.0303
5037.	.9305	0.0290
6197.	.9408	0.0274
7749.	.9531	0.0266
9686.	.9666	0.0243
11624.	.9788	0.0207
13561.	.9904	0.0158
15498.	.9962	0.0132
17435.	.9985	0.0107
19373.	1.0000	0.0090
19992.	.9992	0.0088

X = 164.20

N	F	INTENSITY
67.	.1854	0.0415
83.	.2106	0.0438
104.	.2424	0.0511
125.	.3137	0.0611
166.	.4379	0.0816
208.	.5669	0.0876
250.	.6359	0.0876
291.	.6857	0.0816
333.	.7259	0.0744
416.	.7750	0.0672
499.	.7990	0.0630
582.	.8152	0.0606
707.	.8362	0.0558
832.	.8470	0.0529
1040.	.8668	0.0505
1248.	.8764	0.0475
1664.	.8902	0.0427
2080.	.9034	0.0380
2496.	.9100	0.0350
3327.	.9238	0.0321
4159.	.9346	0.0299
5407.	.9456	0.0273
6655.	.9544	0.0259
8318.	.9628	0.0234
10398.	.9766	0.0213
12478.	.9868	0.0175
14557.	.9940	0.0129
16637.	.9982	0.0106
18716.	1.0000	0.0091
20796.	.9994	0.0088

X = 166.80

N	F	INTENSITY
89.	.1962	0.0397
134.	.2723	0.0559
179.	.3629	0.0723
223.	.4422	0.0879
268.	.5138	0.0958
312.	.5759	0.0994
357.	.6167	0.0975
446.	.6922	0.0933
536.	.7380	0.0866
625.	.7760	0.0829
759.	.8163	0.0757
893.	.8448	0.0692
1116.	.8672	0.0564
1339.	.8862	0.0493
1785.	.9057	0.0412
2231.	.9186	0.0367
2678.	.9259	0.0314
3570.	.9359	0.0276
4463.	.9454	0.0252
5801.	.9555	0.0234
7140.	.9628	0.0213
8925.	.9728	0.0199
10710.	.9822	0.0174
12495.	.9880	0.0147
14280.	.9932	0.0131
16065.	.9973	0.0100
17850.	.9991	0.0092
19635.	1.0000	0.0083
21420.	.9990	0.0078

X = 170.80

N	F	INTENSITY
82.	.1792	0.0289
102.	.2179	0.0382
127.	.2684	0.0465
153.	.3262	0.0560
178.	.3766	0.0647
204.	.4231	0.0712
255.	.5113	0.0784
306.	.5916	0.0828
357.	.6533	0.0851
408.	.7081	0.0860
459.	.7434	0.0877
509.	.7742	0.0833
611.	.8252	0.0763
713.	.8570	0.0668
815.	.8795	0.0596
1019.	.9060	0.0497
1274.	.9216	0.0395
1528.	.9314	0.0346
2038.	.9432	0.0287
2547.	.9510	0.0252
3057.	.9564	0.0230
4076.	.9647	0.0200
5095.	.9706	0.0195
6623.	.9760	0.0170
8152.	.9814	0.0161
10190.	.9873	0.0146
12228.	.9927	0.0123
14265.	.9971	0.0105
16303.	.9990	0.0088
18341.	1.0000	0.0079
20379.	.9990	0.0072

X = 175.00

N	F	INTENSITY
96.	.2645	0.0465
120.	.3003	0.0556
144.	.3524	0.0638
179.	.4158	0.0705
209.	.4754	0.0763
239.	.5138	0.0805
299.	.5997	0.0909
359.	.6610	0.0980
419.	.7023	0.0938
479.	.7460	0.0905
598.	.8098	0.0847
718.	.8486	0.0751
838.	.8799	0.0651
957.	.9020	0.0609
1107.	.9266	0.0482
1496.	.9441	0.0393
1705.	.9545	0.0337
2303.	.9646	0.0279
2992.	.9712	0.0245
3590.	.9762	0.0223
4786.	.9804	0.0188
5983.	.9850	0.0171
7778.	.9892	0.0156
9573.	.9917	0.0142
11966.	.9962	0.0126
14359.	.9996	0.0103
16752.	1.0000	0.0093
19146.	1.0000	0.0084

X = 178.30

N	F	INTENSITY
89.	.2660	0.0626
118.	.3184	0.0699
148.	.3656	0.0775
185.	.4247	0.0864
222.	.4868	0.0925
259.	.5375	0.0993
296.	.5982	0.1047
370.	.6604	0.1053
443.	.7022	0.0982
517.	.7448	0.0955
591.	.7944	0.0955
739.	.8477	0.0841
887.	.8980	0.0699
1035.	.9237	0.0523
1182.	.9436	0.0419
1478.	.9588	0.0299
1848.	.9700	0.0242
2217.	.9743	0.0210
2956.	.9808	0.0176
3695.	.9838	0.0158
4804.	.9872	0.0132
5912.	.9902	0.0127
7390.	.9919	0.0112
9607.	.9946	0.0107
11824.	.9973	0.0098
14780.	.9993	0.0085
17737.	1.0000	0.0078
20693.	1.0000	0.0073

X = 181.20

N	F	INTENSITY
116.	.3040	0.0438
132.	.3273	0.0462
165.	.3892	0.0547
207.	.4680	0.0652
248.	.5402	0.0707
289.	.6042	0.0776
331.	.6434	0.0800
413.	.7337	0.0830
496.	.8046	0.0812
578.	.8439	0.0728
661.	.8786	0.0658
744.	.8989	0.0595
826.	.9185	0.0522
992.	.9402	0.0399
1157.	.9526	0.0335
1405.	.9638	0.0246
1653.	.9719	0.0206
2066.	.9768	0.0179
2479.	.9804	0.0149
3305.	.9858	0.0126
4132.	.9873	0.0113
5784.	.9925	0.0100
7437.	.9943	0.0092
9090.	.9964	0.0096
11569.	.9982	0.0086
14048.	1.0000	0.0078
17353.	1.0000	0.0068

X = 182.30

N	F	INTENSITY
108.	.1698	0.0215
144.	.2312	0.0338
180.	.2924	0.0388
225.	.3691	0.0460
270.	.4544	0.0562
315.	.5204	0.0579
360.	.5768	0.0640
414.	.6405	0.0712
468.	.6959	0.0720
541.	.7591	0.0715
631.	.8084	0.0698
721.	.8457	0.0629
811.	.8776	0.0579
901.	.9009	0.0526
1081.	.9313	0.0443
1261.	.9499	0.0377
1532.	.9665	0.0296
1802.	.9729	0.0241
2252.	.9806	0.0201
2703.	.9856	0.0173
3604.	.9903	0.0147
4505.	.9920	0.0138
5406.	.9939	0.0129
7208.	.9947	0.0116
9910.	.9967	0.0112
12613.	.9992	0.0107
15316.	1.0009	0.0099
18019.	.9992	0.0092

BEST AVAILABLE COPY

X = 185.80

N	F	INTENSITY
133.	.1849	0.0204
155.	.2049	0.0236
177.	.2443	0.0241
222.	.3153	0.0295
277.	.4013	0.0346
333.	.4917	0.0412
388.	.5749	0.0488
444.	.6374	0.0493
510.	.7024	0.0486
577.	.7569	0.0511
664.	.8169	0.0553
776.	.8700	0.0538
887.	.9098	0.0477
998.	.9330	0.0394
1109.	.9505	0.0355
1331.	.9746	0.0277
1553.	.9829	0.0232
1886.	.9861	0.0178
2219.	.9906	0.0149
2662.	.9933	0.0131
3106.	.9951	0.0122
3661.	.9960	0.0107
4437.	.9969	0.0103
5546.	.9984	0.0097
7765.	.9991	0.0091
10538.	.9996	0.0083
13311.	1.0000	0.0082

X = 190.10

N	F	INTENSITY
240.	.5442	0.0303
280.	.5803	0.0301
321.	.6177	0.0306
401.	.6787	0.0296
481.	.7298	0.0330
561.	.7796	0.0390
641.	.8207	0.0400
721.	.8580	0.0372
801.	.8842	0.0352
902.	.9128	0.0338
1002.	.9340	0.0305
1202.	.9577	0.0242
1402.	.9738	0.0198
1603.	.9838	0.0163
2003.	.9913	0.0124
2605.	.9964	0.0095
3206.	.9973	0.0089
4007.	.9984	0.0081
5009.	1.0000	0.0076
6010.	.9994	0.0079

APPENDIX C

ERRATA FOR REPORT SMU-1-PU

page	line	
10	bottom	"96 inches" should "93 inches"
11	6	"3.1672 x 10^{-4}(x)" should be "3.1627 x 10^{-4}(x)
11	6	"6.5931 x 10^{-6}(x^2)" should be "6.5931 x 10^{-7}(x^2)"
11	8	"1.1944 x 10^{-5}(x^2)" should be "1.1994 x 10^{-5}(x^2)"

GOVERNMENT AGENCIES

1. British Embassy
   3100 Massachusetts Avenue, N.W.
   Washington, D.C. 20008
   ATTN: Mr. J. Barry Jamieson
   Propulsion Officer

2. Central Intelligence Agency
   Washington, D.C. 20505
   ATTN: CRS/ADD/Publications

3. Institute for Defense Analyses
   400 Army-Navy Drive
   Arlington, Virginia 22202
   ATTN: Dr. Hans G. Wolfhard,
   Sen. Staff

4. Defense Documentation Center
   Cameron Station
   Alexandria, Virginia 22314

5. EPA Technical Center
   Research Triangle Park
   North Carolina 27711
   ATTN: Dr. W. Herget, P-222

6. Esso Research and Engineering Company
   Government Research Laboratory
   P.O. Box 8
   Linden, New Jersey 07036
   ATTN: Dr. William F. Taylor

7. Arnold Air Force Station
   Tennessee 36389
   ATTN: AEDC (DYF)

8. Arnold Air Force Station
   Tennessee 37389
   ATTN: R.E. Smith, Jr., Chief
   T-Cells Division
   Engine Test Facility

9. Air Force Aero Propulsion Laboratory
   Wright-Patterson Air Force Base
   Ohio 45433
   ATTN: STINFO Office

10. Air Force Eastern Test Range
    MU-135
    Patrick Air Force Base
    Florida 32925
    ATTN: AFETR Technical Library

11. Air Force Office of Scientific Research
    Bolling Air Force Base, Building 410
    Washington, D.C. 20332
    ATTN: Dr. Joseph F. Masi

12. Air Force Aero Propulsion Laboratory
    Wright-Patterson AFB, Ohio 45433
    ATTN: AFAPL/TBC
    Dr. Kervyn Mach

13. Air Force Aero Propulsion Laboratory
    Wright-Patterson AFB, Ohio 45433
    ATTN: AFAPL/TBC
    Francis R. Ostdiek

14. Air Force Rocket Propulsion Laboratory
    Department of Defense
    Edwards AFB, California 93523
    ATTN: LKCG (Mr. Selph)

15. U.S. Army Air Mobility Research and
    Development Laboratory
    Eustis Directorate
    Fort Eustis, Virginia 23604
    ATTN: Propulsion Division
    (SAVDL-EU-PP)

16. U.S. Army Artillery Combat
    Developments Agency
    Fort Sill, Oklahoma 73503
    ATTN: Commanding Officer

17. U.S. Army Missile Command
    Redstone Arsenal, Alabama 35809
    ATTN: AMSMI-RR

18. U.S. Army Missile Command
    Redstone Scientific Information Center
    Redstone Arsenal, Alabama 35809
    ATTN: Chief, Document Section

19. Indiana State Library
    140 North Senate Avenue
    Indianapolis, Indiana 46204
    ATTN: Patricia Matkovic
    Reference Librarian
    % Indiana Division

20. NASA Headquarters
    600 Independence
    Washington, D.C. 20546
    ATTN: Dr. Gordon Banerian

21. NASA Headquarters
    Aeronautical Propulsion Division
    Code RL, Deputy Director
    Office of Advanced Research & Technology
    Washington, D.C. 20546
    ATTN: Mr. Nelson F. Rekos

22. NASA Ames Research Center
    Deputy Chief Aeronautics Division
    Mail Stop 27-4
    Moffett Field, California 94035
    ATTN: Mr. Edward W. Perkins

23. NASA Ames Research Center
    Aerodynamics Branch 227-8
    Moffett Field, California 94305
    ATTN: Mr. Ira R. Schwartz

24. NASA Lewis Research Center
    21000 Brookpark Road
    Cleveland, Ohio 44135
    ATTN: D. Morris, Mail Stop 60-3

25. NASA Lewis Research Center
    Hypersonic Propulsion Section
    Mail Stop 6-1
    21000 Brookpark Road
    Cleveland, Ohio 44135
    ATTN: Dr. Louis A. Povinelli

26. NASA Marshall Space Flight Center
    S&E ASTN-P
    Huntsville, Alabama 35812
    ATTN: Mr. Keith Chandler

27. National Science Foundation
    Engineering Energetics
    Engineering Division
    Washington, D.C. 20550
    ATTN: Dr. George Lee

28. National Science Foundation
    Engineering Energetics
    Engineering Division
    Washington, D.C. 20550
    ATTN: Dr. M. Ojalvo

29. National Science Foundation
    Engineering Energetics
    Engineering Division
    Washington, D.C. 20550
    ATTN: Dr. Royal Rostenbach

30. Naval Air Development Center
    Commanding Officer (AD-5)
    Warminster, Pennsylvania 18974
    ATTN: NADC Library

31. Naval Air Propulsion Test Center (R&T)
    Trenton, New Jersey 08628
    ATTN: Mr. Al Martino

AD-A037 441 PURDUE UNIV LAFAYETTE IND PROJECT SQUID HEADQUARTERS F/G 20/4
LAMINARISCENT TURBULENT BOUNDARY LAYERS: EXPERIMENTS ON NOZZLE --ETC(U)
JAN 77 R L SIMPSON, C R SHACKLETON N00014-75-C-1143

UNCLASSIFIED SQUID-SMU-2-PU NL

2 OF 2
AD
A037441

END
DATE
FILMED
4-77

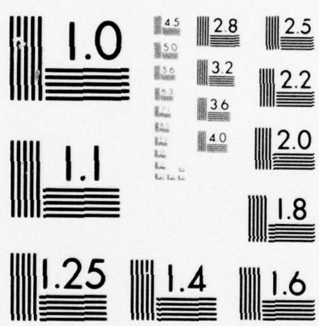

MICROCOPY RESOLUTION TEST CHART

NATIONAL BUREAU OF STANDARDS-1963-A

32. Naval Air Systems Command
Department of the Navy
Washington, D.C. 20360
ATTN: Research Administrator
AIR 310

33. Naval Air Systems Command
Department of the Navy
Washington, D.C. 20360
ATTN: Propulsion Technology Admin.
AIR 330

34. Naval Air Systems Command
Department of the Navy
Washington, D.C. 20360
ATTN: Technical Library Division
AIR 604

35. Naval Ammunition Depot
Research and Development Department
Building 190
Crane, Indiana 47522
ATTN: Mr. B.E. Douda

36. Naval Ordnance Laboratory Commander
White Oak
Silver Springs, Maryland 20910
ATTN: Library

37. Naval Ordnance Systems Command
Department of the Navy
Washington, D.C. 20360
ATTN: ORD 0331

38. Naval Postgraduate School
Department of Aeronautics, Code 57
Monterey, California 93940
ATTN: Dr. Allen E. Fuhs

39. Naval Postgraduate School
Library (Code 2124)
Monetrey, California 93940
ATTN: Superintendent

40. Naval Postgraduate School
Monterey, California 93940
ATTN: Library (Code 0212)

41. Office of Naval Research Branch Office
1030 East Green Street
Pasadena, California 91106
ATTN: Dr. Rudolph J. Marcus

42. Office of Naval Research Branch Office
536 South Clark Street
Chicago, Illinois 60605
ATTN: Commander

43. Office of Naval Research Branch Office
495 Summer Street
Boston, Massachusetts 02210
ATTN: Commander

44. Office of Naval Research
Power Branch, Code 473
Department of the Navy
Arlington, Virginia 22217

45. Office of Naval Research
Fluid Dynamics Branch, Code 438
Department of the Navy
Washington, D.C. 22217
ATTN: Mr. Morton Cooper

46. Naval Research Lab
Code 7710
Washington, D.C. 20390
ATTN: W.W. Balwanz

47. Naval Research Laboratory Director
Washington, D.C. 20390
ATTN: Technical Information Division

48. Naval Research Laboratory Director
Washington, D.C. 20390
ATTN: Library Code 2629 (ONRL)

49. Naval Ship Research and Development Center
Annapolis Division
Annapolis, Maryland 21402
ATTN: Library, Code A214

50. Naval Ship Systems Command
Department of the Navy
Washington, D.C. 20360
ATTN: Technical Library

51. Naval Weapons Center Commander
China Lake, California 93555
ATTN: Airbreathing Propulsion Branch
Code 4583

52. Naval Weapons Center
Chemistry Division
China Lake, California 93555
ATTN: Dr. William S. McEwan
Code 605

53. Naval Weapons Center
Commander
China Lake, California 93555
ATTN: Technical Library

54. Naval Weapons Center
Code 608, Thermochemistry Group
China Lake, California 93555
ATTN: Mr. Edward W. Price, Head

55. Naval Weapons Laboratory
Dahlgren, Virginia 22448
ATTN: Technical Library

56. Naval Undersea Research and
Development Center
San Diego, California 92132
ATTN: Technical Library
Code 1311D

57. Naval Underwater Systems Center
Fort Trumbull
New London, Connecticut 06320
ATTN: Technical Library

58. Naval Underwater Systems Center
Code 5B-331
Newport, Rhode Island 02840
ATTN: Dr. Robert Lazar

59. Picatinny Arsenal
Commanding Officer
Dover, New Jersey 07801
ATTN: Technical Information Library

60. State Documents Section
Exchange and Gift Division
Washington, D.C. 20540
ATTN: Library of Congress

U.S. INDUSTRIES AND LABORATORIES

61. AeroChem Research Laboratories, Inc.
P.O. Box 12
Princeton, New Jersey 08540
ATTN: Dr. Arthur Fontijn

62. AeroChem Research Laboratories, Inc.
P.O. Box 12
Princeton, New Jersey 08540
ATTN: Library

63. Aerojet Liquid Rocket Company
P.O. Box 13222
Sacramento, California 95813
ATTN: Technical Information Center

64. Aeronautical Research Association
of Princeton
50 Washington Road
Princeton, New Jersey 08540
ATTN: Dr. C. Donaldson

65. Aeroprojects, Inc.
West Chester
Pennsylvania 19380

66. The Aerospace Corporation
P.O. Box 92957
Los Angeles, California 90009
ATTN: Mr. Alexander Muraszew

67. Atlantic Research Corporation
5390 Cherokee Avenue
Alexandria, Virginia 22314
ATTN: Dr. Andrej Macek

68. Atlantic Research Corporation
5390 Cherokee Avenue
Alexandria, Virginia 22314
ATTN: Librarian

69. Atlantic Research Corporation
5390 Cherokee Avenue
Alexandria, Virginia 22314
ATTN: Dr. Kermit E. Woodcock
Manager, Propulsion

70. Avco Everett Research Laboratory
Everett, Massachusetts 02149
ATTN: Librarian

71. Avco Lycoming Corporation
550 South Main Street
Stratford, Connecticut 06497
ATTN: Mr. John W. Schrader

72. Ballistics Research Laboratory
Commanding Officer
Aberdeen Proving Ground, Maryland 21005
ATTN: Library

73. Battelle
Columbus Laboratories
505 King Avenue
Colubmus, Ohio 43201
ATTN: Mr. Abbott A. Putnam
Atmospheric Chemistry &
Combustion Systems Division

74. Beech Aircraft Corporation
9709 East Central
Wichita, Kansas 67201
ATTN: William M. Byrne, Jr.

75. Bell Aerospace Company
P.O. Box 1
Buffalo, New York 14240
ATTN: Technical Library

76. Bureau of Mines
Bartlesville Energy Research Center
Box 1398
Bartlesville, Oklahoma 74003

77. Calspan Corporation
4455 Genessee Street
Buffalo, New York 14221
ATTN: Head Librarian

78. Computer Genetics Corporation
Wakefield, Massachusetts 01880
ATTN: Mr. Donald Leonard
Technical Director

79. Convair Aerospace Division
Manager of Propulsion
P.O. Box 748
Fort Worth, Texas 76101
ATTN: L. H. Schreiber

80. Detroit Diesel Allison Division
P.O. Box 894
Indianapolis, Indiana 46206
ATTN: Dr. Sanford Fleeter

81. Dynalysis of Princeton
20 Nassau Street
Princeton, New Jersey 08540
ATTN: Dr. H.J. Herring

82. Fairchild Industries
Fairchild Republic Division
Farmingdale, New York 11735
ATTN: Engineering Library

83. Flame Research, Inc.
P.O. Box 10502
Pittsburgh, Pennsylvania 15235
ATTN: Dr. John Manton

84. Forest Fire and Engineering Research
Pacific Southwest Forest & Range
Experiment Station
P.O. Box 245
Berkeley, California 94701
ATTN: Assistant Director

85. Garrett Corporation
AiResearch Manufacturing Company
Sky Harbor Airport
402 South 36th Street
Phoenix, Arizona 85034
ATTN: Mr. Aldo L. Romanin, Mgr.
Aircraft Propulsion Engine
Product Line

86. General Dynamics
Electro Dynamic Division
P.O. Box 2507
Pomona, California 91766
ATTN: Library MZ 620

87. General Dynamics
P.O. Box 748
Fort Worth, Texas 76101
ATTN: Technical Library MZ 2246

88. General Electric Company
AEG Technical Information Center
Mail Drop N-32, Building 700
Cincinnati, Ohio 45215
ATTN: J.J. Brady

89. General Electric Company
SPO-Bldg, 174AE
1000 Western Avenue
West Lynn, Massachusetts 01910
ATTN: Mr. W. Bruce Gist

90. General Electric Space Sciences Lab
Valley Forge Space Technology Center
Room M-9144
P.O. Box 8555
Philadelphia, Pennsylvania 19101
ATTN: Dr. Theodore Baurer

91. General Motors Corporation
Detroit Diesel Allison Division
P.O. Box 894
Indianapolis, Indiana 46206
ATTN: Mr. P.C. Tram

92. General Motors Technical Center
Passenger Car Turbine Development
General Motors Engineering Staff
Warren, Michigan 48090
ATTN: T.F. Nagey, Director

93. Grumman Aerospace Corporation
Manager Space Vehicle Development
Bethpage, New York 11714
ATTN: Mr. O.S. Williams

94. Mr. Daniel L. Harshman
11131 Embassy Drive
Cincinnati, Ohio 45240

95. Hercules Incorporated
Allegany Ballistics Laboratory
P.O. Box 210
Cumberland, Maryland 21502
ATTN: Mrs. Louise S. Derrick
Librarian

96. Hercules Incorporated
P.O. Box 98
Magna, Utah 84044
ATTN: Library 100-H

97. LTV Vought Aeronautics Company
Flight Technology, Project Engineer
P.O. Box 5907
Dallas, Texas 75222
ATTN: Mr. James C. Utterback

98. Lockheed Aircraft Corporation
Lockheed Missiles and Space Company
Huntsville, Alabama 35804
ATTN: John M. Banefield
Supervisor Propulsion

99. Lockheed-Georgia Company
Dept. 72-47, Zone 259
Marietta, Georgia 30060
ATTN: William A. French

100. Lockheed Missiles and Space Company
3251 Hanover Street
Palo Alto, California 94304
ATTN: Palo Alto Library 52-52

101. Lockheed Propulsion Company
Scientific and Technical Library
P.O. Box 111
Redlands, California 92373
ATTN: Head Librarian

102. Los Alamos Scientific Laboratory
P.O. Box 1663
Los Alamos, New Mexico 97544
ATTN: J. Arthur Freed

103. The Marquardt Company
CCI Aerospace Corporation
16555 Saticoy Street
Van Nuys, California 91409
ATTN: Library

104. Martin-Marietta Corporation
P.O. Box 179
Denver, Colorado 90201
ATTN: Research Library 6617

105. Martin-Marietta Corporation
Orlando Division
P.O. Box 5837
Orlando, Florida 32805
ATTN: Engineering Library, mp-30

106. McDonnell Aircraft Company
P.O. Box 516
St. Louis, Missouri 63166
ATTN: Research & Engineering Library
Dept. 218 - Bldg. 101

107. McDonnell Douglas Corporation
Project Propulsion Engineer
Dept. 243, Bldg. 66, Level 25
P.O. Box 516
St. Louis, Missouri 63166
ATTN: Mr. William C. Paterson

108. McDonnell Douglas Astronautics Company
5301 Bolsa Avenue
Huntington Beach, California 92647
ATTN: A3-328 Technical Library

109. Nielsen Engineering and Research, Inc.
510 Clyde Avenue
Mountain View, California 94040
ATTN: Dr. Jack N. Nielsen

110. *Northrop Corporation*
Ventura Division
1515 Rancho Conejo Boulevard
Newbury Park, California 91230
ATTN: Technical Information Center

111. Mr. J. Richard Perrin
16261 Darcia Avenue
Encino, California 91316

112. Philco-Ford Corporation
Aeronutronic Division
Ford Road
Newport Beach, California 92663
ATTN: Technical Information Center

113. Pratt and Whitney Aircraft
Project Engineer, Advanced
Military System
Engineering Department - 2B
East Hartford, Connecticut 06108
ATTN: Mr. Donald S. Rudolph

114. Pratt and Whitney Aircraft Division
United Aircraft Company
400 South Main Street
East Hartford, Connecticut 06108
ATTN: Mr. Dana B. Waring
Manager-Product Technology

115. Pratt and Whitney Aircraft
Program Manager, Advanced
Military Engineer
Engineering Department - 2B
East Hartford, Connecticut 06108
ATTN: Dr. Robert I. Strough

116. Pratt and Whitney Aircraft
Florida Research and Development Company
P.O. Box 2691
West Palm Beach, Florida 33402
ATTN: Mr. William R. Alley
Chief of Applied Research

117. Rocket Research Corporation
11441 Willow Road
Redmond, Washington 98052
ATTN: Thomas A. Groudle

118. Rocketdyne Division
North American Rockwell
6633 Canoga Avenue
Canoga Park, California 91304
ATTN: Technical Information Center
D 596-108

119. Sandia Laboratories
P.O. Box 969
Livermore, California 94550
ATTN: Dr. Dan Hartley, Div. 8115

120. Sandia Laboratories
Livermore, California 94550
ATTN: Robert Gallagher

121. Sandia Laboratories
P.O. Box 5800
Albuquerque, New Mexico 87115
ATTN: Technical Library, 3141

122. Solar
2200 Pacific Highway
San Diego, California 92112
ATTN: Librarian

123. Standard Oil Company (Indiana)
P.O. Box 400
Naperville, Illinois 60540
ATTN: R. E. Pritz

124. Stauffer Chemical Company
Richmond, California 94802
ATTN: Dr. J. H. Morgenthaler

125. Teledyne CAE
1330 Laskey Road
Toledo, Ohio 43601
ATTN: Technical Library

126. TRW Systems
One Space Park
Redondo Beach, California 90278
ATTN: Mr. F.E. Fendell (R1/1004)

127. TRW Systems Group
One Space Park
Bldg. 0-1 Room 2080
Redondo Beach, California 90278
ATTN: Mr. Donald H. Lee Manager

128. United Technologies Research Center
East Hartford, Connecticut 06108
ATTN: Librarian

129. Valley Forge Sapce Technology Center
P.O. Box 8555
Philadelphia, Pennsylvania 19101
ATTN: Dr. Bert Zauderer

130. Vought Missiles and Space Company
P.O. Box 6267
Dallas, Texas 75222
ATTN: Library - 3-41000

U.S. COLLEGES AND UNIVERSITIES

131. Boston College
Department of Chemistry
Chestnut Hill, Massachusetts 02167
ATTN: Rev. Donald MacLean, S.J.
Associate Professor

132. Brown University
Division of Engineering
Box D
Providence, Rhode Island 02912
ATTN: Dr. R. A. Dobbins

133. California Institute of Technology
Department of Chemical Engineering
Pasadena, California 91109
ATTN: Professor W. H. Corcoran

134. California Institute of Technology
Jet Propulsion Laboratory
4800 Oak Grove Drive
Pasadena, California 91103
ATTN: Library

135. University of California, San Diego
Dept. of Engineering Physics
P.O. Box 109
La Jolla, California 92037
ATTN: Professor S.S. Penner

136. University of California
School of Engineering and
Applied Science
7513 Boelter Hall
Los Angeles, California 90024
ATTN: Engineering Reports Group

137. University of California
Lawrence Radiation Laboratory
P.O. Box 808
Livermore, California 94550
ATTN: Technical Information Dept. L-3

138. University of California
General Library
Berkeley, California 94720
ATTN: Documents Department

139. Case Western Reserve University
10900 Euclid Avenue
Cleveland, Ohio 44106
ATTN: Sears Library - Reports
Department

140. Case Western Reserve University
Division of Fluid Thermal and
Aerospace Sciences
Cleveland, Ohio 44106
ATTN: Professor Eli Reshotko

141. Colorado State University
Engineering Research Center
Fort Collins, Colorado 80521
ATTN: Mr. V. A. Sandborn

142. The University of Connecticut
Department of Mechanical Engineering
U-139
Storrs, Connecticut 06268
ATTN: Professor E. K. Dabora

143. Cooper Union
School of Engineering and Science
Cooper Square
New York, New York 10003
ATTN: Dr. Wallace Chintz
Associate Professor of ME

144. Cornell University
Department of Chemistry
Ithaca, New York 14850
ATTN: Professor Simon H. Bauer

145. Franklin Institute Research Laboratories
Philadelphia, Pennsylvania 19103
ATTN: Dr. G.P. Wachtell

146. George Washington University
Washington, D.C. 20052
ATTN: Dr. Robert Goulard
Dept. of Civil, Mechanical and
Environmental Engineering

147. George Washington University Library
Washington, D.C. 20006
ATTN: Reports Section

148. Georgia Institute of Technology
Atlanta, Georgia 30332
ATTN: Price Gilbert Memorial Library

149. Georgia Institute of Technology
School of Aerospace Engineering
Atlanta, Georgia 30332
ATTN: Dr. Ben T. Zinn

150. University of Illinois
Department of Energy Engineering
Box 4348
Chicago, Illinois 60680
ATTN: Professor Paul H. Chung

151. University of Illinois
College of Engineering
Department of Energy Engineering
Chicago, Illinois 60680
ATTN: Dr. D. S. Hacker

152. The Johns Hopkins University
Applied Physics Laboratory
Johns Hopkins Road
Laurel, Maryland 20810
ATTN: Chemical Propulsion
Information Agency

153. The Johns Hopkins University
Applied Physics Laboratory
Johns Hopkins Road
Laurel, Maryland 20810
ATTN: Document Librarian

154. The Johns Hopkins University
Applied Physics Laboratory
Johns Hopkins Road
Laurel, Maryland 20810
ATTN: Dr. A. A. Westenberg

155: University of Kentucky
Department of Mechanical Engineering
Lexington, Kentucky 40506
ATTN: Dr. Robert E. Peck

156. Massachusetts Institute of Technology
Department of Chemical Engineering
Cambridge, Massachusetts 02139
ATTN: Dr. Jack B. Howard

157. Massachusetts Institute of Technology
Libraries, Room 14 E-210
Cambridge, Massachusetts 02139
ATTN: Technical Reports

158. Massachusetts Institute of Technology
Room 10-408
Cambridge, Massachusetts 02139
ATTN: Engineering Technical Reports

159. Massachusetts Institute of Technology
Dept. of Mechanical Engineering
Room 3-350
Cambridge, Massachusetts 02139
ATTN: Dr. M. Cardillo

160. Massachusetts Institute of Technology
Dept. of Mechanical Engineering
Room 3-246
Cambridge, Massachusetts 02139
ATTN: Professor James Fay

161. Midwest Research Institute
425 Volker Boulevard
Kansas City, Missouri 64100
ATTN: Dr. T. A. Milne

162. New Mexico State University
Dept. of Mechanical Engineering
Box 3450
Las Cruces, New Mexico 88003
ATTN: Dr. Dennis M. Zallen

163. New York Institute of Technology
Wheatley Road
Old Westbury, New York 11568
ATTN: Dr. Fox

164. University of North Carolina
Periodicals and Serials Division
Drawer 870 Library
Chapel Hill, North Carolina 27514
ATTN: Mr. Stephen Berk

165. University of Notre Dame
Serials Record
Memorial Library
Notre Dame, Indiana 46556
ATTN: B. McIntosh

166. University of Notre Dame
College of Engineering
Notre Dame, Indiana 46556
ATTN: Dr. Stuart T. McComas
Assistant Dean for Research
and Special Projects

167. Ohio State University
Dept. of Chemical Engineering
140 West 19th Avenue
Columbus, Ohio 43210
ATTN: Dr. Robert S. Brodkey

168. The Pennsylvania State University
Room 207, Old Main Building
University Park, Pennsylvania 16802
ATTN: Office of Vice President
for Research

169. Princeton University
Dept. of Acrospace and Mechanical
Sciences
James Forrestal Campus
Princeton, New Jersey 08540
ATTN: Dr. Martin Summerfield

170. Princeton University
James Forrestal Campus Library
P.O. Box 710
Princeton, New Jersey 08540
ATTN: V. N. Simosko, Librarian

171. Rice University
Welch Professor of Chemistry
Houston, Texas 77001
ATTN: Dr. Joseph L. Franklin

172. University of Rochester
Dept. of Chemical Engineering
Rochester, New York 14627
ATTN: Dr. John R. Ferron

173. Stanford University
Dept. of Aeronautics and Astronautics
Stanford, California 94305
ATTN: Dr. Walter G. Vincenti

174. State University of New York - Buffalo
Dept. of Mechanical Engineering
228 Parker Engineering Building
Buffalo, New York 14214
ATTN: Dr. George Rudinger

175. Stevens Institute of Technology
Department of Mechanical Engineering
Castle Point Station
Hoboken, New Jersey 07030
ATTN: Professor Fred Sisto

176. University of Virginia
Department of Aerospace Engineering
School of Engineering and Applied Science
Charlottesville, Virginia 22901
ATTN: Dr. John E. Scott

177. University of Virginia
Science/Technology Information Center
Charlottesville, Virginia 22901
ATTN: Dr. Richard H. Austin

178. Yale University
Mason Laboratory
9 Hillhouse Avenue
New Haven, Connecticut 06520
ATTN: Professor Peter P. Wegener

FOREIGN INSTITUTIONS

179. A/S Kongsberg Vaapenfabrikk
Gas Turbine Division
3601 Konsber, NORWAY
ATTN: R.E. Stanley
Senior Aerodynamicist

180. Conservatoire National des Arts
et Metiers
292, Rue Saint'Martin
75141 Paris Cedex 03, FRANCE
ATTN: Professor J. Gossee
Chaire de Thermique

181. DFVLR-Forschungszentrum Gottingen
Institut Fur Stromungsmechanik
Abteilung Theoretische Gashynamik
D-3400 Gottingen
Bunsenstrabe 10, GERMANY
ATTN: Professor Klaus Oswatitsch

182. Ecole Royale Militaire
30 Avenue de la Resaissance
Bruxelles B-1040, BELGIUM
ATTN: Professor Emile Tits

183. Fysisch Laboratorium
Fijksuniversiteit Utrecht
Sorbonnelaan, Utrecht,
THE NETHERLANDS
ATTN: Dr. F. Van der Valk

184. Imperial College
Department of Chemical Engineering
London SW7, ENGLAND
ATTN: Professor F. J. Weinberg

185. Imperial College of Science
and Technology
Department of Mechanical Engineering
Exhibition Road
London, SW7, ENGLAND
ATTN: Professor Gaydon

186. Imperial College of Science
and Technology
Department of Mechanical Engineering
Exhibition Road
London SW7, ENGLAND
ATTN: D. B. Spalding

187/1 Laboratoire de Mecanique des Fluides
36, Route de Dardilly, 36
B.P. No. 17
69130 Ecully, FRANCE
ATTN: G. Assassa

187/2 Laboratoire de Mecanique des Fluides
Ecole Centrale Lyonnaise
36, Route de Dardilly
69130 Ecully, FRANCE
ATTN: Dr. K. Papiliou

188. Ministry of Defense
Main Building, Room 2165
Whitehall Gardens
London SW1, ENGLAND
ATTN: Mr. L.D. Nicholson ED, idc
Vice Controller of Aircraft
Procurement Executive

189. Mitglied des Vorstands der Fried
Krumpp CmbH
43 Essen, Altendorferstrabe 103
GERMANY
ATTN: Professor Dr.-Ing.
Wilhelm Dettmering

190. National Aerospace (NLR)
Voorsterweg 31
Noord-Oost-Polder-Emmelord
THE NETHERLANDS
ATTN: Mr. F. Jaarsma

191. National Research Council
Division of Mechanical Engineering
Montreal Road, Ottawa
Ontario, CANADA KIA OR6
ATTN: Dr. R.B. Whyte

192. Nissan Motor Co., LTD.
3-5-1, Momoi, Suginami-Ku
Tokyo, JAPAN 167
ATTN: Dr. Y. Toda

193. Norweigian Defense Research Establishment
Superintendent NDRE
P.O. Box 25
2007 Kjeller, NORWAY
ATTN: Mr. T. Krog

194. ONERA
Energie and Propulsion
29 Avenue de la Division Leclure
92 Chatillon sous Bagneux, FRANCE
ATTN: Mr. M. Barrere

195. ONERA
Energie and Propulsion
29 Avenue de la Division Leclure
92 Chatillon sous Bagneux, FRANCE
ATTN: Mr. J. Fabri

196. ONERA
Energie and Propulsion
29 Avenue de la Division Leclure
92 Chatillon sous Bagneux, FRANCE
ATTN: Mr. Viaud

197. ONERA-DED
External Relations and Documentation
Department
29, Avenue de la Division Leclure
92320 Chatillon, sous Bagneux, FRANCE
ATTN: Mr. M. Salmon

198. Orta Dogu Teknik Universities
Mechanical Engineering Department
Ankara, TURKEY
ATTN: Professor H. Sezgen

199. Queen Mary College
Department of Mechanical Engineering
Thile Eld Road
London E1, ENGLAND
ATTN: Professor M. W. Thring

200. Rolls-Royce (1971) Limited
Derby Engine Division
P.O. Box 31
Derby DE2 8BJ
London, ENGLAND
ATTN: C. Freeman, Installation
Research Department

201. Rome University
Via Bradano 28
00199 Rome, ITALY
ATTN: Professor Gaetano Salvatore

202. Sener
Departamentao de Investigation
Km. 22.500 de la antigua carretera
Madrid - Barcelona, SPAIN
ATTN: Mr. J. T. Diez Roche

203. Service Technique Aeronautique Moteurs
4 Avenue de la Parte d'Issy
75753 Paris Cedex 15, FRANCE
ATTN: Mr. M. Pianko, Ing. en chef

204. The University of Sheffield
Dept. of Chemical Engineering
and Fuel Technology
Mappin Street, Sheffield S1 3JD
ENGLAND
ATTN: Dr. Norman Chigier

205. Sophia University
Science and Engineering Faculty
Kioi 7 Tokyo-Chiyoda JAPAN 102
ATTN: Professor M. Susuki

206. The University of Sydney
Dept. of Mechanical Engineering
N.S.W. 2006
Sydney, AUSTRALIA
ATTN: Professor R. W. Bilger

207. Technical University of Denmark
Fluid Mechanics Department
Building 404 2800 Lyngby
DK-DENMARK
ATTN: Professor K. Refslund

208. University of Leeds
Leeds, ENGLAND
ATTN: Professor Dixon-Lewis

209. Universite de Poitiers Laboratoire
D'energetique et de Detonique
(L.A. au C.N.R.S. No. 193)
ENSMA - 86034 Poitiers, FRANCE
ATTN: Professor N. Manson

210. University of Tokyo
Department of Reaction Chemistry
Faculty of Engineering
Bunkyo-ku
Tokyo, JAPAN 113
ATTN: Professor T. Hikita

211. Vrije Universiteit Brussel
Fac. Toeg. Wetenshch.
A. Buyllaan 105
1050 Brussels, BELGIUM
ATTN: Ch. Hirsch

PROJECT SQUID CONTRACTORS
1975-76 and 1976-77 (New)

212. AeroChem Research Laboratory, Inc.
Reaction Kinetics Group
P.O. Box 12
Princeton, New Jersey 08540
ATTN: Dr. Arthur Fontijn

213. Aeronautical Research Associates of
Princeton, Inc.
P.O. Box 2229
50 Washington Road
Princeton, New Jersey 08540
ATTN: Dr. Ashok K. Varma

214. California Institute of Technology
Div. of Engineering and
Applied Science
Mail Stop 205-50
Pasadena, California 91109
ATTN: Dr. Anatol Roshko

215. Case Western Reserve University
Div. of Fluid, Thermal and Aerospace
Sciences
Cleveland, Ohio 44106
ATTN: Dr. J.S. T'ien

216. Colorado State University
Engineering Research Center
Foothills Campus
Fort Collins, Colorado 80521
ATTN: Dr. Willy Z. Sadeh

217. General Electric Company
Corporate Research and Development
P.O. Box 8
Schenectady, New York 12301
ATTN: Dr. Marshall Lapp

218. Massachusetts Institute of Technology
Chemistry Department, Room 6-123
77 Massachusetts Avenue
Cambridge, Massachusetts 02139
ATTN: Dr. John Ross

219. Michigan State University
Department of Mechanical Engineering
East Lansing, Michigan 48824
ATTN: Dr. John Foss

220. Pennsylvania State University
Applied Research Laboratory
University Park, Pennsylvania 16802
ATTN: Dr. Edgar P. Bruce

221. Polytechnic Institute of New York
Department of Aerospace Engineering
and Applied Mechanics
Farmingdale, New York 11735
ATTN: Dr. Samuel Lederman

222. Southern Methodist University
Thermal and Fluid Sciences Center
Institute of Technology
Dallas, Texas 75275
ATTN: Dr. Roger L. Simpson

223. Stanford University
Mechanical Engineering Department
Stanford, California 94305
ATTN: Dr. James P. Johnston

224. Stanford University
Mechanical Engineering Department
Stanford, California 94305
ATTN: Dr. S. J. Kline

225. Stanford University
Mechanical Engineering Department
Stanford, California 94305
ATTN: Dr. Sidney Self

226. TRW Systems
Engineering Sciences Laboratory
One Space Park
Redondo Beach, California 90278
ATTN: Dr. J. E. Broadwell

227. United Technologies Research Center
400 Main Street
East Hartford, Connecticut 06108
ATTN: Mr. Franklin O. Carta

228. United Technologies REsearch Center
400 Main Street
East Hartford, Connecticut 06108
ATTN: Dr. Alan C. Eckbreth

229. University of California - San Diego
Department of Aerospace and
Mechanical Engineering
La Jolla, California 92037
ATTN: Dr. Paul Libby

230. University of Colorado
Department of Aerospace
Engineering Sciences
Boulder, Colorado 80304
ATTN: Dr. Mahinder S. Uberoi

231. University of Michigan
Department of Aerospace Engineering
Ann Arbor, Michigan 48105
ATTN: Dr. T. C. Adamson, Jr.

232. University of Michigan
Department of Aerospace Engineering
Ann Arbor, Michigan 48105
ATTN: Dr. Martin Sichel

233. University of Missouri - Columbia
Department of Chemistry
Columbia, Missouri 65201
ATTN: Dr. Anthony Dean

234. University of Southern California
Department of Aerospace Engineering
University Park
Los Angeles, California 90007
ATTN: Dr. F. K. Browand

235. University of Washington
Department of Mechanical Engineering
Seattle, Washington 98195
ATTN: Dr. F.B. Gessner

236. Virginia Polytechnic Institute and
State University
Mechanical Engineering Department
Blacksburg, Virginia 24601
ATTN: Dr. Walter F. O'Brien, Jr.

237. Virginia Polytechnic Institute and
State University
Mechanical Engineering Department
Blacksburg, Virginia 24061
ATTN: Dr. Hal L. Moses

238. Yale University
Engineering and Applied Science
Mason Laboratory
New Haven, Connecticut 06520
ATTN: Dr. John B. Fenn

PURDUE UNIVERSITY

239. School of Aeronautics and Astronautics
Grissom Hall
West Lafayette, Indiana 47907
ATTN: Library

240. School of Mechanical Engineering
Mechanical Engineering Building
West Lafayette, Indiana 47907
ATTN: Library

241-250. Purdue University Advisors

Unclassified

SECURITY CLASSIFICATION OF THIS PAGE (When Data Entered)

REPORT DOCUMENTATION PAGE		READ INSTRUCTIONS BEFORE COMPLETING FORM
1. REPORT NUMBER SMU-2-PU	2. GOVT ACCESSION NO.	3. RECIPIENT'S CATALOG NUMBER
4. TITLE (and Subtitle) LAMINARISCENT TURBULENT BOUNDARY LAYERS: EXPERIMENTS ON NOZZLE FLOWS		5. TYPE OF REPORT & PERIOD COVERED Technical 6. PERFORMING ORG. REPORT NUMBER
7. AUTHOR(s) Professor R. L. Simpson and Mr. C. R. Shackleton		8. CONTRACT OR GRANT NUMBER(s) N00014-75-C-1143
9. PERFORMING ORGANIZATION NAME AND ADDRESS Department of Civil and Mechanical Engineering Southern Methodist University Dallas, TX 75275		10. PROGRAM ELEMENT, PROJECT, TASK AREA & WORK UNIT NUMBERS NR-098-038
11. CONTROLLING OFFICE NAME AND ADDRESS Project SQUID, Thermal Science and Propulsion Center, Purdue University West Lafayette, IN 47907		12. REPORT DATE January 1977 13. NUMBER OF PAGES 87
14. MONITORING AGENCY NAME & ADDRESS (if different from Controlling Office) Office of Naval Research Department of the Navy Arlington, VA 22217		15. SECURITY CLASS. (of this report) Unclassified 15a. DECLASSIFICATION/DOWNGRADING SCHEDULE

16. DISTRIBUTION STATEMENT (of this Report)

This document has been approved for public release and sale; its distribution is unlimited.

17. DISTRIBUTION STATEMENT (of the abstract entered in Block 20, if different from Report)

18. SUPPLEMENTARY NOTES

19. KEY WORDS (Continue on reverse side if necessary and identify by block number)

Bursting frequency	Intermittency
Cross-correlation	Laminariscent boundary layers
Dissipation	Turbulence intensities
Entrainment	Velocity fluctuation spectra
Hot-film anemometer	Viscous sublayer structure

20. ABSTRACT (Continue on reverse side if necessary and identify by block number)

Because a turbulent boundary layer in a nozzle undergoes strong acceleration, a laminariscent boundary layer with the benefit of a lower surface heat transfer rate can result for some short distance. Here and in a previous report (Simpson and Wallace, 1975) several phenomena which accompany laminarescence produced by strong acceleration are examined for nozzle-flow and sink-flow accelerational distributions, respectively. Several different type measurements of the structure of two nozzle-type flows are reported to determine how an initially normal

DD FORM 1 JAN 73 1473 EDITION OF 1 NOV 65 IS OBSOLETE

Unclassified

SECURITY CLASSIFICATION OF THIS PAGE (When Data Entered)

20. turbulent boundary layer approaches the laminar-like state, including mean velocity and Reynolds stresses profiles, spectra, turbulent/non-turbulent interfacial structure, and wall bursting and sublayer spanwise spatial structure.

As a result of these experiments, it appears that the surface skin-friction is not reduced to laminar values in sink flows unless $K(=\nu U_\infty^{-2} dU_\infty/dx)$ is greater than about 3.6×10^{-6}. In nozzle-type flows, K must also be greater than this value over a short distance in order to produce a short relaminarized region downstream. The large-eddy structure of the outer region governs the bursting frequency, the intermittent bulge passage frequency, and influences the wall flow behavior downstream. After the cessation of entrainment of free-stream fluid, these frequencies approach constant values. The wall spanwise structure appears to lag behind local conditions and to reflect upstream flow behavior. After retransition to a low acceleration turbulent boundary layer downstream, much larger spanwise scale structures are observed.

The entrainment rate of non-turbulent fluid decreases to zero at about the streamwise location at which the shape factor reaches a minimum value. The cessation of entrainment by the eruption and engulfment action of the large eddies can be traced to the reduction of available turbulence energy for diffusion to free-stream fluid. This reduction of available energy is due to the negative normal stresses turbulence energy production term. Spectral distributions of the streamwise fluctuation F(n) possess a frequency region where nF(n) is constant for laminar-like boundary layers at large K values.